Strål
säkerhets
myndigheten
Swedish Radiation Safety Authority

Authors:
Peter Dillström
Mats Bergman
Björn Brickstad
Weilin Zang
Iradj Sattari-Far
Peder Andersson
Göran Sund
Lars Dahlberg
Fred Nilsson

Research

2008:01

A combined deterministic and probabilistic procedure for safety assessment of components with cracks – Handbook

Report number: 2008:01 **ISSN:** 2000-0456
Available at www.stralsakerhetsmyndigheten.se

Title: A combined deterministic and probabilistic procedure for safety assessment of components with cracks – Handbook.
Report number: 2008:01
Author/Authors: Peter Dillström, Mats Bergman, Björn Brickstad, Weilin Zang, Iradj Sattari-Far, Peder Andersson, Göran Sund, Lars Dahlberg and Fred Nilsson
Name of your company or institution/city and country: DNV Technology Sweden (now Inspecta Technology AB)/Stockholm Sweden.

Background

SSM has supported research work for the further development of a previously developed procedure/handbook (SKI Report 99:49) for assessment of detected cracks and tolerance for defect analysis. During the operative use of the handbook it was identified needs to update the deterministic part of the procedure and to introduce a new probabilistic flaw evaluation procedure. Another identified need was a better description of the theoretical basis to the computer program.

The project was initiated by SKI.

Objectives of the project

The principal aim of the project has been to update the deterministic part of the recently developed procedure and to introduce a new probabilistic flaw evaluation procedure. Other objectives of the project have been to validate the conservatism of the procedure, make the procedure well defined and easy to use and make the handbook that documents the procedure as complete as possible.

Results

The procedure/handbook and computer program ProSACC, Probabilistic Safety Assessment of Components with Cracks, has been extensively revised within this project.
The major differences compared to the last revision are within the following areas:

- It is now possible to deal with a combination of deterministic and probabilistic data.
- It is possible to include J-controlled stable crack growth.
- The appendices on material data to be used for nuclear applications and on residual stresses are revised.
- A new deterministic safety evaluation system is included.
- The conservatism in the method for evaluation of the secondary stresses for ductile materials is reduced.
- A new geometry, a circular bar with a circumferential surface crack has been introduced.

Effect on SSM supervisory and regulatory task

The results of this project will be of use to SSM in safety assessments of components with cracks and in assessments of the interval between the inspections of components in nuclear power plants.

Project information

SSM´s Project Leader: Kostas Xanthopoulos
Project number: 14.42-000696/00202.
Project Organisation: DNV Technology Sweden (now Inspecta Technology AB) has managed the project with P. Dillström as project leader. M. Bergman, B. Brickstad, W. Zang, I. Sattari-Far, P. Andersson, G. Sund, L. Dahlberg and F. Nilsson have assisted in the development of the project.

Table of Content *Page*

NOMENCLATURE

a	Crack depth for surface cracks
$\overline{a}$	Crack depth with a plastic zone correction
$2a$	Crack depth for embedded cracks
da/dN	Local crack growth rate for fatigue crack cracking
da/dt	Local crack growth rate for stress corrosion cracking
b	Geometry parameter to define a crack in a cylindrical bar
c	Constant in algorithm to calculate the most probable point of failure (MPP)
c_1, c_2	Constants in the distribution function - Probability Of Detection
c_i	Constants in fitting polynomial
C	Constant for fatigue or stress corrosion crack growth
d_i	Search direction vector to the most probable point of failure (MPP)
D	Diameter of a cylindrical bar, diameter, distance in an X shaped weld geometry
$D(\ldots)$	Detection event
E	Elastic modulus, energy
e	Eccentricity of embedded cracks
f	Geometry function for stress intensity factor, frequency
f_b	Geometry function for stress intensity factor, $b \rightarrow$ bending
f_{FAD}	Failure assessment curve
f_m	Geometry function for stress intensity factor, $m \rightarrow$ membrane
f_{R6}	R6 revision 3, option 1 type failure assessment curve
$f_X(x)$	Joint probability density function
F_{POD}	Distribution function - Probability Of Detection
$F_X(x)$	Cumulative distribution function
$g(x)$	Limit state function
$g(X)$	Limit state function
g_f	Material function to define the crack growth (fatigue)
$g_{FAD}(X)$	Limit state function - Failure assessment diagram
$g_{Linear}(u)$	Transformed limit state function, using a linear approximation
$g_{L_r^{max}}(X)$	Limit state function - Upper limit of L_r
$g_{Quadratic}(u)$	Transformed limit state function, using a quadratic approximation

g_{sc}	Material function to define the crack growth (stress corrosion)
$g_U(u)$	Limit state function in a transformed standard normal space U
$G(\ldots)$	Limit state event
J	J-integral
J_{Ic}	Critical J-value according to ASTM E1820
J_{acc}	Acceptable value of the J-integral
J_R	J-resistance (curve)
k	Weibull distribution parameter - shape
K	Parameter used in the definition of fatigue growth data for ferritic steel
K_{I}	Stress intensity factor
K_{I}^{max}	Maximum stress intensity factor
K_{I}^{min}	Minimum stress intensity factor
K_{I}^{p}	Primary stress intensity factor
K_{I}^{s}	Secondary stress intensity factor
K_{Ia}	Fracture toughness at crack arrest
K_{Ic}	Fracture toughness according to ASTM E399
K_1	Elastic stress intensity factor (used in the modified version of Budden`s method)
K_2	Plastic stress intensity factor (used in the modified version of Budden`s method)
K_{cr}	Critical value of stress intensity factor
K_{cr}^{d}	Critical value of stress intensity factor (used in design)
K_r	Fracture parameter
l	Crack length
l_m	Crack length at the mean radius of a cylinder
L_r	Limit load parameter
L_r^{max}	Maximum allowed value of the limit load parameter
$m(\ldots)$	Merit function in algorithm to calculate the most probable point of failure (MPP)
M_0	Applied bending moment on a cylindrical bar
M_f	Limit load in pure bending for a cylindrical bar
M_{limit}	Limit load parameter for a cylindrical bar
n	Constant for fatigue or stress corrosion crack growth
N	Number of cycles, total number of simulations, number of random variables, number of inspections

N_0	Applied tensile force on a cylindrical bar
N_f	Limit load in pure tension for a cylindrical bar
N_F	Number of failures during simulation
N_{limit}	Limit load parameter for a cylindrical bar
P_F	Probability of failure
$P_{F,FORM}$	Probability of failure - using First-Order Reliability Method
$P_{F,MCS}$	Probability of failure - using Simple Monte Carlo Simulation
$P_{F,SORM}$	Probability of failure - using Second-Order Reliability Method
P_L	Limit load, local membrane stress
P_m	The primary general membrane stress
R	Stress intensity factor ratio, $R = K_{\mathrm{I}}^{min} / K_{\mathrm{I}}^{max}$, radius of a cylindrical bar
R_e	Yield strength – standardised value
R_{eL}	Lower yield strength
R_i	Inner radius
R_m	Ultimate tensile strength – standardised value, mean radius of a cylinder
$R_{p0.2}$	0.2% elongation stress
$R_{p1.0}$	1.0% elongation stress
RT_{NDT}	Nil-ductility transition temperature
s	Distance between neighbouring defects
s_{bg}	Stress parameter, used in the definition of limit loads for circumferential cracks in a cylinder
s'_{bg}	Stress parameter, used in the definition of limit loads for circumferential cracks in a cylinder
s_i	Step size in algorithm to calculate the most probable point of failure (MPP)
s_m	Stress parameter, used in the definition of limit loads for circumferential cracks in a cylinder
s'_m	Stress parameter, used in the definition of limit loads for circumferential cracks in a cylinder
SF	Safety factor, safety margin
SF_J	Safety factor against fracture described by J
SF_K	Safety factor against fracture described by K_{I}, $SF_K = \sqrt{SF_J}$
$SF_K^{Primary}$	Primary safety factor against fracture described by K_{I}

$SF_K^{Secondary}$	Secondary safety factor against fracture described by K_{I}
SF_L	Safety factor against plastic collapse
S_m	Allowable design stress
S_r	Magnitude of residual stresses
T	Temperature
T_{app}	Applied tearing modulus
T_R	Tearing modulus
t	Plate or wall thickness, time
u	Coordinate, random number - between 0 and 1, transformed random parameter
U	Transformed random vector
x	Coordinate, random parameter, random variable
X	Random vector
y_i	Approximation to the most probable point of failure (MPP)
z	Parameter of the gamma function
Δa	Stable crack growth
ΔK_{I}	Stress intensity factor range, $\Delta K_{\mathrm{I}} = K_{\mathrm{I}}^{max} - K_{\mathrm{I}}^{min}$
$\Delta K_{\mathrm{I}}^{eff}$	Effective stress intensity factor range
Δ_{total}	Total displacement, used in the definition of applied tearing modulus
α	Angle parameter - used in the definition of limit loads for circumferential cracks in a cylinder, Confidence level for error estimation - using Simple Monte Carlo Simulation
β	Angle parameter, used in the definition of limit loads for circumferential cracks in a cylinder and for surface cracks in a bar. Parameter used to differentiate between plane stress and plane strain in a plastic zone correction according to Irwin
β_{HL}	Reliability index
ε_{MCS}	Error estimate - using Simple Monte Carlo Simulation
ϕ	Angle parameter, used in the definition of limit loads for surface cracks in a bar
$\Phi(u)$	Cumulative distribution function in standard normal space
γ_m^k	Partial coefficient (related to fracture toughness)
γ_m^y	Partial coefficient (related to yield strength)
$\Gamma(z)$	Gamma function
κ_i	Principal curvatures of the limit state surface
λ	Equivalent crack length, Exponential distribution parameter
μ_a	Defect depth, defect size - mean value

$\mu_{K_{Ic}}$	Fracture toughness - mean value
μ_{LogNor}	Log-normal distribution parameter - log-normal mean value
μ_{σ_U}	Ultimate tensile strength - mean value
μ_{σ_Y}	Yield strength - mean value
ν	Poisson's ratio
θ	Angle parameter, used in the definition of limit loads for circumferential cracks in a cylinder, Weibull distribution parameter - scale
ρ	Parameter for interaction between primary and secondary stresses
σ	Stress
σ_0	Stress amplitude
σ_a	Defect depth, defect size - standard deviation
σ_b	Through-thickness bending stress
σ_{bg}	Global bending stress
σ_f	Flow stress
$\sigma_{K_{Ic}}$	Fracture toughness - standard deviation
σ_{LogNor}	Log-normal distribution parameter - log-normal standard deviation
σ_m	Membrane stress
σ^p	Primary stress
σ^s	Secondary stress
σ_Y	Yield strength, R_{eL} or $R_{p0.2}$ (used in design)
σ_Y^d	Yield strength (used in design)
σ_U	Ultimate tensile strength, R_m
σ_{σ_U}	Ultimate tensile strength - standard deviation
σ_{σ_Y}	Yield strength - standard deviation
χ	Parameter for calculation of interaction parameter ρ between primary and secondary stresses
ζ	Equivalent crack depth over length ratio

1. INTRODUCTION

In this handbook a procedure is described which can be used both for assessment of detected cracks or crack like defects and for defect tolerance analysis. The procedure can be used to calculate possible crack growth due to fatigue or stress corrosion and to calculate the reserve margin for failure due to fracture and plastic collapse. For all materials, the procedure gives the reserve margin for initiation of stable crack growth and for ductile materials there is also the possibility to present the reserve margin including a limited amount of stable crack growth. In this fourth edition of the handbook, a new probabilistic flaw evaluation procedure is introduced.

The procedure was developed for operative use with the following objectives in mind:

a) The procedure should be able to handle both linear and non-linear problems without any a priori division.
b) The procedure shall ensure uniqueness of the deterministic safety assessment.
c) The procedure shall include the possibility to do a probabilistic safety assessment.
d) The procedure should be well defined and easy to use.
e) The conservatism of the procedure should be well validated.
f) The handbook, that documents the procedure, should be so complete that for most assessments, access to any other fracture mechanics literature should not be necessary.

The method utilized in the procedure is based on the R6-method [1.1] developed at Nuclear Electric plc. The basic assumption is that fracture initiated by a crack can be described by the variables K_r and L_r. K_r is the ratio between the stress intensity factor and the fracture toughness of the material. L_r is the ratio between applied load and the plastic limit load of the structure. The pair of calculated values of these variables is plotted in a diagram; see Fig. 1 in Chapter 2.1. If the point is situated within the non-critical region, fracture is assumed not to occur. If the point is situated outside the region, crack growth and fracture may occur.

The method can in principal be used for all metallic materials. It is, however, more extensively verified for steel alloys only. The method is not intended for use in temperature regions where creep deformation is of importance.

To fulfil the above given objectives, the handbook contains solutions for the stress intensity factor and the limit load for a number of crack geometries of importance for applications. It also contains rules for defect characterization, recommendations for estimation of residual stresses, material data for nuclear applications and a safety evaluation system. To ensure conservatism, the procedure with the given solutions of the stress intensity factor and the limit load has been validated [1.2]. Predictions of the procedure were compared with the actual outcome of full scale experiments reported in the literature. Some of the new solutions introduced in this fourth edition of the handbook are, however, not included in the validation reported in Ref. [1.2]. However, additional validations have been published in the last revision of the R6 document [1.3].

The first edition of the handbook was released in 1990, the second in 1991 and the third in 1996. This fourth edition has been extensively revised. A new deterministic safety evaluation system has been introduced. The conservatism in the method for assessment of secondary stresses, for ductile materials, has been reduced. It is now possible to include *J*-dominated stable crack growth. The solutions for the stress intensity factor and the limit load, the recommendations for estimation of residual stresses and the given material data for nuclear applications have been updated. A new geometry, a bar with a circumferential surface crack is included. Finally, a new probabilistic flaw evaluation procedure is introduced.

A modern Windows based PC-program ProSACC [1.4] has been developed which can perform the assessments described in this handbook including calculation of crack growth due to stress corrosion and fatigue. The program also has an option which enables assessment of cracks according to the 1995 edition of the ASME Boiler and Pressure Vessel Code, Section XI. Appendices A, C and H for assessment of cracks in ferritic pressure vessels, austenitic piping and ferritic piping, respectively. The probabilistic assessments performed by ProSACC, are based on the R6 method only.

The revision of the handbook and the PC-program ProSACC was financially funded by the Swedish Nuclear Power Inspectorate (SKI), Barsebäck Kraft AB, Forsmarks Kraftgrupp AB, OKG Aktiebolag and Ringhals AB. The support has made this work possible and is greatly appreciated.

1.1 References

[1.1] MILNE, I., AINSWORTH, R. A., DOWLING, A. R., and A. T. STEWART, (1988), "Assessment of the integrity of structures containing defects", *The International Journal of Pressure Vessels and Piping*, Vol. 32, pp. 3-104.

[1.2] SATTARI-FAR, I., and F. NILSSON, (1991), "Validation of a procedure for safety assessment of cracks", SA/FoU-Report 91/19, SAQ Kontroll AB, Stockholm, Sweden.

[1.3] —, (2003), "Assessment of the Integrity of Structures Containing Defects", R6 – Revision 4, Up to amendment record No.2, British Energy Generation Ltd.

[1.4] DILLSTRÖM, P., and W. ZANG., (2004), "User manual ProSACC Version 1.0", DNV Research Report 2004/02, Det Norske Veritas AB, Stockholm, Sweden.

2. PROCEDURE

2.1 Overview

A deterministic fracture assessment according to the procedure consists of the following steps:

1) Characterization of defect (Chapter 2.2 and Appendix A).
2) Choice of geometry (Chapter 2.3 and Appendix G).
3) Determination of stress state (Chapter 2.4).
4) Determination of material data (Chapter 2.5 and Appendix M).
5) Calculation of possible slow crack growth (Chapter 2.6 and Appendix M).
6) Calculation of K_I^p and K_I^s (Chapter 2.7 and Appendix K).
7) Calculation of L_r (Chapter 2.8 and Appendix L).
8) Calculation of K_r (Chapter 2.9).
9) Fracture assessment (Chapter 2.10).

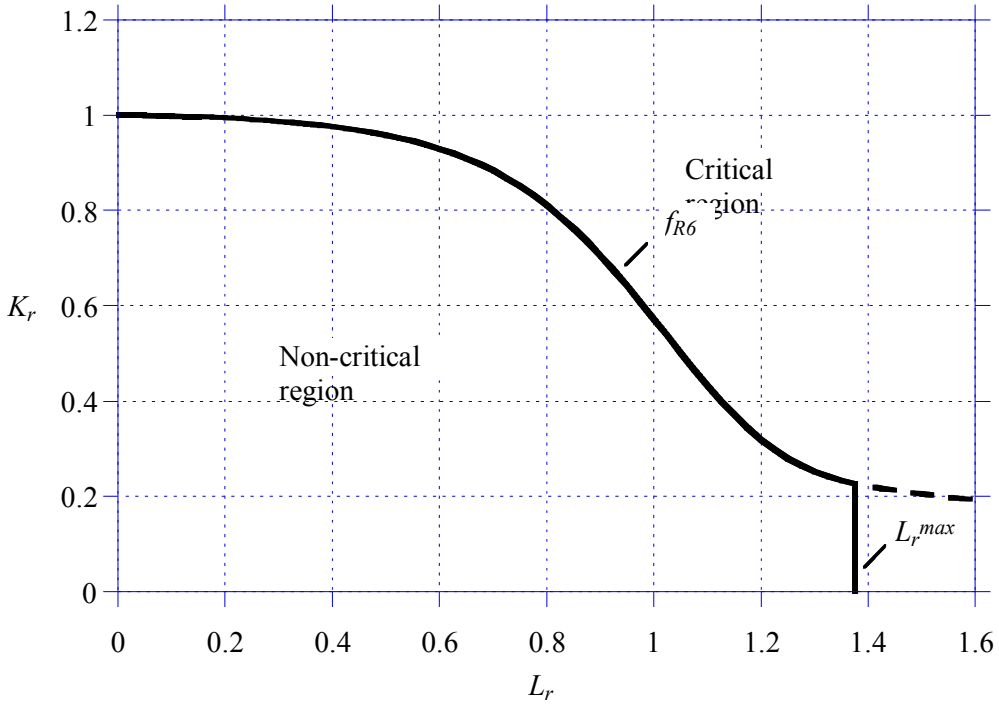

Figure 2.1. Diagram for fracture assessment (FAD).

The non-critical region is limited by,

$$K_r \le f_{R6} = (1 - 0.14L_r^2)[0.3 + 0.7\exp(-0.65L_r^6)] \quad , \tag{2.1}$$

$$L_r \le L_r^{max} = \begin{cases} 1, & \text{for materials with a yield plateu} \\ \dfrac{\sigma_f}{\sigma_Y}, & \text{for all other cases} \end{cases} \quad . \tag{2.2}$$

10) Assessment of results (Chapter 2.11).

2.2 Characterization of defect

A fracture mechanics analysis requires that the actual defect geometry is characterized in a unique manner. For application to components in nuclear power facilities methods according to Appendix A should be used to define shape and size of cracks.

For assessment of an actual defect it is important to determine whether the defect remains from the manufacture or has occurred because of service induced processes such as fatigue or stress corrosion cracking.

2.3 Choice of geometry

The geometries considered in this procedure are documented in Appendix G. In the idealization process from the real geometry to these cases care should be taken to avoid non-conservatism. In cases when an idealization of the real geometry to one of the cases considered here are not adequate, stress intensity factor and limit load solutions can be found in the literature or be calculated by numerical methods. The use of such solutions should be carefully checked for accuracy.

2.4 Stress state

In this procedure it is assumed that the stresses have been obtained under the assumption of linearly elastic material behaviour. The term nominal stress denotes the stress state that would act at the plane of the crack in the corresponding crack free component.

The stresses are divided into primary σ^p and secondary σ^s stresses. Primary stresses are caused by the part of the loading that contributes to plastic collapse e.g. pressure, gravity loading etc. Secondary stresses are caused by the part of the loading that does not contribute to plastic collapse e.g. stresses caused by thermal gradients, weld residual stresses etc. If the component is cladded this should be taken into account when the stresses are determined.

All stresses acting in the component shall be considered. The stresses caused by the service conditions should be calculated according to some reliable method. Some guidance about weld residual stresses is given in Appendix R.

2.5 Material data

To perform the assessments the yield strength σ_Y, the ultimate tensile strength σ_U, the critical stress intensity factor K_{cr} and J_r-curves of the material must be determined. If possible, data obtained from testing of the actual material of the component should be used. This is not always possible and therefore minimum values for σ_Y and σ_U from codes, standards or material specifications may be used. These data should be determined at the actual temperature.

σ_Y is equal to the lower yield strength R_{eL} if this can be determined and in other cases the 0.2% proof stress $R_{p0,2}$. In the cases when R_{eL} can be determined the material is considered to have a yield plateau. This is for instance common for certain low alloy carbon manganese steels at low temperatures.

σ_U is the ultimate tensile strength of the material.

The yield strength and ultimate tensile strength of the base material should normally be used even when the crack is situated in a welded joint. The reason for this is that the yield limit of the structure is not a local property but also depends on the strength properties of the material remote from the crack.

K_{cr} is the critical value of the stress intensity factor for the material at the crack front. If possible, K_{cr} should be set equal to the fracture toughness K_{Ic} according to ASTM E399 [2.1]. It is in many cases not possible to obtain a valid K_{Ic}-value. J_{Ic}-values according to ASTM E1820 [2.2] can be used instead and be converted according to Eq. (2.3).

$$K_{cr} = \sqrt{\frac{EJ_{Ic}}{1-\nu^2}} \quad . \tag{2.3}$$

Here E is the elastic modulus of the material and ν is Poisson's ratio.

Ductile materials normally show a significant raise of the J-resistance curve after initiation. When taking this into account, J_r-data according to ASTM E1820 [2.2] should be used.

For application on nuclear components fracture toughness and J_r-curves according to Appendix M can be used if actual test data for the considered material is not available.

When not stated otherwise the material data for the actual temperature should be used.

2.6 Calculation of slow crack growth

The final fracture assessment as described below should be based on the estimated crack size at the end of the service period. In cases where slow crack growth due to fatigue, stress corrosion cracking or some other mechanism can occur the possible growth must be accounted for in the determination of the final crack size.

The rate of crack growth due to both fatigue and stress corrosion cracking is supposed to be governed by the stress intensity factor K_I. This quantity is calculated according to methods described in Appendix K.

For fatigue crack growth, the rate of growth per loading cycle can be described by an expression of the form

$$\frac{da}{dN} = g_f(\Delta K_I,\ R) \quad . \tag{2.4}$$

Here

$$\Delta K_I = K_I^{max} - K_I^{min} \quad , \tag{2.5}$$

and

$$R = \frac{K_I^{min}}{K_I^{max}} \quad , \tag{2.6}$$

where K_I^{max} and K_I^{min} are the algebraic maximum and minimum, respectively, of K_I during the load cycle. g_f is a material function that can also depend on environmental factors such as temperature and humidity. For cases when $R < 0$ the influence of the R-value on the crack growth rate can be estimated by use of growth data for $R = 0$ and an effective stress intensity factor range according to

$$\Delta K_I^{eff} = K_I^{max}, \qquad \text{if} \quad K_I^{min} < 0 \quad . \tag{2.7}$$

For application on nuclear components fatigue crack growth data according to Appendix M can be used if actual test data for the considered material is not available.

For stress corrosion cracking, the growth rate per time unit can be described by a relation of the form

$$\frac{da}{dt} = g_{sc}(K_I) \quad . \tag{2.8}$$

g_{sc} is a material function which is strongly dependent on environmental factors such as the temperature and the chemical properties of the environment.

For application on nuclear components stress corrosion crack growth data according to Appendix M can be used if actual test data for the material and environment under consideration is not available.

2.7 Calculation of K_I^p and K_I^s

The stress intensity factors K_I^p (caused by primary stresses σ^p) and K_I^s (caused by secondary stresses σ^s) are calculated with the methods given in Appendix K. For the cases given it is assumed that the nominal stress distribution (i.e. without consideration of the crack) is known.

Limits for the applicability of the solutions are given for the different cases. If results are desired for a situation outside the applicability limits a recharacterization of the crack geometry can sometimes be made. The following recharacterizations are recommended:

a) A semi-elliptical surface crack with a length/depth ratio which is larger than the applicability limit can instead be treated as an infinitely long two-dimensional crack.

b) A semi-elliptical surface crack with a depth that exceeds the applicability limit can instead be treated as a through-thickness crack with the same length as the original crack.

c) A cylinder with a ratio between wall thickness and inner radius which is below the applicability limit can instead be treated as a plate with a corresponding stress state.

In cases when the solutions of Appendix K cannot be applied, stress intensity factors can be obtained either by use of solutions found in the literature, see for example the handbooks [2.3], [2.4], [2.5] and [2.6], or by numerical calculations, e.g. by the finite element method.

2.8 Calculation of L_r

L_r is defined as the ratio between the current primary load and the limit load P_L for the component under consideration and with the presence of the crack taken into account. P_L should be calculated under the assumption of a perfectly-plastic material with the yield strength σ_Y chosen as discussed in Chapter 2.5. Appendix L contains solutions of L_r for the cases considered in this procedure.

Limits for the applicability of the solutions are given for the different cases. If results are desired for a situation outside the applicability limits a recharacterization of the crack geometry can sometimes be made similarly to what was discussed for the stress intensity factor above.

In cases when the solutions of Appendix L cannot be applied, L_r can be obtained either by use of solutions found in the literature, see for example [2.7], or by numerical calculations, e.g. by the finite element method.

2.9 Calculation of K_r

The ordinate K_r in the failure assessment diagram (Fig. 2.1) is calculated in the following way.

$$K_r = \frac{K_{\mathrm{I}}^p + K_{\mathrm{I}}^s}{K_{cr}} + \rho \quad , \tag{2.9}$$

where ρ is a parameter that takes into account plastic effects because of interaction between secondary and primary stresses. ρ is obtained from the diagram in Fig. 2.2 where ρ is given as a function of L_r and the parameter χ defined as

$$\chi = \frac{K_I^s L_r}{K_I^p} \quad . \tag{2.10}$$

χ is set to zero if χ falls below zero. Also, ρ is restricted to non-negative values as defined in Fig. 2.2.

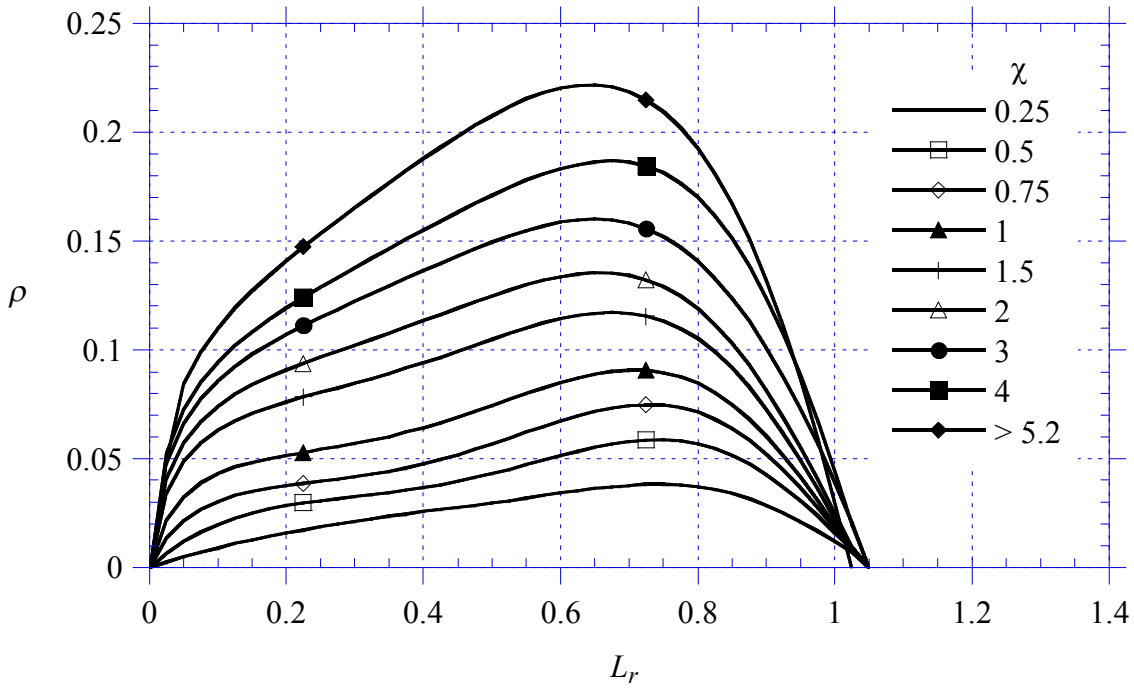

Figure 2.2. Diagram for calculation of ρ.

2.10 Fracture assessment

In order to assess the risk of fracture the assessment point (L_r, K_r) calculated as described above is plotted in the diagram in Fig. 2.1. If the point is situated within the non-critical region no initiation of crack growth is assumed to occur and thus no fracture. The non-critical region is limited by the R6 option 1 (see R6, Revision 3 or [2.8]) type failure assessment curve according to

$$K_r \le f_{R6} = (1 - 0.14L_r^2)[0.3 + 0.7\exp(-0.65L_r^6)] \quad , \tag{2.11}$$

$$L_r \le L_r^{max} \quad . \tag{2.12}$$

For materials which shows a continuous stress-strain curve without any yield plateau, the upper limit of L_r is defined by

$$L_r^{max} = \frac{\sigma_f}{\sigma_Y} \quad , \tag{2.13}$$

where σ_f is the uniaxial flow stress. Depending on application and type of material, σ_f is given by

$$\sigma_f = \begin{cases} 2.4S_m, & \text{for ferritic nuclear components} \\ 3.0S_m, & \text{for austenitic nuclear components} \\ (\sigma_Y + \sigma_U)/2, & \text{for all other cases} \end{cases} \quad . \tag{2.14}$$

Here S_m is the allowable design stress defined by

$$S_m = \min\left(\frac{2\sigma_Y(20\ ^\circ\mathrm{C})}{3},\ \frac{2\sigma_Y(T)}{3},\ \frac{\sigma_U(20\ ^\circ\mathrm{C})}{3},\ \frac{\sigma_U(T)}{3} \right) \quad , \tag{2.15}$$

for ferritic materials and by

$$S_m = \min\left(\frac{2\sigma_Y(20\ ^\circ\mathrm{C})}{3},\ 0.9\sigma_Y(T),\ \frac{\sigma_U(20\ ^\circ\mathrm{C})}{3},\ \frac{\sigma_U(T)}{3} \right) \quad , \tag{2.16}$$

for austenitic materials. T is the temperature of the material.

For materials that exhibit a discontinuous yield point L_r^{max} is restricted to 1.0. This is conservative and should be regarded as a compromise when applying the option 1 type R6 failure assessment curve to a problem that is actually better described by an option 2 type failure assessment curve, cf. [2.8].

When the failure load of a component with a crack is sought, the above described procedure is carried out for different load levels and the crack geometry is kept constant. The critical load is then given by the load level which causes the point (L_r, K_r) to fall on the border to the critical region. Similarly, the limiting crack size is obtained by keeping the loads fixed and calculating the point (L_r, K_r) for different crack sizes until it falls on the border to the critical region.

In order to assess the risk of fracture for materials with high toughness, stable crack growth has to be included in the assessment. The non-critical region is here limited by

$$J = J_R \quad , \tag{2.17}$$

$$T_{app} \le T_R \quad , \tag{2.18}$$

where J is the applied J, J_R is the resistance curve, T_{app} is the applied tearing modulus and T_R is the tearing modulus. In Appendix B, the background to this assessment is given.

2.11 Safety assessment

The following conditions should be fulfilled to determine if a detected crack of a certain size is acceptable, cf. [2.9]:

$$J \le \frac{J_{Ic}}{SF_J} \quad , \tag{2.19}$$

$$P \le \frac{P_L}{SF_L} \quad . \tag{2.20}$$

Eqs. (2.19) and (2.20) account for the failure mechanisms fracture and plastic collapse and SF_J and SF_L are the respective safety factors against these failure mechanisms. Plastic collapse is assumed to occur when the primary load P is equal to the limit load P_L. This occurs when the remaining ligament of the cracked section becomes fully plastic and has reached the flow stress σ_f. J is the path-independent J-integral which is meaningful for situations where J completely characterizes the crack-tip conditions. J should be evaluated with all stresses present (including residual stresses) and for the actual material data. J_{Ic} is the value of the J-integral at which initiation of crack growth occurs.

In this procedure J is estimated using the option 1 type R6 failure assessment curve [2.8]. The R6-estimation of J is given by

$$J = \frac{(1-\nu^2)K_I^2}{E} \frac{1}{[f_{R6}(L_r) - \rho]^2} \quad , \tag{2.21}$$

where f_{R6} is defined by Eq. (2.11). The second fraction on the right hand side of Eq. (2.21) can be interpreted as a plasticity correction function, based on the limit load, for the linear elastic value of J determined by the stress intensity factor K_{I}.

Combining Eqs. (2.3), (2.19) and (2.21) gives the following relation for the acceptance of a crack:

$$\frac{K_{\mathrm{I}}}{K_{cr}} + \frac{\rho}{\sqrt{SF_J}} \le \frac{f_{R6}(L_r)}{\sqrt{SF_J}} \quad . \tag{2.22}$$

The left-hand side of Eq. (2.22) represents the parameter K_r used for safety assessment. Eq. (2.22) implies that the assessment point (L_r, K_r) should be located below the R6 failure assessment curve divided by the safety factor $\sqrt{SF_J}$. The maximum acceptable condition is obtained in the limit when the assessment point is located on the reduced failure assessment curve, expressed by Eq. (2.22) with a sign of equality. In addition a safety factor against plastic collapse, corresponding to Eq. (2.19), is introduced as a safety margin against the cut-off of L_r as

$$L_r \le \frac{L_r^{max}}{SF_L} \quad . \tag{2.23}$$

Eqs. (2.22) and (2.23) represent the safety assessment procedure used in this handbook and in the PC-program ProSACC [2.10]. In Appendix S, a set of safety factors are defined to be used for nuclear applications, cf. [2.9]. The safety factor SF_K is introduced which is the safety factor on K_{cr} corresponding to the safety factor SF_J on J_{Ic}. They are related through $SF_K = \sqrt{SF_J}$. Critical conditions are obtained when all safety factors are set to unity and when the assessment point is located on the failure assessment curve.

One drawback with this deterministic safety evaluation system is that it may overestimate the contribution from secondary stresses (i.e. welding residual stresses or stresses from a thermal transient) for ductile materials. The Swedish Nuclear Power Inspectorate and Det Norske Veritas has therefore started a project that will lead to a quantitative recommendation on how to treat secondary stresses for high L_r-values in a R6 fracture assessment. This recommendation will define new safety factors against fracture described by K_{I} and differentiate between $SF_K^{Primary}$ (relating to primary stresses) and $SF_K^{Secondary}$ (relating to secondary stresses). The results from this project will be incorporated in the next revision of the handbook.

Ductile materials normally show a significant raise of the *J*-resistance curve after initiation. When doing a safety assessment, including stable crack growth, Eq. (2.19) is no longer valid. The acceptable region is then given by

$$J \le \frac{J_R}{SF_J} \quad \text{and} \quad T_{app} \le \frac{T_R}{SF_J} \quad . \tag{2.24}$$

In cases which are particularly difficult to assess, a sensitivity analysis may be necessary. Such an analysis is simplest to perform by a systematic variation of the load, crack size and material properties.

2.12 References

[2.1] —, (1997), "Standard Test Method for Plane-Strain Fracture Toughness of Metallic Materials", ASTM Standard E399 – 90.

[2.2] —, (2001), "Standard Test Method for Measurement of Fracture Toughness", ASTM Standard E 1820 – 01.

[2.3] MURAKAMI, Y. (ed.), (1987-1991), *Stress intensity factors handbook*, Vol. 1-3, Pergamon Press, Oxford, U.K.

[2.4] MURAKAMI, Y. (ed.), (2001), *Stress intensity factors handbook*, Vol. 4-5, Elsevier, Oxford, U.K.

[2.5] TADA, H., PARIS, P. C., and G. C. IRWIN, (1985), *The stress analysis of cracks handbook*, 2nd edition, Paris Productions Inc., St. Louis, U.S.A.

[2.6] ROOKE, D. P., and D. J. CARTWRIGHT, (1976), *Compendium of stress intensity factors*, Her Majesty's Stationary Office, London, U.K.

[2.7] MILLER, A. G., (1988), "Review of limit loads of structures containing defects", *The International Journal of Pressure Vessels and Piping*, Vol. 32, pp. 197-327.

[2.8] MILNE, I., AINSWORTH, R. A., DOWLING, A. R., and A. T. STEWART, (1988), "Assessment of the integrity of structures containing defects", *The International Journal of Pressure Vessels and Piping*, Vol. 32, pp. 3-104.

[2.9] BRICKSTAD, B., and M. BERGMAN, (1996), "Development of safety factors to be used for evaluation of cracked nuclear components", SAQ/FoU-Report 96/07, SAQ Kontroll AB, Stockholm, Sweden.

[2.10] DILLSTRÖM, P., and W. ZANG., (2004), "User manual ProSACC Version 1.0", DNV Research Report 2004/02, Det Norske Veritas AB, Stockholm, Sweden.

TABLE OF REVISIONS

Rev	Activity / Purpose of this revision	Handled by	Date
4-1	First printing of revision 4 of the handbook.	Peter Dillström	2004-10-14

APPENDIX A. DEFECT CHARACTERIZATION

A fracture mechanics assessment requires that the current defect geometry is characterized uniquely. In this appendix general rules for this are given. For additional information it is referred to ASME Boiler and Pressure Vessel Code, Sect. XI [A1].

A1. Defect geometry

Surface defects are characterized as semi-elliptical cracks. Embedded defects are characterized as elliptical cracks. Through thickness defects are characterized as rectangular cracks. The characterizing parameters of the crack are defined as follows:

a) The depth of a surface crack a corresponding to half of the minor axis of the ellipse.

b) The depth of an embedded crack $2a$ corresponding to the minor axis of the ellipse.

c) The length of a crack l corresponding to the major axis of the ellipse for surface and embedded cracks or the side of the rectangle for through thickness cracks.

In case the plane of the defect does not coincide with a plane normal to a principal stress direction, the defect shall be projected on to normal planes of each principal stress direction. The one of these projections is chosen for the assessment that gives the most conservative result according to this procedure.

A2. Interaction between neighbouring defects

When a defect is situated near a free surface or is close to other defects the interaction shall be taken into account. Some cases of practical importance are illustrated in Fig. A1. According to the present rules the defects shall be regarded as one compound defect if the distance *s* satisfies the condition given in the figure. The compound defect size is determined by the length and depth of the geometry described above which circumscribes the defects. The following shall be noted:

a) The ratio *l/a* shall be greater than or equal to 2.

b) In case of surface cracks in cladded surfaces the crack depth should be measured from the free surface of the cladding. If the defect is wholly contained in the cladding the need of an assessment has to be judged on a case-by-case basis.

c) Defects in parallel planes should be regarded as situated in a common plane if the distance between their respective planes is less than 12.7 mm.

Case	Defect sketches	Criterion
1	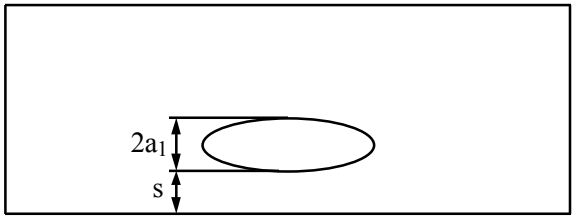	If $s < 0.4a_1$ then $a = 2a_1 + s$
2	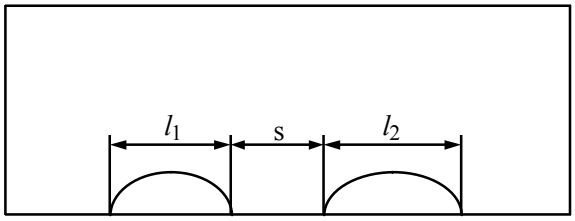	If $s < \min(l_1, l_2)$ then $l = l_1 + l_2 + s$
3	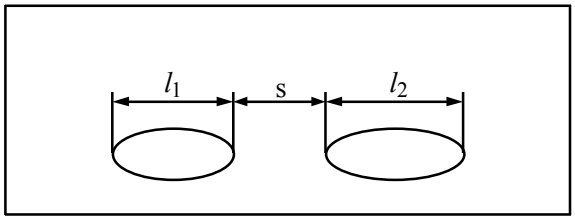	If $s < \min(l_1, l_2)$ then $l = l_1 + l_2 + s$
4	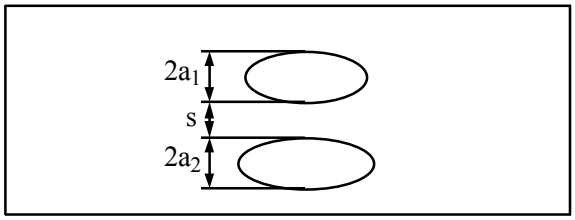	If $s < \max(2a_1, 2a_2)$ then $2a = 2a_1 + 2a_2 + s$
5	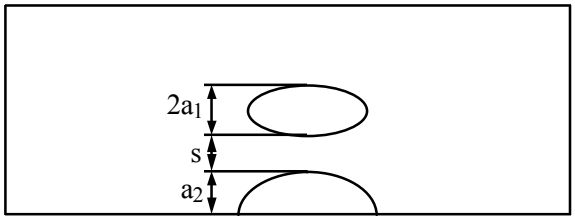	If $s < \max(2a_1, a_2)$ then $a = 2a_1 + a_2 + s$
6	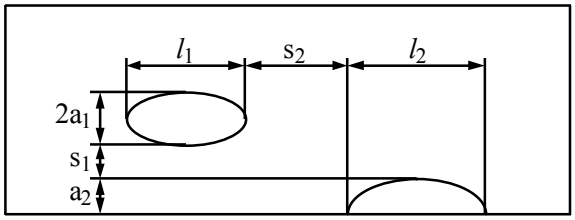	If $s_1 < \max(2a_1, a_2)$ and $s_2 < \min(l_1, l_2)$ then $a = 2a_1 + a_2 + s_1$ $l = l_1 + l_2 + s_2$

Figure A1. Rules for defect characterization at interaction.

A3. References

[A1] —, (1995), *ASME Boiler and Pressure Vessel Code, Sect. XI, Rules for inservice inspection of nuclear power plant components.* The American Society of Mechanical Engineers, New York, U.S.A.

APPENDIX R. RESIDUAL STRESSES

Residual stresses are defined as stresses existing in a structure when it is free from external loading. The distribution and magnitude of residual stresses in a component depend on the fabrication process and service influences. Residual stresses are normally created during the manufacturing stage but can also appear or be redistributed during service. At pressure or load test of a component, peaks of residual stresses can be relaxed due to local plasticity if the total stress level exceeds the yield strength of the material.

It is anticipated that with increasing amount of external load (increasing limit load parameter L_r) the contribution to the risk of fracture from the weld residual stresses is diminished. There is experimental evidence [R1], which demonstrates that for ductile materials, the influence of weld residual stresses on the load carrying capacity is quite low. In [R1] the influence of the weld residual stresses beyond L_r of 1.0 was almost zero. The ASME Code, Section XI, has dealt with this problem by simply ignoring weld residual stresses for certain materials, for instance for austenitic stainless steels. However, this treatment is questionable for situations that is dominated by secondary loads (e.g. for thermal shock loads) and when the material is not sufficiently ductile that the failure mechanism is controlled only by plastic collapse. The Swedish Nuclear Power Inspectorate and Det Norske Veritas has therefore started a project that will lead to a quantitative recommendation on how to treat weld residual stresses for high L_r-values in a R6 fracture assessment. The results from this project will be incorporated in the next revision of the handbook.

Guidelines for estimation of residual stresses in steel components due to welding are given below for use in cases when more precise information is not available. In some cases, welding leads to formation of bainite or martensite at cooling which results in a change in volume. Such a volume change affects the weld residual stresses and makes it difficult to perform accurate predictions. A more comprehensive compendium of residual stress profiles are given in [R2-R4]. The residual stresses are given in the transverse and longitudinal directions, corresponding to stresses normal and parallel to the weld run. Weld residual stresses acting in the through thickness direction are assumed to be negligible.

The magnitude of the residual stresses are expressed in S_r which is set to the 0.2% yield strength of the material at the actual temperature, see Chapter 2.5. For austenitic stainless steels, however, S_r should be chosen to the 1% proof stress at the considered temperature. This is mainly due to the large strain hardening that occurs for stainless steels. If data for the 1% proof stress is missing, it may be estimated as 1.3 times the 0.2% proof stress. The actual yield strength values rather than minimum values should be used for a realistic estimation.

For an overmatched weld joint, the yield strength is referred to the weld material for the residual stress in the longitudinal direction in the weld centerline. For the transverse residual stress, the yield strength is in general referred to the base material.

R1. Butt welded joints

R1.1 Thin plates

With thin plates is here meant plates with butt welds where the variation of the residual stress in the thickness direction is insignificant. This holds for butt welds with only one or a few weld beads.

The weld residual stresses acting in the longitudinal direction of the weld has a distribution across the weld according to Fig. R1. The width of the zone with tensile stresses l is about four to six times the plate thickness. This distribution is obtained along the entire weld except when the weld ends at a free surface where the stresses tend to zero.

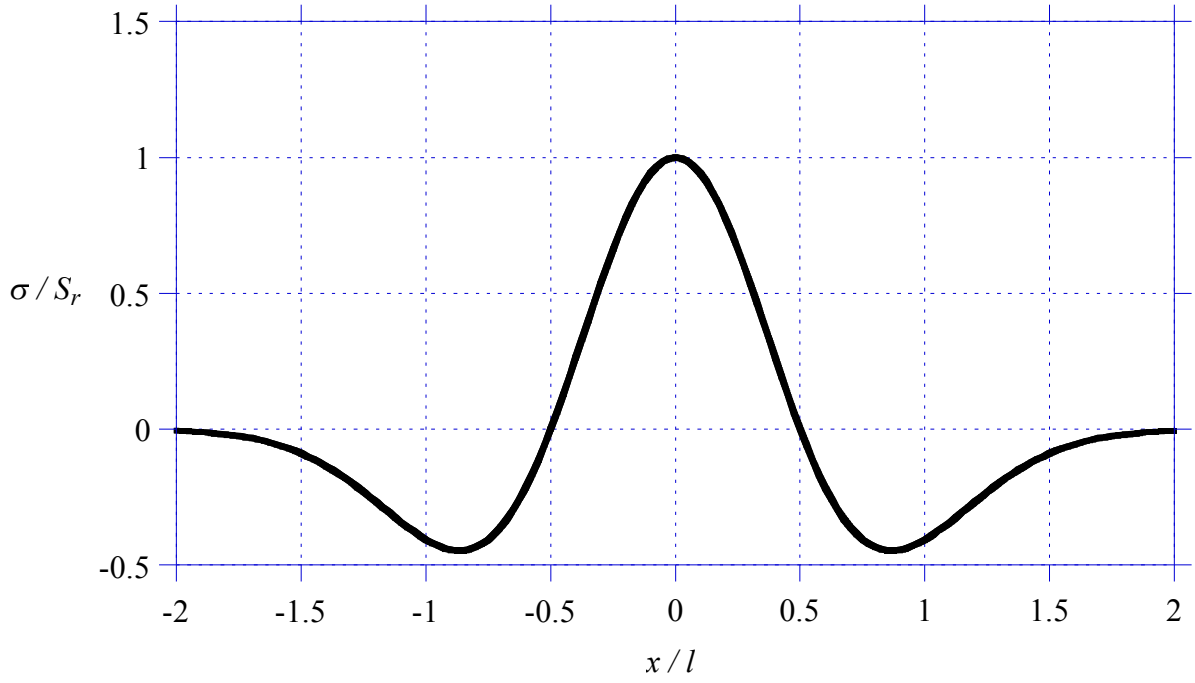

Figure R1. Distribution across the weld of residual stresses acting in the longitudinal direction of the weld.

The magnitude of the weld residual stresses acting transverse to the weld direction is dependent on whether the plates have been free or fixed during welding. If for instance, the plates are fixed to each other by tack welding before the final welding, residual stresses with a magnitude up to S_r are obtained. If one of the two plates is free to move during cooling the residual stresses become limited to $0.2S_r$, see e.g. Ref. [R5]. The values are valid at the centerline of the weld. They successively diminish in sections outside the centerline.

R1.2 Thick plates

In thick plates welded with many weld beads the variation of the residual stresses in the thickness direction cannot be neglected. The stress distribution is much more complicated in thick plates than in thin plates and depends very much on joint design and weld method. It is therefore difficult to give simple general guidelines for estimation of residual stresses in thick plates. It is not possible to give a specific value of the plate thickness that represents the transition from a thin to a thick plate. For more detailed information, see Refs. [R2, R6-R8].

The weld residual stresses acting in the weld vary both in the thickness direction and across the weld. The highest stress in the symmetry plane of the weld is S_r. The simplest but in many cases very conservative assumption is that the weld residual stress is constant and equal to S_r throughout the entire thickness.

In a symmetric joint, for instance an X-joint or a double U-joint with many weld beads, the residual stress through the thickness t varies as shown in Fig. R2.

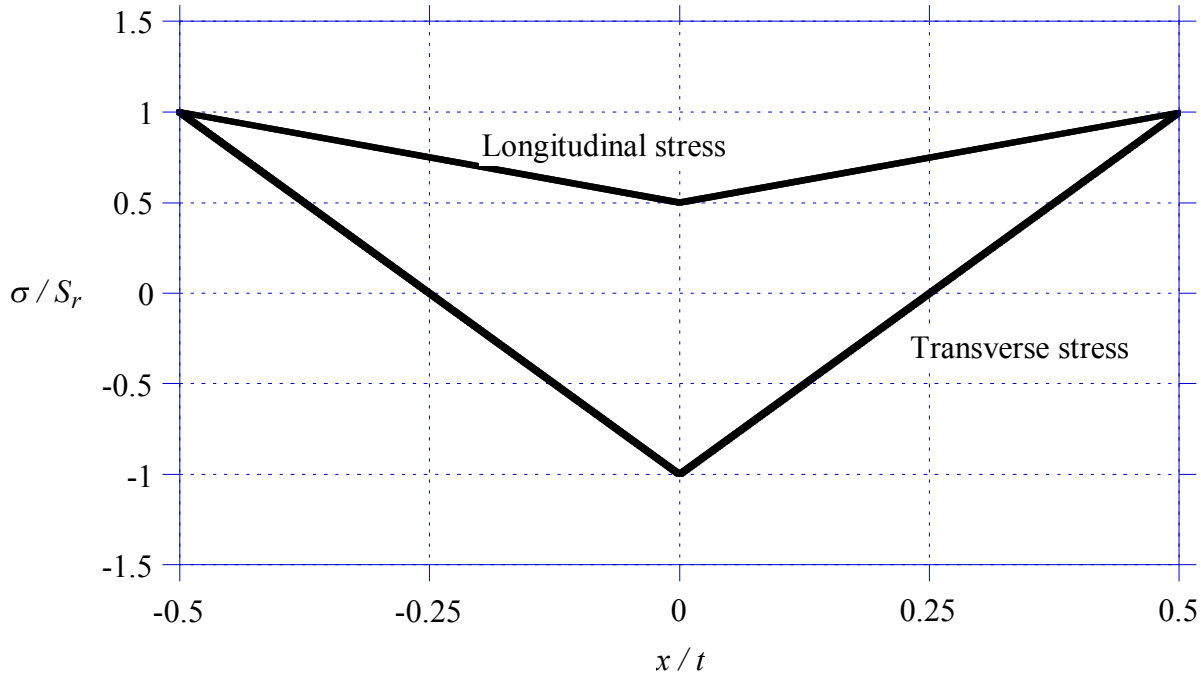

Figure R2. Thickness distribution of residual stresses acting in a welded thick plate in a symmetric joint with many weld beads. This distribution for residual stresses acting transverse the weld applies for a free plate.

The weld residual stresses acting transverse the weld vary as shown in Fig. R2 if any of the plates is free to move during the cooling.

R1.3 Butt welded pipes

The residual stress distribution in girth welds in both thick walled and thin walled pipes are complicated and depends on joint shape, weld method, heat input, wall thickness and pipe radius. The recommendations given here are based on a numerical investigation on austenitic stainless steel pipes [R9] and apply to girth welds applied from the outside (single sided V- or U-preparation). They are valid for a radius to thickness ratio R_i / t of approximately 8 but can conservatively be used for higher ratios of R_i / t. The heat input relative to the pipe thickness was between 75 and 101 MJ/m^2 which is considered to be high. More detailed information is given in [R9]. A parametric study of a large number of pipes can also be found in [R10].

The local residual stresses acting longitudinal and transverse to a girth weld are shown in Fig. R3 for a pipe thickness up to 30 mm. The stresses decrease successively in sections further outside the fusion line.

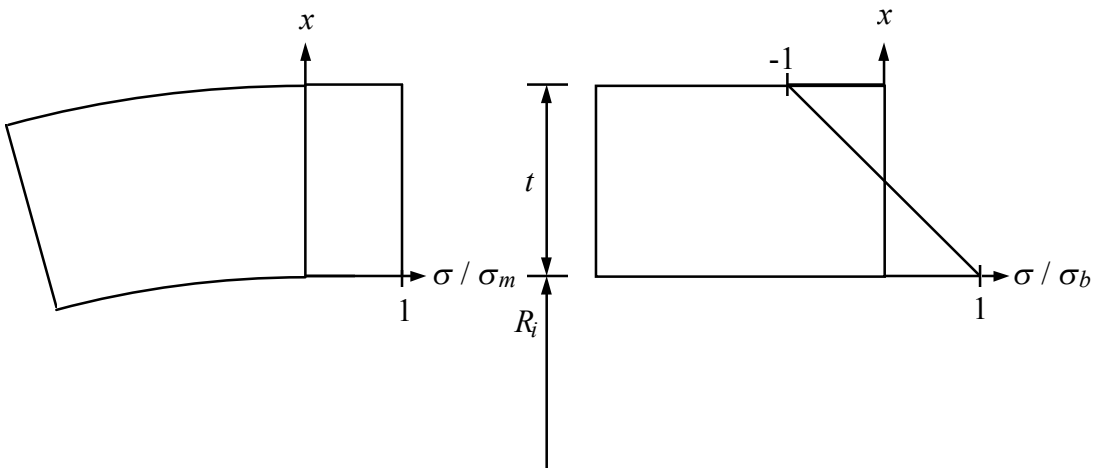

Figure R3. Local distribution of residual stress acting longitudinal and transverse to a girth weld for an austenitic pipe up to a thickness of 30 mm.

In Table R1 the specific values of the membrane stress σ_m and local bending stress σ_b are given. They are taken from [R9] and determined at 288 °C which is a common operating temperature for nuclear LWR plants.

The local residual stresses acting longitudinal and transverse to a girth weld are shown in Fig. R4, for a pipe thickness greater than 30 mm. The stresses decrease successively in sections further outside the fusion line.

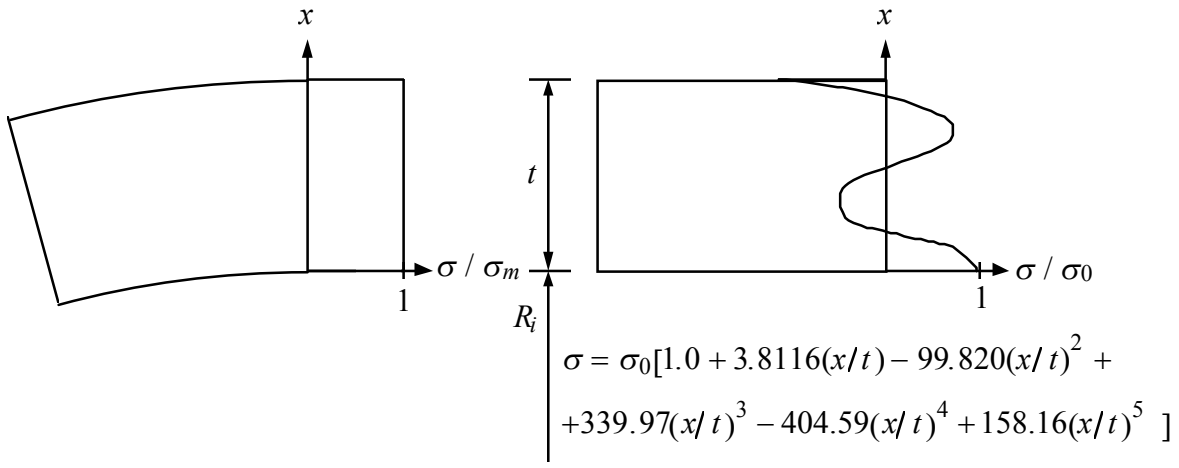

Figure R4. Local distribution of residual stress acting longitudinal and transverse to a girth weld for an austenitic pipe with a thickness greater than 30 mm.

In Table R1 the specific values of the membrane stress σ_m and stress amplitude σ_0 are given. They are determined at 288 °C.

In [R9] the stainless steel pipes considered were overmatched with a weld material yield strength at 1% strain of 348 MPa and base material yield strength at 1% strain of 187 MPa at 288 °C. S_r in Table R1 is referred to the 1% proof stress at 288 °C for the base material except for the longitudinal stress at the weld centerline where S_r is referred to the 1% proof stress of the weld material. For other combinations of weld and base material yield properties, appropriate adjustments of these recommendations can be made according to Table R1.

Pipes with a thickness up to 40 mm were studied in [R9]. For a pipe wall thickness greater than this, the recommendations in Table R1 should be conservative.

Table R1. Recommended longitudinal and transverse residual stress distributions for austenitic stainless steel pipe welds at 288 °C. $x = 0$ at the inside of the pipe wall. See Figs. R3 and R4.

Transverse stress [MPa]	
t [mm]	Weld centerline and HAZ
$t \le 7$	$1.219\,S_r\,[1 - 2(x/t)]$
$7 < t \le 25$	$(1.5884 - 0.05284t)\;S_r\,[1 - 2(x/t)]$
$25 < t \le 30$	$0.2674\,S_r\,[1 - 2(x/t)]$
$t > 30$	$0.4246\,S_r\,[1 + 3.8116(x/t) - 99.82(x/t)^2 + 339.97(x/t)^3 - 404.59(x/t)^4 + 158.16(x/t)^5]$

Longitudinal stress [MPa]		
t [mm]	Weld centerline	HAZ
$t \le 30$	$0.925\,S_r$	$0.861\,S_r$
$t > 30$	$0.925\,S_r$	$0.646\,S_r$

For ferritic steel piping, predictions based on numerical methods are more difficult due to volume changes during certain phase transformations. Based on the investigation in [R10], the principal feature for the residual stresses for girth welds should be similar as for austenitic piping. Thus if no other data for a specific case exists, it is proposed to use Table R1 also for ferritic piping. Proper adjustment has to be made for the actual yield properties of the ferritic pipe weld. Also, the bending stress σ_b for thinner pipes in Table R1, should be limited to the yield strength for a ferritic pipe.

R1.4 Butt-welded bimetallic pipes (V or U shape)

The recommendations of the residual stress distribution given here are based on a numerical investigation [R3-R4] and apply to girth welds applied from the outside (single sided V- or U-preparation), see Fig. R5. It is shown that the material at HAZ has little influence on residual stress. The position (left or right) decides the magnitude and the distribution of the residual stress.

Weld type (a)

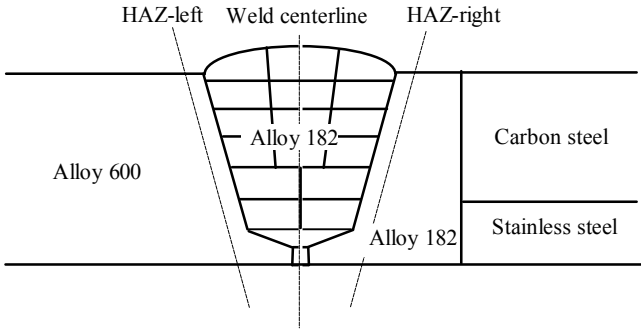

Weld type (b)

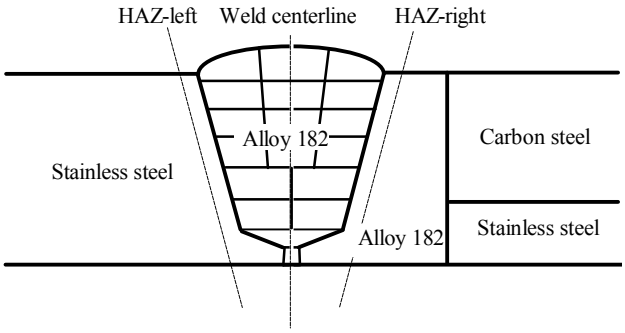

Weld type (c)

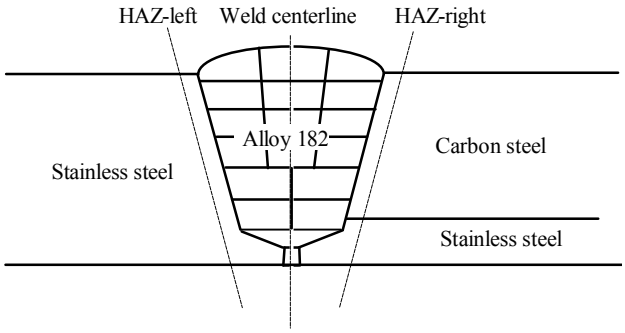

Weld type (d)

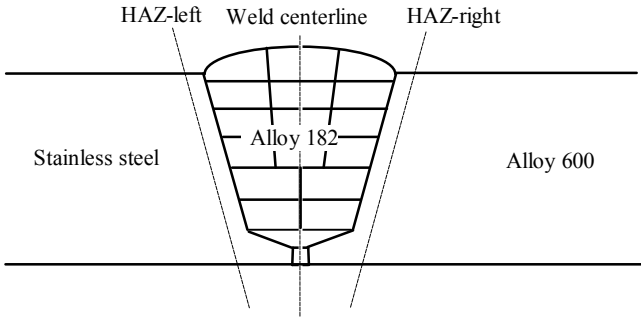

Figure R5. Butt-welded bimetallic pipes (single sided V- or U-preparation).

The weld residual stress across the thickness is fitted by a 5-th degree polynomial as,

$$\sigma = \left\{ c_0 + \sum_{i=1}^{5} c_i \left(\frac{u}{t} \right)^i \right\} \text{ MPa} \ , \qquad \text{(R1)}$$

where u = 0 indicates the inside surface of the pipe and t the thickness of the pipe. The parameters for the recommended weld residual stresses are presented in Tables R2 and R3 at three different cross lines, namely at the weld centre line, the HAZ left line and the HAZ right line. The stress distributions are also plotted in Fig. R6 and R7.

Table R2. Recommended transverse residual stress for butt-welded bimetallic pipes.

Position	***t* [mm]**	c_0	c_1	c_2	c_3	c_4	c_5
HAZ left	$t < 10$	245.0	539.8	-5734.5	12197.	-11190.	3849.1
Weld centre		171.2	1257.6	-7048.2	11265.	-8498.5	2570.4
HAZ right		253.4	188.3	-4357.1	7951.5	-5555.0	1396.4
HAZ left	$10 < t \leq \leq 20$	129.3	26.2	-2066.3	7944.4	-11395.	5175.9
Weld centre		124.1	934.6	-9166.4	24979.	-28074.	11005.
HAZ right		149.9	-800.3	1694.4	-2322.8	1724.8	-477.1
HAZ left	$20 < t \leq \leq 30$	52.4	66.6	-5063.3	21002.	-28115.	11925.
Weld centre		100.7	-50.1	-5156.3	18102.	-20949.	7833.0
HAZ right		140.2	-1192.8	1868.0	1848.7	-6318.7	3782.3
HAZ left	$30 < t \leq \leq 70$	33.0	-466.4	-4326.5	21424.	-27647.	10915.
Weld centre		32.9	-177.4	-5280.1	20579.	-24143.	8986.1
HAZ right		102.3	-1682.4	4191.1	-610.9	-6619.8	4881.2

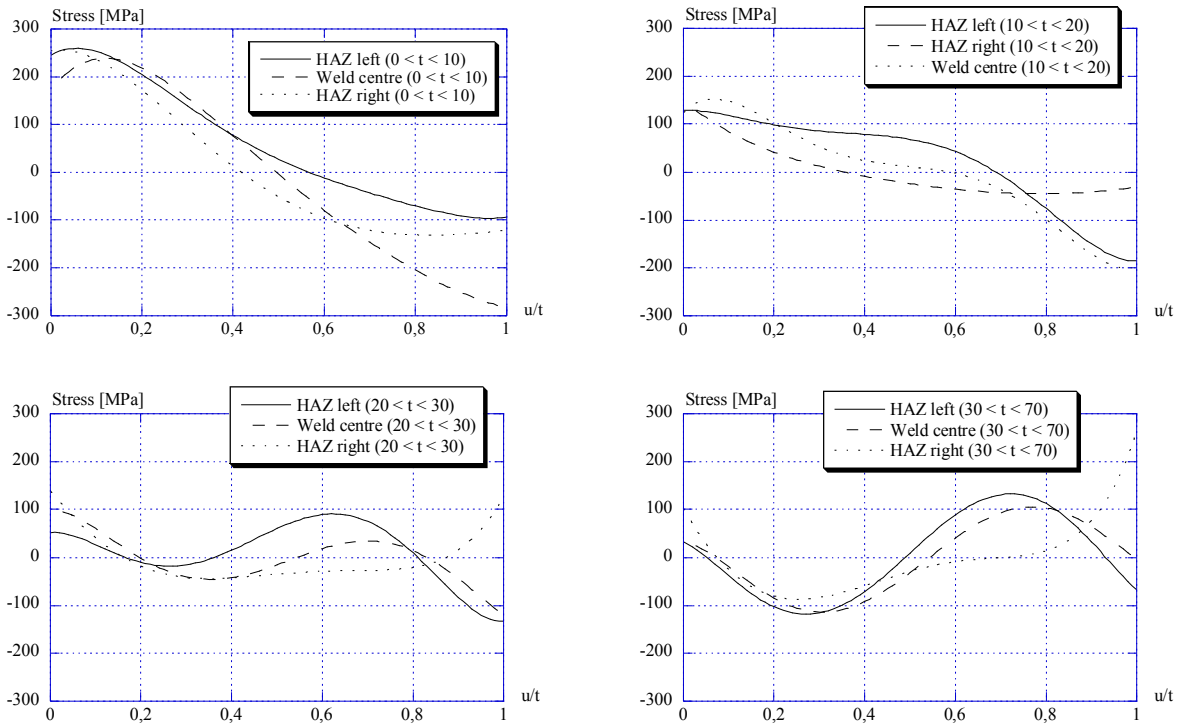

Figure R6. Recommended transverse residual stress for butt-welded bimetallic pipes.

Table R3. Recommended longitudinal (hoop) residual stress for butt-welded bimetallic pipes.

Position	***t* [mm]**	c_0	c_1	c_2	c_3	c_4	c_5
HAZ left	$t < 10$	187.9	38.7	107.8	-1831.0	1993.9	-512.8
Weld centre		371.6	451.6	-1071.9	-1044.7	2504.2	-1151.1
HAZ right		197.8	523.3	-806.1	-2881.9	5462.9	-2457.7
HAZ left	$10 < t \leq \leq 20$	248.2	297.3	-1696.1	5125.5	-7120.0	3173.0
Weld centre		386.1	671.7	-6490.3	17792.	-19862.	7662.3
HAZ right		170.4	-315.5	1117.5	-1624.8	745.4	-14.3
HAZ left	$20 < t \leq \leq 30$	252.2	-231.7	-354.8	5424.9	-9185.7	4174.3
Weld centre		172.5	-658.2	2458.6	-159.7	-3635.1	2046.1
HAZ right		89.9	-596.9	4191.8	-6975.5	3644.5	242.7
HAZ left	$30 < t \leq \leq 70$	16.4	-605.3	812.7	9426.8	-18206.	8689.4
Weld centre		88.7	170.4	-2984.4	13346.	-17190.	6833.8
HAZ right		91.9	273.8	-2184.1	11029.	-16671.	7719.9

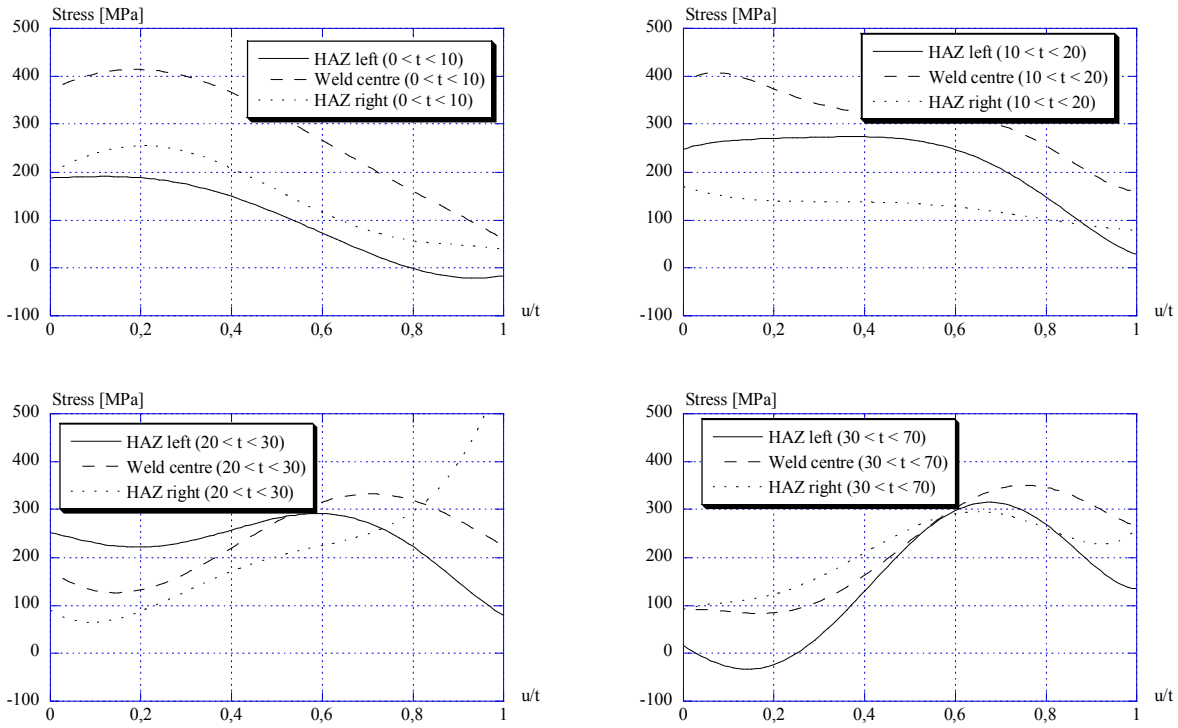

Figure R7. Recommended longitudinal (hoop) residual stress for butt-welded bimetallic pipes.

R1.5 Butt-welded bimetallic pipes (X shape)

The following weld configuration has been considered, see Fig. R8. The thickness of the pipe is 84 mm, the inner radius of the pipe is 348.5 mm and the distance D in the figure is 36 mm. The recommend residual stresses are fitted by a 5-th degree polynomial Eq. (R1). The parameters for weld residual stresses are presented in Table R4 at three different cross lines, namely at the weld centre line, the HAZ left line and the HAZ right line. The stress distributions are also plotted in Fig. R9.

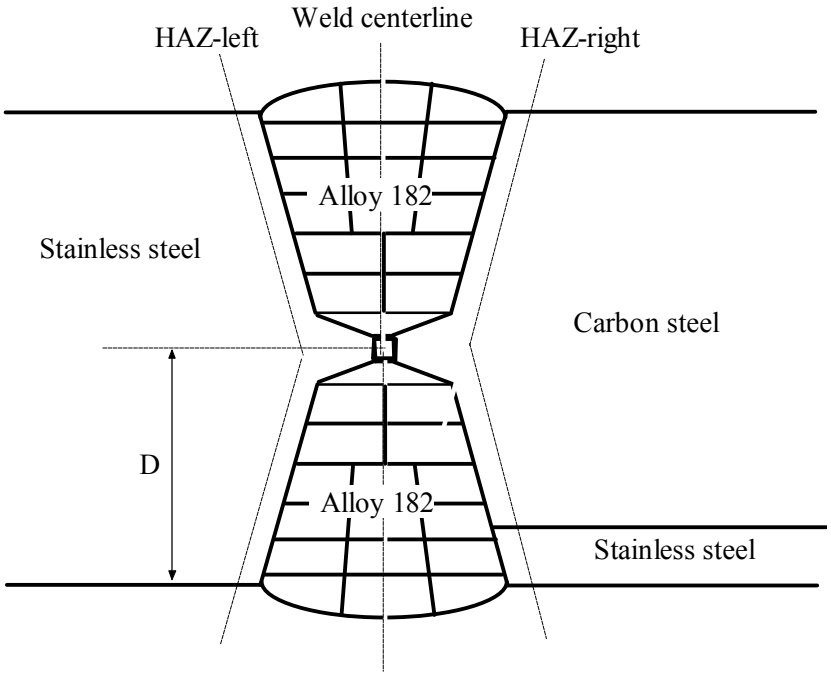

Figure R8. Butt-welded bimetallic pipes (X shape).

Table R4. Recommended residual stress for butt-welded bimetallic pipes (X-shape).

Position	**Direction**	c_0	c_1	c_2	c_3	c_4	c_5
HAZ left	Transverse	16.5	-114.9	-2052.7	10852.	-15613.	6868.6
Weld centre		-45.9	3302.7	-28043.	79894.	-89816.	34593.
HAZ right		96.1	-2029.1	13368.	-35634.	41989.	-17763.
HAZ left	Longitudinal	81.2	22.1	1054.1	-2661.1	2986.8	-1603.7
Weld centre		152.8	1151.1	-11255.	41225.	-53695.	22684.
HAZ right		-51.2	3279.2	-10251.	12270.	-3062.4	-1864.4

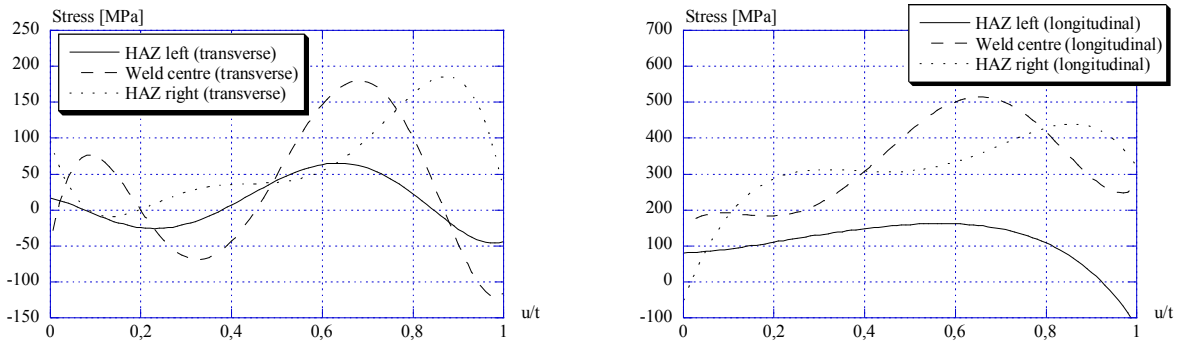

Figure R9. Recommended residual stress for butt-welded bimetallic pipes (X-shape).

R1.6 Pipe seam welds

The residual stresses acting longitudinal and transverse to a seam weld can approximately be estimated from the corresponding distribution in a plate if the pipe is not adjusted with respect to roundness after welding.

R2. Fillet welds

The residual stresses acting both along and across a fillet weld amount to S_r. The stresses decrease outside the fillet weld.

R3. Stress relieved joints

In correctly stress relieved joints the maximum residual stress decreases to 0.15-0.20 S_r. Micro alloyed steels are sometimes stress relieved at temperatures lower than 560 °C. The relaxation is in such cases not so effective and the remaining residual stress is larger than 0.2 S_r.

Local stress relief that sometimes is used gives a result that is more difficult to assess.

R4. Summary

The above given guidelines for estimation of residual stresses are summarized in Table R5.

Table R5. Estimation of residual stresses in welded joints.

Type of joint	Thickness	Residual stress, longitudinal	Residual stress, transverse
Butt weld in a plate	Thin plate with only a few weld beads	Fig. R1	$\leq S_r$, fixed plate $\leq 0.2S_r$, free plate
	Thick plate with many weld beads, symmetric X-joint	Fig. R2	Fig. R2
Butt weld in a pipe, girth weld	Thin ($\leq$ 30 mm)	Fig. R3 and Table R1	Fig. R3 and Table R1
	Thick (> 30 mm)	Fig. R4 and Table R1	Fig. R4 and Table R1
Butt weld bimetallic pipes (V or U shape)		Fig. R5 and Table R2	Fig. R5 and Table R3
Butt weld bimetallic pipes (X shape)	Thick (> 80 mm)	Fig. R6 and Table R4	Fig. R6 and Table R4
Butt weld in a pipe, seam weld	Thin	See thin plate	See thin plate
	Thick	See thick plate	See thick plate
Fillet weld		$\leq S_r$	$\leq S_r$
Stress relieved weld		$\leq 0.2S_r$	$\leq 0.2S_r$

S_r = 0.2% proof stress for ferritic steels and 1% proof stress for austenitic stainless steels at the temperature of assessment.

R5. References

[R1] SHARPLES, J. K., SANDERSON, D. J., BOWDLER, B. R., WIGHTMAN, A. P. and R. A. AINSWORTH, (1995), ”Experimental programme to assess the effect of residual stresses on fracture behaviour”, *Proceedings of the 1995 ASME Pressure Vessels & Piping Conference*, V. 437, pp. 539-551.

[R2] —, (2003), ”Assessment of the Integrity of Structures Containing Defects”, R6 – Revision 4, Up to amendment record No.2, British Energy Generation Ltd.

[R3] DELFIN, P., and B. BRICKSTAD, (1998), ”Residual stresses in multi-pass butt-welded bimetallic piping, Part I”, SAQ/FoU-Report 98/12, SAQ Kontroll AB, Stockholm, Sweden.

[R4] DELFIN, P., and B. BRICKSTAD, (1999), ”Residual stresses in multi-pass butt-welded bimetallic piping, Part II”, SAQ/FoU-Report 99/06, SAQ Kontroll AB, Stockholm, Sweden.

[R5] ANDERSSON, B., and L. KARLSSON, (1981), ”Thermal stresses in large butt-welded plates”, *J. Thermal Stresses*, Vol. 4, pp. 491-500.

[R6] UEDA, Y., TAKAHASHI, E., SAKAMOTO, K. and K. NAKACHO, (1976), ”Multipass welding stresses in very thick plates and their reduction from stress relief annealing”, *Trans. JWRI*, Vol. 5, No. 2, pp. 79-88.

[R7] UEDA, Y., and K. NAKACHO, (1986), ”Distribution of welding residual stresses in various welded joints of thick plates”, *Trans. JWRI*, Vol. 15, No. 1.

[R8] RUND, C. O., and P. S DIMASCO, (1981), ”A prediction of residual stresses in heavy plate butt welds”, *J. Materials for Energy Systems*, Vol. 3, pp. 62-65.

[R9] BRICKSTAD, B., and L. JOSEFSON, (1996), ”A parametric study of residual stresses in multipass butt-welded stainless steel pipes”, SAQ/FoU-Report 96/01, SAQ Kontroll AB, Stockholm, Sweden.

[R10] SCARAMANGAS, A., (1984), ”Residual stresses in girth butt weld pipes”, Technical Report No. CUED/D-Struct./TR. 109, Dept. of Engineering, Cambridge University, U.K.

APPENDIX G. GEOMETRIES TREATED IN THIS HANDBOOK

G1. Cracks in a plate

G1.1 Finite surface crack

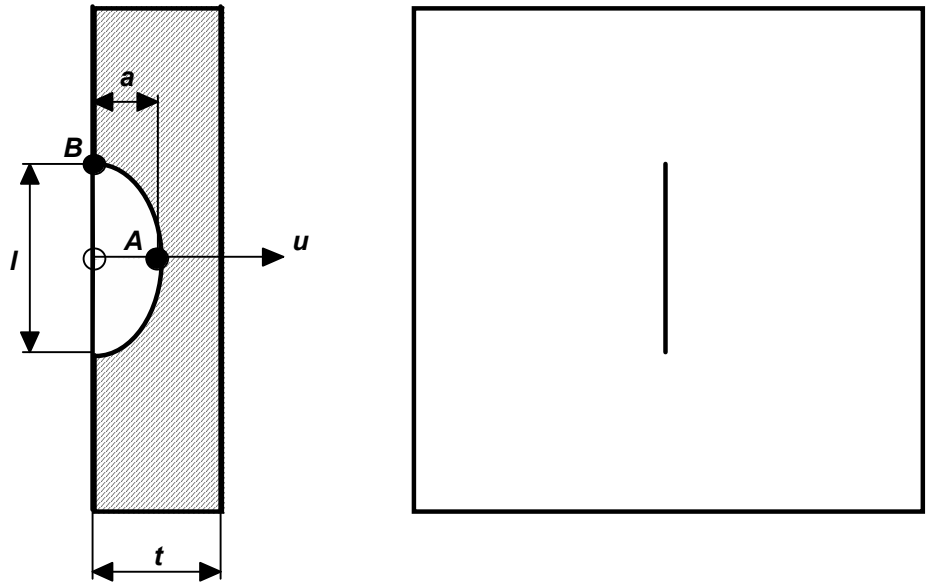

Figure G1.1. Finite surface crack in a plate.

G1.2 Infinite surface crack

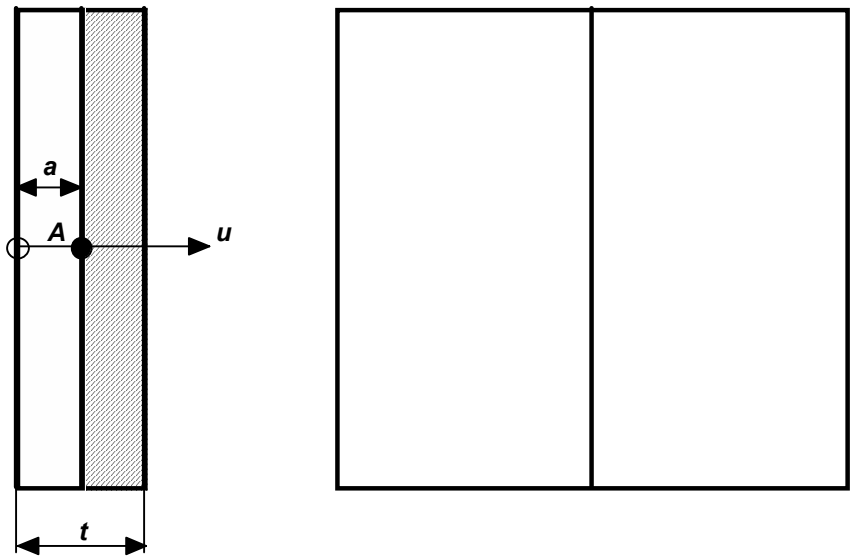

Figure G1.2. Infinite surface crack in a plate.

G1.3 Embedded crack

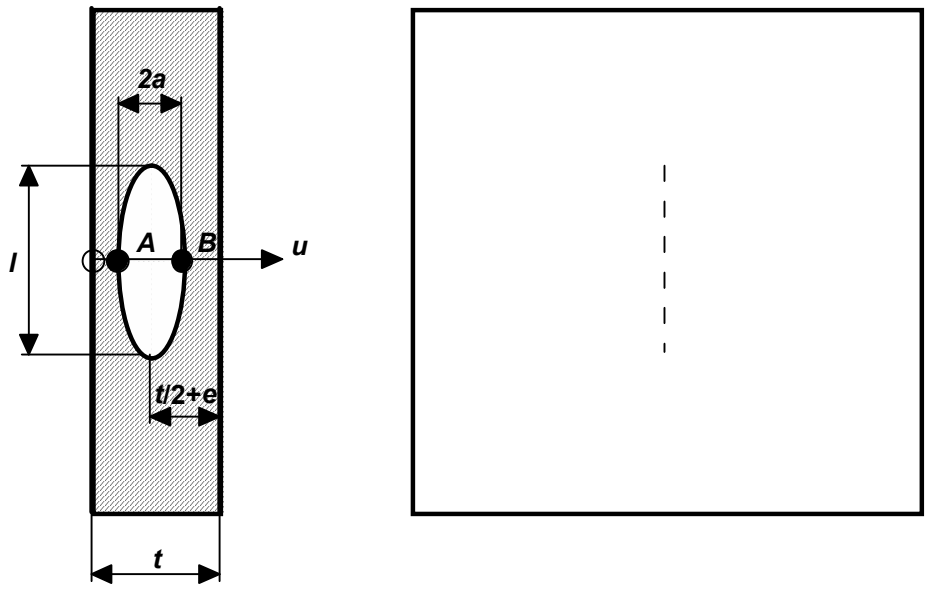

Figure G1.3. Embedded crack in a plate.

G1.4 Through-thickness crack

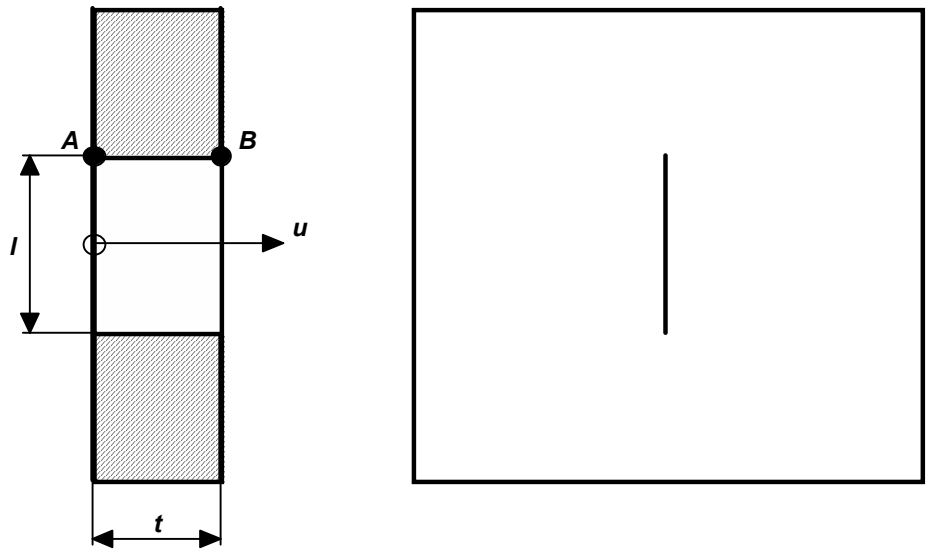

Figure G1.4. Through-thickness crack in a plate.

G2. Axial cracks in a cylinder

G2.1 Finite internal surface crack

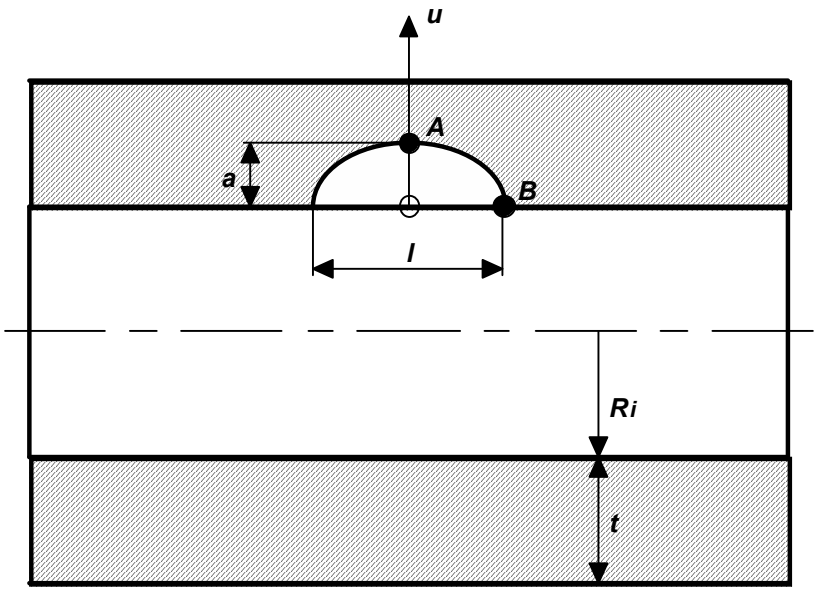

Figure G2.1. Finite axial internal surface crack in a cylinder.

G2.2 Infinite internal surface crack

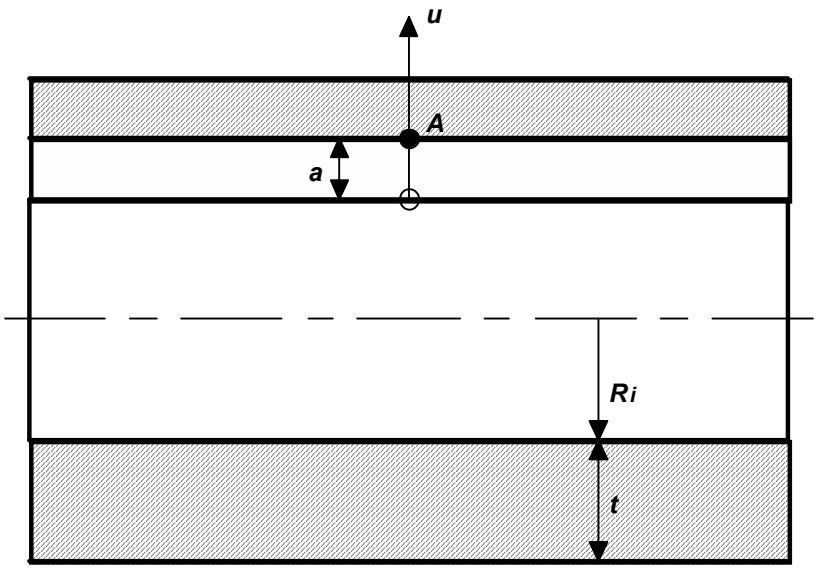

Figure G2.2. Infinite axial internal surface crack in a cylinder.

G2.3 Finite external surface crack

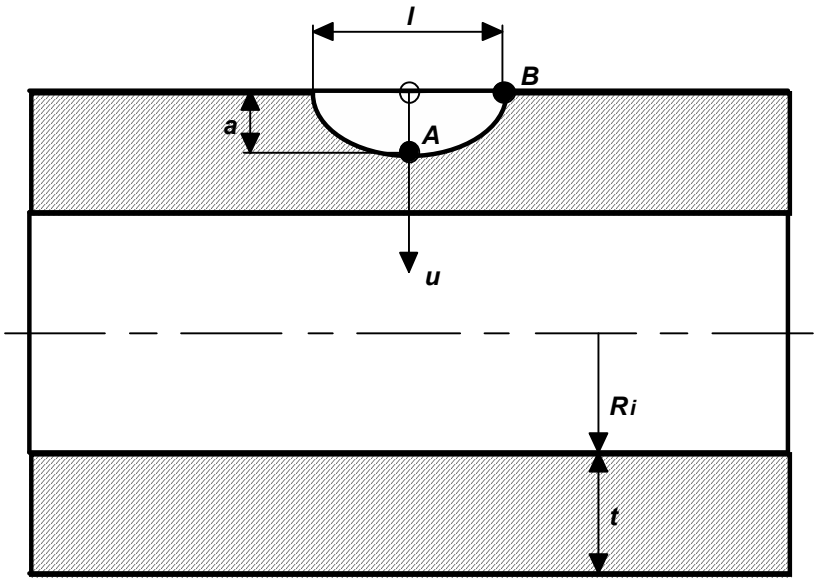

Figure G2.3. Finite axial external surface crack in a cylinder.

G2.4 Infinite external surface crack

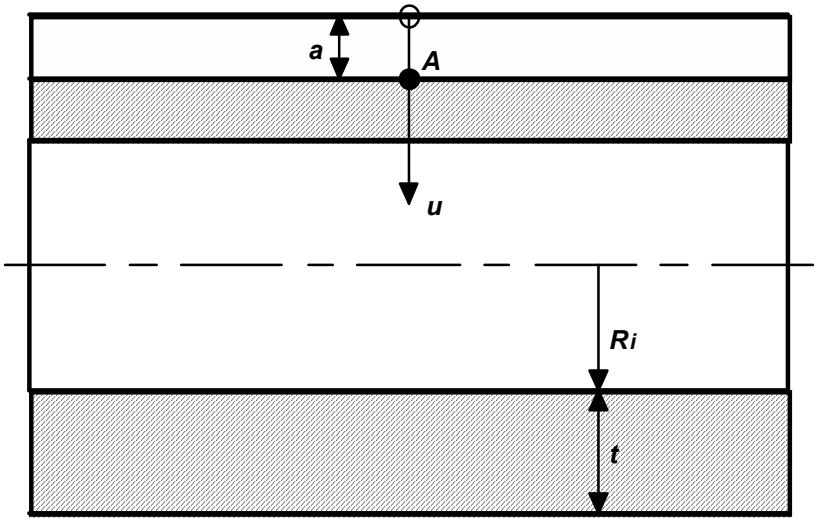

Figure G2.4. Infinite axial external surface crack in a cylinder.

G2.5 Through-thickness crack

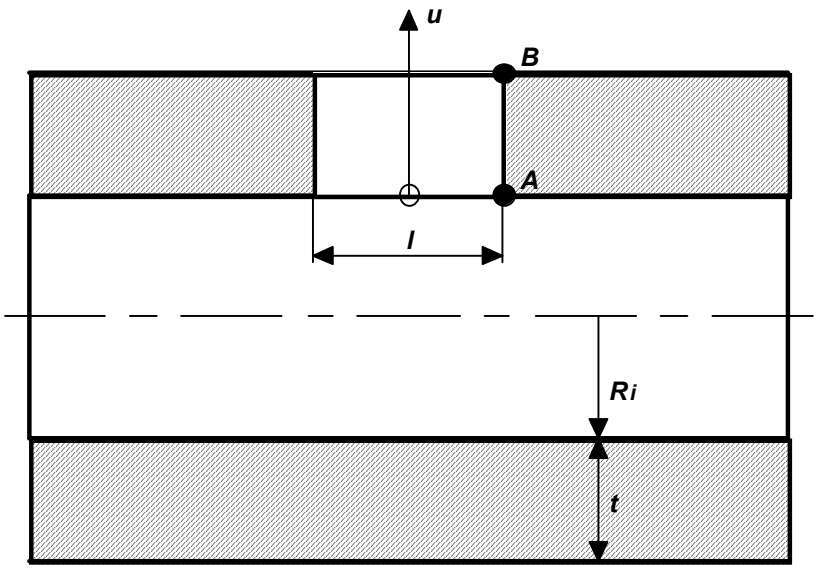

Figure G2.5. Axial through-thickness crack in a cylinder.

G3. Circumferential cracks in a cylinder

G3.1 Part circumferential internal surface crack

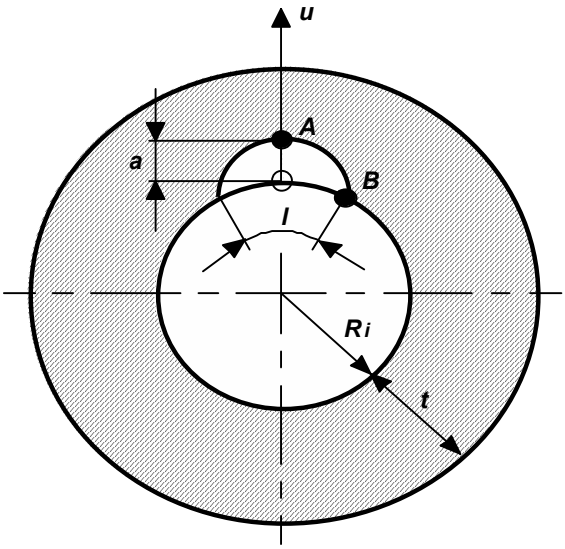

Figure G3.1. Part circumferential internal surface crack in a cylinder.

G3.2 Complete circumferential internal surface crack

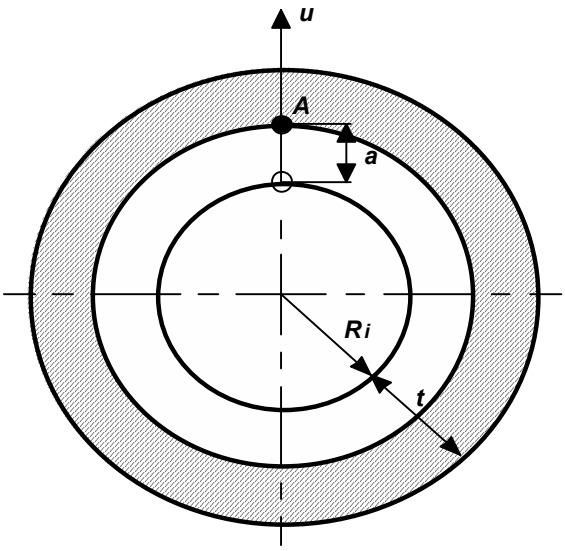

Figure G3.2. Complete circumferential internal surface crack in a cylinder.

G3.3 Part circumferential external surface crack

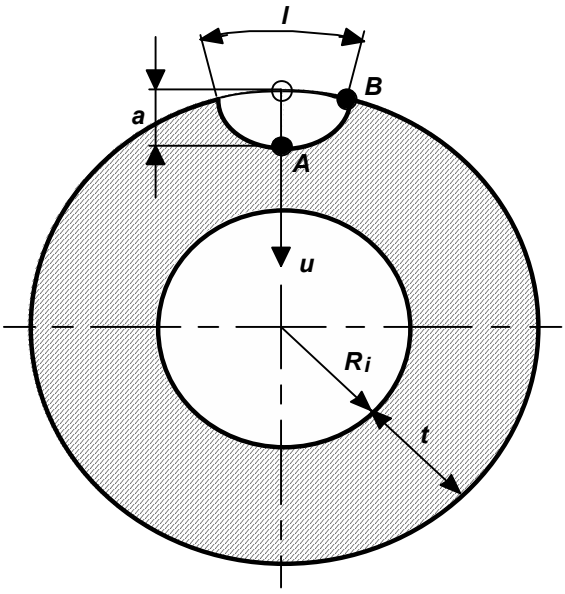

Figure G3.3. Part circumferential external surface crack in a cylinder.

G3.4 Complete circumferential external surface crack

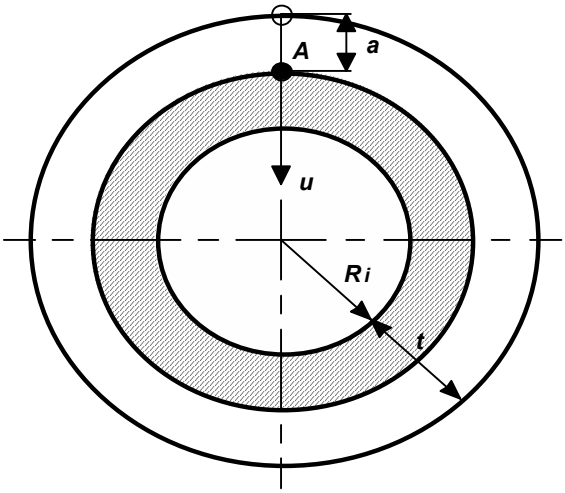

Figure G3.4. Complete circumferential external surface crack in a cylinder.

G3.5 Through-thickness crack

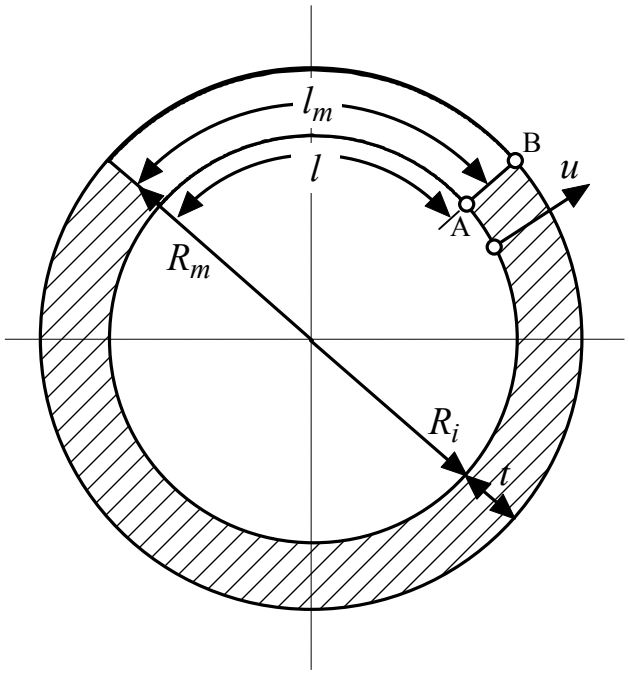

Figure G3.5. Circumferential through-thickness crack in a cylinder.

G4. Cracks in a sphere

G4.1 Through-thickness crack

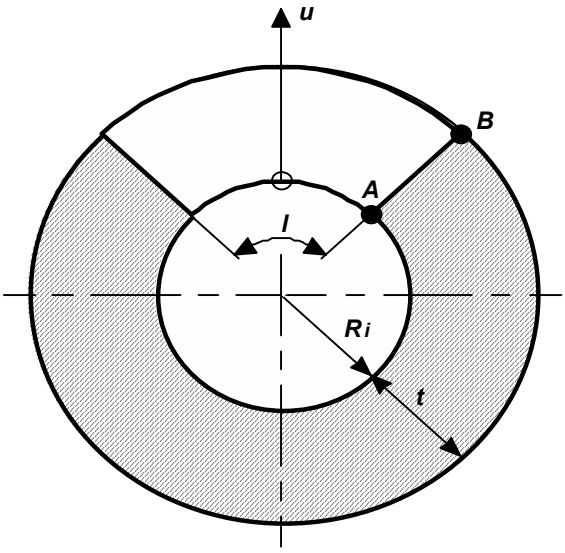

Figure G4.1. Circumferential through-thickness crack in a sphere.

G5. Cracks in a bar

G5.1 Part circumferential surface crack

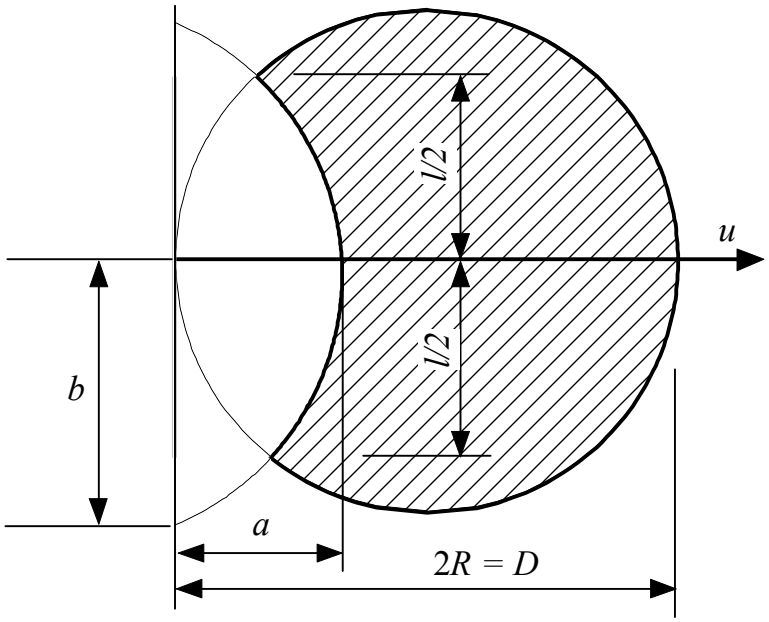

Figure G5.1. Part circumferential surface crack in a cylindrical bar.

APPENDIX K. STRESS INTENSITY FACTOR SOLUTIONS

K1. Cracks in a plate

K1.1 Finite surface crack

K_I is given by

$$K_I = \sqrt{\pi a}\sum_{i=0}^{5}\sigma_i f_i\left(a/t, l/a\right) \quad . \tag{K1}$$

σ_i (i = 0 to 5) are stress components which define the stress state σ according to

$$\sigma = \sigma(u) = \sum_{i=0}^{5}\sigma_i\left(\frac{u}{a}\right)^i \qquad \text{for } 0 \le u \le a\,. \tag{K2}$$

σ is to be taken normal to the prospective crack plane in an uncracked plate. σ_i is determined by fitting σ to Eq. (K2). The coordinate u is defined in Fig. G1.1.

f_i (i = 0 to 5) are geometry functions which are given in Tables K1 and K2 for the deepest point of the crack (f_i^A), and at the intersection of the crack with the free surface (f_i^B), respectively. See Fig. G1.1.

Remark: The plate should be large in comparison to the length of the crack so that edge effects do not influence the results.

Ref.: [K1-K2].

Table K1-1. Geometry functions for a finite surface crack in a plate — deepest point of the crack ($2 \le l/a \le 5$).

$l/a = 2$						
a/t	f_0^A	f_1^A	f_2^A	f_3^A	f_4^A	f_5^A
0	0.659	0.471	0.387	0.337	0.299	0.266
0.2	0.663	0.473	0.388	0.337	0.299	0.269
0.4	0.678	0.479	0.390	0.339	0.300	0.271
0.6	0.692	0.486	0.396	0.342	0.304	0.274
0.8	0.697	0.497	0.405	0.349	0.309	0.278
$l/a = 5/2$						
a/t	f_0^A	f_1^A	f_2^A	f_3^A	f_4^A	f_5^A
0	0.741	0.510	0.411	0.346	0.300	0.266
0.2	0.746	0.512	0.413	0.352	0.306	0.270
0.4	0.771	0.519	0.416	0.356	0.309	0.278
0.6	0.800	0.531	0.422	0.362	0.317	0.284
0.8	0.820	0.548	0.436	0.375	0.326	0.295
$l/a = 10/3$						
a/t	f_0^A	f_1^A	f_2^A	f_3^A	f_4^A	f_5^A
0	0.833	0.549	0.425	0.351	0.301	0.267
0.2	0.841	0.554	0.430	0.359	0.309	0.271
0.4	0.885	0.568	0.442	0.371	0.320	0.285
0.6	0.930	0.587	0.454	0.381	0.331	0.295
0.8	0.960	0.605	0.476	0.399	0.346	0.310
$l/a = 5$						
a/t	f_0^A	f_1^A	f_2^A	f_3^A	f_4^A	f_5^A
0	0.939	0.580	0.434	0.353	0.302	0.268
0.2	0.957	0.595	0.446	0.363	0.310	0.273
0.4	1.057	0.631	0.475	0.389	0.332	0.292
0.6	1.146	0.668	0.495	0.407	0.350	0.309
0.8	1.190	0.698	0.521	0.428	0.367	0.324

Table K1-2. Geometry functions for a finite surface crack in a plate — deepest point of the crack ($10 \le l/a \le \infty$).

$l/a = 10$						
a/t	f_0^A	f_1^A	f_2^A	f_3^A	f_4^A	f_5^A
0	1.053	0.606	0.443	0.357	0.302	0.269
0.2	1.106	0.640	0.467	0.374	0.314	0.277
0.4	1.306	0.724	0.525	0.420	0.348	0.304
0.6	1.572	0.815	0.571	0.448	0.377	0.327
0.8	1.701	0.880	0.614	0.481	0.399	0.343
$l/a = 32$						
a/t	f_0^A	f_1^A	f_2^A	f_3^A	f_4^A	f_5^A
0	1.070	0.641	0.496	0.418	0.367	0.330
0.2	1.240	0.716	0.541	0.451	0.394	0.353
0.4	1.680	0.876	0.623	0.499	0.426	0.376
0.6	2.453	1.148	0.764	0.585	0.482	0.416
0.8	3.316	1.453	0.924	0.685	0.552	0.467
$l/a = 60$						
a/t	f_0^A	f_1^A	f_2^A	f_3^A	f_4^A	f_5^A
0	1.076	0.646	0.499	0.421	0.369	0.332
0.2	1.284	0.736	0.553	0.459	0.400	0.358
0.4	1.825	0.935	0.657	0.522	0.443	0.389
0.6	2.896	1.316	0.856	0.645	0.525	0.448
0.8	4.519	1.872	1.142	0.820	0.644	0.535
$l/a \to \infty$						
a/t	f_0^A	f_1^A	f_2^A	f_3^A	f_4^A	f_5^A
0	1.123	0.682	0.524	0.440	0.386	0.344
0.2	1.380	0.784	0.582	0.478	0.414	0.369
0.4	2.106	1.059	0.735	0.578	0.485	0.423
0.6	4.025	1.750	1.105	0.814	0.651	0.548
0.8	11.92	4.437	2.484	1.655	1.235	0.977

Table K2-1. Geometry functions for a finite surface crack in a plate — intersection of crack with free surface ($2 \le l/a \le 5$).

$l/a = 2$						
a/t	f_0^B	f_1^B	f_2^B	f_3^B	f_4^B	f_5^B
0	0.716	0.118	0.041	0.022	0.014	0.010
0.2	0.729	0.123	0.045	0.023	0.014	0.010
0.4	0.777	0.133	0.050	0.026	0.015	0.011
0.6	0.839	0.148	0.058	0.029	0.018	0.012
0.8	0.917	0.167	0.066	0.035	0.022	0.015
$l/a = 5/2$						
a/t	f_0^B	f_1^B	f_2^B	f_3^B	f_4^B	f_5^B
0	0.730	0.124	0.041	0.021	0.013	0.010
0.2	0.749	0.126	0.046	0.023	0.014	0.010
0.4	0.795	0.144	0.054	0.028	0.017	0.012
0.6	0.901	0.167	0.066	0.033	0.021	0.015
0.8	0.995	0.193	0.076	0.042	0.026	0.017
$l/a = 10/3$						
a/t	f_0^B	f_1^B	f_2^B	f_3^B	f_4^B	f_5^B
0	0.723	0.118	0.039	0.019	0.011	0.008
0.2	0.747	0.125	0.044	0.022	0.014	0.010
0.4	0.803	0.145	0.056	0.029	0.018	0.012
0.6	0.934	0.180	0.072	0.037	0.023	0.016
0.8	1.070	0.218	0.087	0.047	0.029	0.020
$l/a = 5$						
a/t	f_0^B	f_1^B	f_2^B	f_3^B	f_4^B	f_5^B
0	0.673	0.104	0.032	0.015	0.009	0.006
0.2	0.704	0.114	0.038	0.018	0.011	0.007
0.4	0.792	0.139	0.053	0.027	0.016	0.011
0.6	0.921	0.183	0.074	0.038	0.024	0.017
0.8	1.147	0.244	0.097	0.052	0.032	0.021

Table K2-2. Geometry functions for a finite surface crack in a plate — intersection of crack with free surface ($10 \le l/a \le \infty$).

$l/a = 10$						
a/t	f_0^B	f_1^B	f_2^B	f_3^B	f_4^B	f_5^B
0	0.516	0.069	0.017	0.009	0.005	0.004
0.2	0.554	0.076	0.022	0.011	0.007	0.005
0.4	0.655	0.099	0.039	0.019	0.012	0.008
0.6	0.840	0.157	0.063	0.032	0.020	0.013
0.8	1.143	0.243	0.099	0.055	0.034	0.023
$l/a = 32$						
a/t	f_0^B	f_1^B	f_2^B	f_3^B	f_4^B	f_5^B
.05	0.203	0.010	0.004	0.007	0.000	0.000
.2	0.215	0.015	0.010	0.009	0.000	0.000
.4	0.273	0.021	0.016	0.010	0.000	0.000
.6	0.435	0.061	0.031	0.013	0.000	0.000
.8	0.735	0.142	0.065	0.032	0.011	0.000
$l/a = 60$						
a/t	f_0^B	f_1^B	f_2^B	f_3^B	f_4^B	f_5^B
.05	0.121	0.017	0.005	0.001	0.000	0.000
.2	0.163	0.032	0.011	0.005	0.000	0.000
.4	0.214	0.007	0.015	0.010	0.000	0.000
.6	0.355	0.089	0.020	0.015	0.000	0.000
.8	0.642	0.113	0.050	0.021	0.003	0.000
$l/a \to \infty$						
a/t	f_0^B	f_1^B	f_2^B	f_3^B	f_4^B	f_5^B
0	0.000	0.000	0.000	0.000	0.000	0.000
0.2	0.000	0.000	0.000	0.000	0.000	0.000
0.4	0.000	0.000	0.000	0.000	0.000	0.000
0.6	0.000	0.000	0.000	0.000	0.000	0.000
0.8	0.000	0.000	0.000	0.000	0.000	0.000

K1.2 Infinite surface crack

K_I is given by

$$K_I = \frac{1}{\sqrt{2\pi a}} \int_0^a \sigma(u) \sum_{i=1}^{5} f_i(a/t) \left(1 - \frac{u}{a}\right)^{i-\frac{3}{2}} du \quad . \tag{K3}$$

The stress state $\sigma = \sigma(u)$ is to be taken normal to the prospective crack plane in an uncracked plate. The coordinate *u* is defined in Fig. G1.2.

f_i (i = 1 to 5) are geometry functions which are given in Table K3 for the deepest point of the crack (f_i^A). See Fig. G1.2.

Remark: The plate should be large in the transverse direction to the crack so that edge effects do not influence the results.

Ref.: [K3].

Table K3. Geometry functions for an infinite surface crack in a plate.

a/t	f_1^A	f_2^A	f_3^A	f_4^A	f_5^A
0	2.000	0.977	1.142	-0.350	-0.091
0.1	2.000	1.419	1.138	-0.355	-0.076
0.2	2.000	2.537	1.238	-0.347	-0.056
0.3	2.000	4.238	1.680	-0.410	-0.019
0.4	2.000	6.636	2.805	-0.611	0.039
0.5	2.000	10.02	5.500	-1.340	0.218
0.6	2.000	15.04	11.88	-3.607	0.786
0.7	2.000	23.18	28.03	-10.50	2.587
0.8	2.000	38.81	78.75	-36.60	9.871
0.9	2.000	82.70	351.0	-207.1	60.86

K1.3 Embedded crack

K_I is given by

$$K_I = \sqrt{\pi a}\left[\sigma_m f_m\left(2a/t, l/2a, e/t\right) + \sigma_b f_b\left(2a/t, l/2a, e/t\right)\right] \quad . \tag{K4}$$

σ_m and σ_b are the membrane and bending stress components respectively, which define the stress state σ according to

$$\sigma = \sigma(u) = \sigma_m + \sigma_b\left(1 - \frac{2u}{t}\right) \qquad \text{for } 0 \le u \le t \quad . \tag{K5}$$

σ is to be taken normal to the prospective crack plane in an uncracked plate. σ_m and σ_b are determined by fitting σ to Eq. (K5). The coordinate *u* is defined in Fig. G1.3.

f_m and f_b are geometry functions which are given in Tables K4 and K5 for the points of the crack closest to (f^A), and furthest (f^B) from $u = 0$, respectively. See Fig. G1.3.

Remark: The plate should be large in comparison to the length of the crack so that edge effects do not influence the results.

Ref.: [K4].

Table K4. Geometry functions for an embedded crack in a plate — point closest to $u = 0$.

$l/2a = 1$						
$2a/t$	$e/t = 0$		$e/t = 0.15$		$e/t = 0.3$	
	f_m^A	f_b^A	f_m^A	f_b^A	f_m^A	f_b^A
0	0.638	0.000	0.638	0.191	0.638	0.383
0.2	0.649	0.087	0.659	0.286	0.694	0.509
0.4	0.681	0.182	0.725	0.411	-	-
0.6	0.739	0.296	0.870	0.609	-	-
$l/2a = 2$						
$2a/t$	$e/t = 0$		$e/t = 0.15$		$e/t = 0.3$	
	f_m^A	f_b^A	f_m^A	f_b^A	f_m^A	f_b^A
0	0.824	0.000	0.824	0.247	0.824	0.494
0.2	0.844	0.098	0.862	0.359	0.932	0.668
0.4	0.901	0.210	0.987	0.526	-	-
0.6	1.014	0.355	1.332	0.866	-	-
$l/2a = 4$						
$2a/t$	$e/t = 0$		$e/t = 0.15$		$e/t = 0.3$	
	f_m^A	f_b^A	f_m^A	f_b^A	f_m^A	f_b^A
0	0.917	0.000	0.917	0.275	0.917	0.550
0.2	0.942	0.102	0.966	0.394	1.058	0.749
0.4	1.016	0.220	1.129	0.584	-	-
0.6	1.166	0.379	1.655	1.034	-	-
$l/2a \to \infty$						
$2a/t$	$e/t = 0$		$e/t = 0.15$		$e/t = 0.3$	
	f_m^A	f_b^A	f_m^A	f_b^A	f_m^A	f_b^A
0	1.010	0.000	1.010	0.303	1.010	0.606
0.2	1.041	0.104	1.071	0.428	1.189	0.833
0.4	1.133	0.227	1.282	0.641	-	-
0.6	1.329	0.399	2.093	1.256	-	-

Table K5. Geometry functions for an embedded crack in a plate — point furthest from $u = 0$.

$l/2a = 1$						
$2a/t$	$e/t = 0$		$e/t = 0.15$		$e/t = 0.3$	
	f_m^B	f_b^B	f_m^B	f_b^B	f_m^B	f_b^B
0	0.638	0.000	0.638	0.191	0.638	0.383
0.2	0.649	-0.087	0.646	0.108	0.648	0.303
0.4	0.681	-0.182	0.668	0.022	-	-
0.6	0.739	-0.296	0.705	-0.071	-	-
$l/2a = 2$						
$2a/t$	$e/t = 0$		$e/t = 0.15$		$e/t = 0.3$	
	f_m^B	f_b^B	f_m^B	f_b^B	f_m^B	f_b^B
0	0.824	0.000	0.824	0.247	0.824	0.494
0.2	0.844	-0.098	0.844	0.155	0.866	0.418
0.4	0.901	-0.210	0.902	0.060	-	-
0.6	1.014	-0.355	1.016	-0.051	-	-
$l/2a = 4$						
$2a/t$	$e/t = 0$		$e/t = 0.15$		$e/t = 0.3$	
	f_m^B	f_b^B	f_m^B	f_b^B	f_m^B	f_b^B
0	0.917	0.000	0.917	0.275	0.917	0.550
0.2	0.942	-0.102	0.945	0.181	0.980	0.482
0.4	1.016	-0.220	1.029	0.086	-	-
0.6	1.166	-0.379	1.206	-0.030	-	-
$l/2a \to \infty$						
$2a/t$	$e/t = 0$		$e/t = 0.15$		$e/t = 0.3$	
	f_m^B	f_b^B	f_m^B	f_b^B	f_m^B	f_b^B
0	1.010	0.000	1.010	0.303	1.010	0.606
0.2	1.041	-0.104	1.048	0.210	1.099	0.550
0.4	1.133	-0.227	1.162	0.166	-	-
0.6	1.329	-0.399	1.429	0.000	-	-

K1.4 Through-thickness crack

K_I is given by

$$K_I = \sqrt{\pi l / 2}\left(\sigma_m f_m + \sigma_b f_b\right) \quad . \tag{K6}$$

σ_m and σ_b are the membrane and bending stress components respectively, which define the stress state σ according to

$$\sigma = \sigma(u) = \sigma_m + \sigma_b\left(1 - \frac{2u}{t}\right) \qquad \text{for } 0 \le u \le t \quad . \tag{K7}$$

σ is to be taken normal to the prospective crack plane in an uncracked plate. σ_m and σ_b are determined by fitting σ to Eq. (K7). The coordinate *u* is defined in Fig. G1.4.

f_m and f_b are geometry functions which are given in Table K6 for the intersections of the crack with the free surface at $u = 0$ (f^A), and at $u = t$ (f^B). See Fig. G1.4.

Remark: The plate should be large in comparison to the length of the crack so that edge effects do not influence the results.

Ref.: [K5].

Table K6. Geometry functions for a through-thickness crack in a plate.

f_m^A	f_b^A	f_m^B	f_b^B
1.000	1.000	1.000	-1.000

K2. Axial cracks in a cylinder

K2.1 Finite internal surface crack

K_I is given by

$$K_I = \sqrt{\pi a}\sum_{j=0}^{3}\sigma_j f_j\left(a/t, l/a, R_i/t\right) \quad . \tag{K8}$$

σ_j (j = 0 to 3) are stress components which define the stress state σ according to

$$\sigma = \sigma(u) = \sum_{j=0}^{3}\sigma_j\left(\frac{u}{a}\right)^j \qquad \text{for } 0 \le u \le a \quad . \tag{K9}$$

σ is to be taken normal to the prospective crack plane in an uncracked cylinder. σ_j is determined by fitting σ to Eq. (K9). The coordinate u is defined in Fig. G2.1.

f_j (j = 0 to 3) are geometry functions which are given in Tables K7 and K8 for the deepest point of the crack (f^A), and at the intersection of the crack with the free surface (f^B), respectively. See Fig. G2.1.

Remarks: The cylinder should be long in comparison to the length of the crack so that edge effects do not influence the results.

Ref.: [K1] and [K6].

Table K7. Geometry functions for a finite axial internal surface crack in a cylinder — deepest point of crack.

a/t	$l/a=2,\quad R_i/t=4$				$l/a=2,\quad R_i/t=10$			
	f_0^A	f_1^A	f_2^A	f_3^A	f_0^A	f_1^A	f_2^A	f_3^A
0	0.659	0.471	0.387	0.337	0.659	0.471	0.387	0.337
0.2	0.643	0.454	0.375	0.326	0.647	0.456	0.375	0.326
0.5	0.663	0.463	0.378	0.328	0.669	0.464	0.380	0.328
0.8	0.704	0.489	0.397	0.342	0.694	0.484	0.394	0.339
a/t	$l/a=5,\quad R_i/t=4$				$l/a=5,\quad R_i/t=10$			
	f_0^A	f_1^A	f_2^A	f_3^A	f_0^A	f_1^A	f_2^A	f_3^A
0	0.939	0.580	0.434	0.353	0.939	0.580	0.434	0.353
0.2	0.919	0.579	0.452	0.382	0.932	0.584	0.455	0.383
0.5	1.037	0.622	0.474	0.395	1.058	0.629	0.477	0.397
0.8	1.255	0.720	0.534	0.443	1.211	0.701	0.523	0.429
a/t	$l/a=10,\quad R_i/t=4$				$l/a=10,\quad R_i/t=10$			
	f_0^A	f_1^A	f_2^A	f_3^A	f_0^A	f_1^A	f_2^A	f_3^A
0	1.053	0.606	0.443	0.357	1.053	0.606	0.443	0.357
0.2	1.045	0.634	0.487	0.406	1.062	0.641	0.489	0.417
0.5	1.338	0.739	0.540	0.438	1.359	0.746	0.544	0.440
0.8	1.865	0.948	0.659	0.516	1.783	0.914	0.639	0.504

Table K8. Geometry functions for a finite axial internal surface crack in a cylinder — intersection of crack with free surface.

a/t	$l/a=2,\quad R_i/t=4$				$l/a=2,\quad R_i/t=10$			
	f_0^B	f_1^B	f_2^B	f_3^B	f_0^B	f_1^B	f_2^B	f_3^B
0	0.716	0.118	0.041	0.022	0.716	0.118	0.041	0.022
0.2	0.719	0.124	0.046	0.024	0.726	0.126	0.047	0.024
0.5	0.759	0.136	0.052	0.027	0.777	0.141	0.054	0.028
0.8	0.867	0.158	0.062	0.032	0.859	0.163	0.063	0.033
a/t	$l/a=5,\quad R_i/t=4$				$l/a=5,\quad R_i/t=10$			
	f_0^B	f_1^B	f_2^B	f_3^B	f_0^B	f_1^B	f_2^B	f_3^B
0	0.673	0.104	0.032	0.016	0.673	0.104	0.032	0.015
0.2	0.670	0.107	0.037	0.018	0.676	0.109	0.037	0.018
0.5	0.803	0.151	0.059	0.031	0.814	0.153	0.060	0.031
0.8	1.060	0.229	0.095	0.051	1.060	0.225	0.092	0.049
a/t	$l/a=10,\quad R_i/t=4$				$l/a=10,\quad R_i/t=10$			
	f_0^B	f_1^B	f_2^B	f_3^B	f_0^B	f_1^B	f_2^B	f_3^B
0	0.516	0.069	0.017	0.009	0.516	0.069	0.017	0.009
0.2	0.577	0.075	0.022	0.010	0.578	0.075	0.022	0.010
0.5	0.759	0.134	0.051	0.027	0.753	0.131	0.050	0.026
0.8	1.144	0.250	0.103	0.056	1.123	0.241	0.099	0.053

K2.2 Infinite internal surface crack

K_I is given by

$$K_I = \frac{1}{\sqrt{2\pi a}} \int_0^a \sigma(u) \sum_{j=1}^{3} f_j\left(a/t, R_i/t\right) \left(1 - \frac{u}{a}\right)^{j-\frac{3}{2}} du \quad . \qquad \text{(K10)}$$

The stress state $\sigma = \sigma(u)$ is to be taken normal to the prospective crack plane in an uncracked cylinder. The coordinate *u* is defined in Fig. G2.2.

f_j (*j* = 1 to 3) are geometry functions which are given in Table K9 for the deepest point of the crack (f^A). See Fig. G2.2.

Ref.: [K3].

Table K9. Geometry functions for an infinite axial internal surface crack in a cylinder.

a/t	$R_i/t=0.5$			$R_i/t=1$		
	f_1^A	f_2^A	f_3^A	f_1^A	f_2^A	f_3^A
0	2.000	1.328	0.220	2.000	1.336	0.220
0.1	2.000	0.890	0.155	2.000	1.271	0.184
0.2	2.000	0.895	0.193	2.000	1.566	0.237
0.3	2.000	1.032	0.252	2.000	1.997	0.360
0.4	2.000	1.329	0.210	2.000	2.501	0.542
0.5	2.000	1.796	0.093	2.000	3.072	0.762
0.6	2.000	2.457	-0.074	2.000	3.807	0.892
0.7	2.000	3.597	-0.618	2.000	4.877	0.825
0.75	2.000	4.571	-1.272	2.000	5.552	0.786
a/t	$R_i/t=2$			$R_i/t=4$		
	f_1^A	f_2^A	f_3^A	f_1^A	f_2^A	f_3^A
0	2.000	1.340	0.219	2.000	1.340	0.219
0.1	2.000	1.519	0.212	2.000	1.659	0.217
0.2	2.000	2.119	0.322	2.000	2.475	0.358
0.3	2.000	2.934	0.551	2.000	3.615	0.709
0.4	2.000	3.820	1.066	2.000	4.982	1.499
0.5	2.000	4.692	1.853	2.000	6.455	2.936
0.6	2.000	5.697	2.600	2.000	7.977	5.018
0.7	2.000	6.995	3.224	2.000	9.513	7.637
0.75	2.000	7.656	3.733	2.000	10.24	9.134

K2.3 Finite external surface crack

K_I is given by

$$K_I = \sqrt{\pi a}\sum_{j=0}^{3}\sigma_j f_j\left(a/t, l/a, R_i/t\right) \quad . \tag{K11}$$

σ_j (j = 0 to 3) are stress components which define the stress state σ according to

$$\sigma = \sigma(u) = \sum_{j=0}^{3}\sigma_j\left(\frac{u}{a}\right)^j \qquad \text{for } 0 \le u \le a \quad . \tag{K12}$$

σ is to be taken normal to the prospective crack plane in an uncracked cylinder. σ_j is determined by fitting σ to Eq. (K12). The coordinate u is defined in Fig. G2.3.

f_j (j = 0 to 3) are geometry functions which are given in Tables K10 and K11 for the deepest point of the crack (f^A), and at the intersection of the crack with the free surface (f^B), respectively. See Fig. G2.3.

Remarks: The cylinder should be long in comparison to the length of the crack so that edge effects do not influence the results.

Ref.: [K1] and [K6].

Table K10. Geometry functions for a finite axial external surface crack in a cylinder — deepest point of crack.

a/t	$l/a=2,\quad R_i/t=4$				$l/a=2,\quad R_i/t=10$			
	f_0^A	f_1^A	f_2^A	f_3^A	f_0^A	f_1^A	f_2^A	f_3^A
0	0.659	0.471	0.387	0.337	0.659	0.471	0.387	0.337
0.2	0.656	0.459	0.377	0.327	0.653	0.457	0.376	0.327
0.5	0.697	0.473	0.384	0.331	0.687	0.470	0.382	0.330
0.8	0.736	0.495	0.398	0.342	0.712	0.487	0.394	0.340
a/t	$l/a=5,\quad R_i/t=4$				$l/a=5,\quad R_i/t=10$			
	f_0^A	f_1^A	f_2^A	f_3^A	f_0^A	f_1^A	f_2^A	f_3^A
0	0.939	0.580	0.434	0.353	0.939	0.580	0.434	0.353
0.2	0.964	0.596	0.461	0.387	0.953	0.591	0.459	0.386
0.5	1.183	0.672	0.500	0.410	1.139	0.656	0.491	0.405
0.8	1.502	0.795	0.568	0.455	1.361	0.746	0.543	0.439
a/t	$l/a=10,\quad R_i/t=4$				$l/a=10,\quad R_i/t=10$			
	f_0^A	f_1^A	f_2^A	f_3^A	f_0^A	f_1^A	f_2^A	f_3^A
0	1.053	0.606	0.443	0.357	1.053	0.606	0.443	0.357
0.2	1.107	0.658	0.499	0.413	1.092	0.652	0.496	0.411
0.5	1.562	0.820	0.584	0.465	1.508	0.799	0.571	0.457
0.8	2.390	1.122	0.745	0.568	2.188	1.047	0.704	0.541

Table K11. Geometry functions for a finite axial external surface crack in a cylinder — intersection of crack with free surface.

a/t	$l/a=2,\quad R_i/t=4$				$l/a=2,\quad R_i/t=10$			
	f_0^B	f_1^B	f_2^B	f_3^B	f_0^B	f_1^B	f_2^B	f_3^B
0	0.716	0.118	0.041	0.022	0.716	0.118	0.041	0.022
0.2	0.741	0.130	0.049	0.026	0.736	0.129	0.048	0.025
0.5	0.819	0.155	0.061	0.033	0.807	0.150	0.059	0.031
0.8	0.954	0.192	0.078	0.041	0.926	0.182	0.072	0.038
a/t	$l/a=5,\quad R_i/t=4$				$l/a=5,\quad R_i/t=10$			
	f_0^B	f_1^B	f_2^B	f_3^B	f_0^B	f_1^B	f_2^B	f_3^B
0	0.673	0.104	0.032	0.015	0.673	0.104	0.032	0.015
0.2	0.690	0.113	0.039	0.019	0.685	0.111	0.039	0.019
0.5	0.864	0.170	0.068	0.036	0.856	0.167	0.066	0.035
0.8	1.217	0.277	0.117	0.064	1.198	0.269	0.112	0.061
a/t	$l/a=10,\quad R_i/t=4$				$l/a=10,\quad R_i/t=10$			
	f_0^B	f_1^B	f_2^B	f_3^B	f_0^B	f_1^B	f_2^B	f_3^B
0	0.516	0.069	0.017	0.009	0.516	0.069	0.017	0.009
0.2	0.583	0.076	0.022	0.010	0.583	0.076	0.022	0.010
0.5	0.748	0.128	0.047	0.024	0.768	0.135	0.051	0.027
0.8	1.105	0.230	0.092	0.049	1.202	0.264	0.109	0.059

K2.4 Infinite external surface crack

K_I is given by

$$K_I = \frac{1}{\sqrt{2\pi a}} \int_0^a \sigma(u) \sum_{j=1}^{4} f_j\left(a/t, R_i/t\right) \left(1 - \frac{u}{a}\right)^{j-\frac{3}{2}} du \quad . \qquad \text{(K13)}$$

The stress state $\sigma = \sigma(u)$ is to be taken normal to the prospective crack plane in an uncracked cylinder. The coordinate *u* is defined in Fig. G2.4.

f_j (j = 1 to 4) are geometry functions which are given in Table K12 for the deepest point of the crack (f^A). See Fig. G2.4.

Ref.: [K3].

Table K12. Geometry functions for an infinite axial external surface crack in a cylinder.

a/t	$R_i/t=0.5$				$R_i/t=1$			
	f_1^A	f_2^A	f_3^A	f_4^A	f_1^A	f_2^A	f_3^A	f_4^A
0	2.000	0.901	1.401	-0.620	2.000	0.901	1.401	-0.620
0.1	2.000	1.359	1.376	-0.585	2.000	1.331	1.365	-0.584
0.2	2.000	1.933	1.387	-0.549	2.000	1.967	1.369	-0.543
0.3	2.000	2.614	1.422	-0.510	2.000	2.766	1.484	-0.512
0.4	2.000	3.408	1.541	-0.481	2.000	3.708	1.759	-0.505
0.5	2.000	4.321	1.799	-0.472	2.000	4.787	2.238	-0.528
0.6	2.000	5.459	2.101	-0.456	2.000	6.055	2.904	-0.577
0.7	2.000	7.145	2.187	-0.361	2.000	7.726	3.601	-0.605
0.75	2.000	8.355	2.112	-0.265	2.000	8.853	3.901	-0.590
a/t	$R_i/t=2$				$R_i/t=4$			
	f_1^A	f_2^A	f_3^A	f_4^A	f_1^A	f_2^A	f_3^A	f_4^A
0	2.000	0.901	1.401	-0.620	2.000	0.900	1.400	-0.620
0.1	2.000	1.330	1.370	-0.585	2.000	1.335	1.382	-0.587
0.2	2.000	2.086	1.403	-0.542	2.000	2.219	1.416	-0.535
0.3	2.000	3.095	1.580	-0.510	2.000	3.464	1.658	-0.501
0.4	2.000	4.307	2.054	-0.524	2.000	4.993	2.412	-0.549
0.5	2.000	5.643	3.004	-0.625	2.000	6.823	3.794	-0.704
0.6	2.000	7.103	4.376	-0.802	2.000	8.984	6.051	-1.011
0.7	2.000	8.976	5.735	-0.949	2.000	11.10	10.07	-1.674
0.75	2.000	10.28	6.243	-0.963	2.000	11.80	13.08	-2.229

K2.5 Through-thickness crack

K_I is given by

$$K_I = \sqrt{\pi l/2}\left(\sum_{j=0}^{4}\sigma_j f_j(l/t, R_i/t)\right) \quad , \tag{K14}$$

where σ_j (j = 0 to 4) are stress components which define the stress state σ according to

$$\sigma = \sigma(u) = \sum_{j=0}^{4}\sigma_j\left(\frac{u}{t}\right)^j \qquad \text{for } 0 \le u \le t \quad . \tag{K15}$$

σ is to be taken normal to the prospective crack plane in an uncracked cylinder. σ_j is determined by fitting σ to Eq. (K15). The coordinate u is defined in Fig. G2.5.

f_j (j = 0 to 4) are geometry functions which are given in Tables K13 and K14 for the intersections of the crack with the free surface at $u = 0$ (f^A), and at $u = t$ (f^B). See Fig. G2.5.

Remarks: The cylinder should be long in comparison to the length of the crack so that edge effects do not influence. The small negative values given in Table K13-1 to K13-3 are the result of the fitting procedure in [K7].

Ref.: [K7].

Table K13-1. Geometry functions for an axial through-thickness crack in a cylinder — the intersection of the crack with the free surface at $u = 0$.

$R_i / t = 5$					
l/t	f_0^A	f_1^A	f_2^A	f_3^A	f_4^A
1	1.003	0.099	0.004	-0.022	-0.022
2	1.017	0.155	0.036	-0.001	-0.016
4	1.233	0.316	0.146	0.082	0.051
6	1.569	0.520	0.288	0.190	0.139
8	1.966	0.747	0.445	0.311	0.236
10	2.396	0.987	0.610	0.437	0.338
15	3.538	1.605	1.033	0.759	0.599
20	4.700	2.221	1.454	1.079	0.857
25	5.826	2.812	1.856	1.384	1.103
30	6.873	3.360	2.227	1.665	1.330
50	9.656	4.812	3.213	2.412	1.931
$R_i / t = 10$					
l/t	f_0^A	f_1^A	f_2^A	f_3^A	f_4^A
1	1.017	0.095	-0.001	-0.028	-0.038
2	0.999	0.132	0.016	-0.019	-0.033
4	1.097	0.225	0.077	0.026	0.005
6	1.284	0.347	0.161	0.091	0.057
8	1.525	0.491	0.261	0.168	0.119
10	1.801	0.649	0.370	0.251	0.187
15	2.578	1.076	0.665	0.476	0.368
20	3.421	1.528	0.973	0.710	0.558
25	4.294	1.988	1.286	0.948	0.749
30	5.175	2.448	1.599	1.185	0.940
50	8.584	4.209	2.788	2.083	1.663

Table K13-2. Geometry functions for an axial through-thickness crack in a cylinder — the intersection of the crack with the free surface at $u = 0$.

$R_i / t = 20$					
l/t	f_0^A	f_1^A	f_2^A	f_3^A	f_4^A
1	1.025	0.094	-0.003	-0.029	-0.038
2	0.997	0.121	0.006	-0.041	-0.037
4	1.029	0.175	0.038	-0.005	-0.022
6	1.120	0.244	0.085	0.031	0.007
8	1.251	0.328	0.144	0.076	0.043
10	1.412	0.424	0.211	0.127	0.085
15	1.895	0.699	0.401	0.272	0.203
20	2.448	1.001	0.609	0.431	0.331
25	3.040	1.319	0.826	0.596	0.465
30	3.656	1.645	1.048	0.765	0.601
50	6.203	2.971	1.947	1.445	1.148
$R_i / t = 50$					
l/t	f_0^A	f_1^A	f_2^A	f_3^A	f_4^A
1	1.020	0.093	-0.003	-0.029	-0.037
2	0.999	0.116	0.001	-0.035	-0.047
4	0.997	0.147	0.016	-0.024	-0.038
6	1.023	0.179	0.036	-0.009	-0.027
8	1.071	0.217	0.063	0.011	-0.010
10	1.138	0.262	0.094	0.036	0.010
15	1.366	0.401	0.191	0.110	0.070
20	1.652	0.565	0.305	0.197	0.141
25	1.975	0.744	0.429	0.292	0.218
30	2.323	0.934	0.559	0.392	0.298
50	3.852	1.746	1.114	0.813	0.639

Table K13-3. Geometry functions for an axial through-thickness crack in a cylinder — the intersection of the crack with the free surface at $u = 0$.

$R_i / t = 100$					
l/t	f_0^A	f_1^A	f_2^A	f_3^A	f_4^A
1	0.989	0.089	-0.002	-0.026	-0.034
2	0.990	0.114	0.000	-0.034	-0.045
4	0.990	0.140	0.009	-0.030	-0.037
6	0.995	0.158	0.020	-0.022	-0.039
8	1.013	0.178	0.034	-0.012	-0.041
10	1.042	0.202	0.050	0.001	-0.019
15	1.156	0.278	0.103	0.041	0.014
20	1.313	0.373	0.170	0.092	0.055
25	1.501	0.482	0.245	0.151	0.103
30	1.711	0.600	0.328	0.214	0.154
50	2.681	1.129	0.692	0.492	0.380

Table K14-1. Geometry functions for an axial through-thickness crack in a cylinder — the intersection of the crack with the free surface at $u = t$.

$R_i / t = 5$					
l/t	f_0^B	f_1^B	f_2^B	f_3^B	f_4^B
1	1.159	1.022	0.911	0.835	0.783
2	1.276	1.043	0.890	0.790	0.720
4	1.595	1.168	0.945	0.808	0.716
6	1.919	1.309	1.024	0.856	0.746
8	2.211	1.439	1.100	0.906	0.780
10	2.464	1.551	1.167	0.951	0.812
15	2.938	1.758	1.290	1.033	0.870
20	3.251	1.890	1.367	1.084	0.907
25	3.479	1.984	1.421	1.120	0.932
30	3.670	2.063	1.467	1.151	0.954
50	4.272	2.327	1.627	1.262	1.036
$R_i / t = 10$					
l/t	f_0^B	f_1^B	f_2^B	f_3^B	f_4^B
1	1.111	0.994	0.891	0.818	0.766
2	1.176	0.992	0.854	0.763	0.697
4	1.397	1.075	0.884	0.764	0.682
6	1.649	1.185	0.945	0.799	0.701
8	1.900	1.299	1.012	0.843	0.731
10	2.138	1.408	1.078	0.888	0.763
15	2.647	1.641	1.222	0.987	0.836
20	3.035	1.817	1.330	1.063	0.893
25	3.323	1.945	1.408	1.117	0.933
30	3.530	2.034	1.462	1.153	0.959
50	3.848	2.149	1.519	1.186	0.979

Table K14-2. Geometry functions for an axial through-thickness crack in a cylinder — the intersection of the crack with the free surface at $u = t$.

$R_i / t = 20$					
l/t	f_0^B	f_1^B	f_2^B	f_3^B	f_4^B
1	1.080	0.976	0.877	0.807	0.757
2	1.110	0.957	0.830	0.740	0.683
4	1.250	1.002	0.836	0.728	0.653
6	1.425	1.077	0.874	0.747	0.660
8	1.612	1.162	0.923	0.777	0.679
10	1.801	1.250	0.976	0.813	0.704
15	2.249	1.459	1.106	0.903	0.770
20	2.637	1.640	1.219	0.983	0.830
25	2.963	1.791	1.314	1.050	0.881
30	3.231	1.914	1.391	1.104	0.922
50	3.872	2.198	1.565	1.226	1.013
$R_i / t = 50$					
l/t	f_0^B	f_1^B	f_2^B	f_3^B	f_4^B
1	1.045	0.951	0.858	0.792	0.744
2	1.057	0.927	0.810	0.727	0.669
4	1.128	0.940	0.794	0.696	0.627
6	1.224	0.977	0.808	0.697	0.619
8	1.335	1.026	0.833	0.710	0.625
10	1.453	1.080	0.864	0.729	0.638
15	1.762	1.224	0.952	0.789	0.680
20	2.066	1.368	1.043	0.852	0.727
25	2.350	1.502	1.128	0.913	0.773
30	2.608	1.624	1.205	0.968	0.815
50	3.392	1.990	1.437	1.135	0.943

Table K14-3. Geometry functions for an axial through-thickness crack in a cylinder — the intersection of the crack with the free surface at $u = t$.

$R_i / t = 100$					
l/t	f_0^B	f_1^B	f_2^B	f_3^B	f_4^B
1	1.003	0.916	0.830	0.768	0.724
2	1.024	0.905	0.792	0.713	0.658
4	1.073	0.910	0.773	0.679	0.615
6	1.131	0.928	0.774	0.671	0.598
8	1.200	0.956	0.786	0.674	0.593
10	1.276	0.990	0.804	0.684	0.601
15	1.486	1.088	0.862	0.721	0.625
20	1.706	1.192	0.927	0.766	0.658
25	1.925	1.297	0.993	0.812	0.693
30	2.137	1.397	1.057	0.858	0.728
50	2.855	1.736	1.272	1.013	0.847

K3. Circumferential cracks in a cylinder

K3.1 Part circumferential internal surface crack

K_I is given by

$$K_I = \sqrt{\pi a}\left(\sum_{j=0}^{3}\sigma_j f_j\left(a/t, l/a, R_i/t\right) + \sigma_{bg} f_{bg}\left(a/t, l/a, R_i/t\right)\right) \quad . \tag{K16}$$

where σ_j (j = 0 to 3) are stress components which define the stress state σ according to

$$\sigma = \sigma(u) = \sum_{j=0}^{3}\sigma_j\left(\frac{u}{a}\right)^j \qquad \text{for } 0 \le u \le a \quad , \tag{K17}$$

and σ_{bg} is the global bending stress. σ and σ_{bg} are to be taken normal to the prospective crack plane in an uncracked cylinder. σ_j is determined by fitting σ to Eq. (K17). The coordinate u is defined in Fig. G3.1.

f_j (j = 0 to 3) and f_{bg} are geometry functions which are given in Tables K15 and K16 for the deepest point of the crack (f^A), and at the intersection of the crack with the free surface (f^B), respectively. See Fig. G3.1.

Remark: The cylinder should be long in the transverse direction to the crack so that edge effects do not influence.

Ref.: [K2].

Table K15-1. Geometry functions for a part circumferential internal surface crack in a cylinder — deepest point of crack ($l/a = 2$).

a/t	f_0^A	f_1^A	f_2^A	f_3^A	f_{bg}^A	f_0^A	f_1^A	f_2^A	f_3^A	f_{bg}^A
	$l/a = 2,\quad R_i/t = 1$					$l/a = 2,\quad R_i/t = 2$				
0	0.657	0.465	0.385	0.338	0.329	0.657	0.465	0.385	0.338	0.438
0.1	0.661	0.468	0.387	0.339	0.355	0.659	0.466	0.385	0.337	0.456
0.2	0.667	0.473	0.391	0.342	0.381	0.664	0.469	0.387	0.339	0.475
0.4	0.685	0.485	0.399	0.348	0.385	0.681	0.478	0.393	0.343	0.517
0.6	0.723	0.505	0.413	0.359	0.484	0.707	0.492	0.403	0.350	0.567
0.8	0.831	0.565	0.453	0.388	0.602	0.769	0.530	0.430	0.371	0.651
	$l/a = 2,\quad R_i/t = 5$					$l/a = 2,\quad R_i/t = 10$				
0	0.657	0.465	0.385	0.338	0.548	0.657	0.465	0.385	0.338	0.597
0.1	0.658	0.464	0.383	0.336	0.556	0.657	0.464	0.383	0.335	0.602
0.2	0.662	0.466	0.385	0.337	0.567	0.661	0.465	0.384	0.336	0.610
0.4	0.677	0.472	0.388	0.339	0.596	0.676	0.470	0.387	0.337	0.632
0.6	0.697	0.482	0.395	0.344	0.627	0.693	0.479	0.392	0.341	0.656
0.8	0.727	0.507	0.413	0.358	0.671	0.712	0.498	0.407	0.353	0.683
	$l/a = 2,\quad R_i/t = 20$					$l/a = 2,\quad R_i/t = 40$				
0	0.657	0.465	0.385	0.338	0.626	0.657	0.465	0.385	0.338	0.641
0.1	0.657	0.463	0.383	0.335	0.628	0.657	0.463	0.383	0.335	0.642
0.2	0.661	0.465	0.383	0.335	0.634	0.660	0.464	0.383	0.335	0.647
0.4	0.675	0.469	0.386	0.336	0.652	0.675	0.469	0.385	0.336	0.663
0.6	0.691	0.477	0.390	0.340	0.672	0.690	0.476	0.390	0.339	0.680
0.8	0.703	0.493	0.403	0.350	0.689	0.699	0.490	0.402	0.349	0.692
	$l/a = 2,\quad R_i/t = 80$					$l/a = 2,\quad R_i/t \to \infty$				
0	0.657	0.465	0.385	0.338	0.649	0.657	0.465	0.385	0.338	0.657
0.1	0.657	0.463	0.382	0.335	0.649	0.657	0.463	0.382	0.335	0.657
0.2	0.660	0.464	0.383	0.335	0.653	0.660	0.464	0.383	0.335	0.660
0.4	0.674	0.468	0.385	0.336	0.668	0.675	0.469	0.385	0.336	0.675
0.6	0.688	0.475	0.389	0.339	0.683	0.691	0.475	0.389	0.339	0.691
0.8	0.696	0.488	0.400	0.348	0.692	0.697	0.489	0.400	0.348	0.697

Table K15-2. Geometry functions for a part circumferential internal surface crack in a cylinder — deepest point of crack ($l/a = 4$).

a/t	$l/a=4,\ R_i/t=1$					$l/a=4,\ R_i/t=2$				
	f_0^A	f_1^A	f_2^A	f_3^A	f_{bg}^A	f_0^A	f_1^A	f_2^A	f_3^A	f_{bg}^A
0	0.883	0.569	0.451	0.386	0.442	0.883	0.569	0.451	0.386	0.589
0.1	0.863	0.562	0.447	0.382	0.461	0.874	0.565	0.448	0.382	0.602
0.2	0.855	0.561	0.447	0.382	0.483	0.874	0.566	0.449	0.383	0.621
0.4	0.866	0.567	0.451	0.385	0.538	0.900	0.576	0.454	0.387	0.674
0.6	0.932	0.599	0.471	0.400	0.628	0.956	0.601	0.470	0.398	0.753
0.8	1.166	0.715	0.545	0.452	0.803	1.102	0.677	0.519	0.434	0.896
a/t	$l/a=4,\ R_i/t=5$					$l/a=4,\ R_i/t=10$				
	f_0^A	f_1^A	f_2^A	f_3^A	f_{bg}^A	f_0^A	f_1^A	f_2^A	f_3^A	f_{bg}^A
0	0.883	0.569	0.451	0.386	0.736	0.883	0.569	0.451	0.386	0.803
0.1	0.880	0.566	0.448	0.382	0.743	0.882	0.567	0.448	0.382	0.807
0.2	0.888	0.569	0.450	0.384	0.759	0.893	0.571	0.450	0.384	0.822
0.4	0.930	0.584	0.457	0.388	0.814	0.943	0.588	0.459	0.388	0.878
0.6	0.988	0.607	0.471	0.397	0.882	1.005	0.611	0.472	0.397	0.946
0.8	1.069	0.656	0.505	0.422	0.972	1.061	0.650	0.500	0.419	1.010
a/t	$l/a=4,\ R_i/t=20$					$l/a=4,\ R_i/t=40$				
	f_0^A	f_1^A	f_2^A	f_3^A	f_{bg}^A	f_0^A	f_1^A	f_2^A	f_3^A	f_{bg}^A
0	0.883	0.569	0.451	0.386	0.841	0.883	0.569	0.451	0.386	0.861
0.1	0.883	0.567	0.448	0.382	0.844	0.884	0.567	0.448	0.382	0.864
0.2	0.895	0.571	0.451	0.384	0.858	0.896	0.572	0.451	0.384	0.878
0.4	0.951	0.590	0.459	0.389	0.917	0.954	0.591	0.460	0.389	0.937
0.6	1.016	0.614	0.473	0.398	0.985	1.022	0.615	0.473	0.398	1.006
0.8	1.059	0.648	0.498	0.417	1.033	1.059	0.646	0.497	0.416	1.046
a/t	$l/a=4,\ R_i/t=80$					$l/a=4,\ R_i/t\to\infty$				
	f_0^A	f_1^A	f_2^A	f_3^A	f_{bg}^A	f_0^A	f_1^A	f_2^A	f_3^A	f_{bg}^A
0	0.883	0.569	0.451	0.386	0.872	0.883	0.569	0.451	0.386	0.883
0.1	0.884	0.567	0.448	0.382	0.874	0.884	0.567	0.449	0.383	0.884
0.2	0.896	0.572	0.451	0.384	0.887	0.898	0.572	0.451	0.384	0.898
0.4	0.955	0.591	0.460	0.389	0.946	0.962	0.593	0.461	0.390	0.962
0.6	1.023	0.615	0.473	0.398	1.015	1.038	0.620	0.476	0.399	1.038
0.8	1.058	0.645	0.496	0.416	1.052	1.070	0.649	0.498	0.416	1.070

Table K15-3. Geometry functions for a part circumferential internal surface crack in a cylinder — deepest point of crack ($l/a = 8$).

a/t	$l/a=8,\ R_i/t=1$					$l/a=8,\ R_i/t=2$				
	f_0^A	f_1^A	f_2^A	f_3^A	f_{bg}^A	f_0^A	f_1^A	f_2^A	f_3^A	f_{bg}^A
0	1.022	0.632	0.491	0.415	0.511	1.022	0.632	0.491	0.415	0.681
0.1	0.982	0.617	0.482	0.407	0.523	1.004	0.624	0.485	0.409	0.691
0.2	0.966	0.612	0.479	0.406	0.566	1.008	0.626	0.486	0.410	0.712
0.4	0.992	0.624	0.486	0.410	0.593	1.062	0.646	0.497	0.416	0.784
0.6	1.106	0.676	0.518	0.432	0.678	1.179	0.695	0.525	0.436	0.892
0.8	1.549	0.904	0.669	0.545	0.892	1.484	0.837	0.613	0.498	1.125
a/t	$l/a=8,\ R_i/t=5$					$l/a=8,\ R_i/t=10$				
	f_0^A	f_1^A	f_2^A	f_3^A	f_{bg}^A	f_0^A	f_1^A	f_2^A	f_3^A	f_{bg}^A
0	1.022	0.632	0.491	0.415	0.852	1.022	0.632	0.491	0.415	0.929
0.1	1.018	0.629	0.487	0.411	0.859	1.022	0.630	0.488	0.411	0.935
0.2	1.039	0.636	0.491	0.413	0.885	1.051	0.640	0.493	0.414	0.966
0.4	1.139	0.671	0.509	0.424	0.989	1.176	0.684	0.515	0.427	1.094
0.6	1.274	0.723	0.538	0.442	1.124	1.333	0.740	0.546	0.447	1.248
0.8	1.479	0.821	0.600	0.487	1.314	1.487	0.819	0.597	0.484	1.402
a/t	$l/a=8,\ R_i/t=20$					$l/a=8,\ R_i/t=40$				
	f_0^A	f_1^A	f_2^A	f_3^A	f_{bg}^A	f_0^A	f_1^A	f_2^A	f_3^A	f_{bg}^A
0	1.022	0.632	0.491	0.415	0.973	1.022	0.632	0.491	0.415	0.997
0.1	1.025	0.631	0.489	0.411	0.979	1.026	0.632	0.489	0.411	1.003
0.2	1.057	0.643	0.494	0.415	1.013	1.061	0.644	0.495	0.415	1.038
0.4	1.200	0.691	0.519	0.429	1.156	1.212	0.695	0.521	0.430	1.190
0.6	1.376	0.754	0.552	0.450	1.332	1.403	0.762	0.556	0.453	1.380
0.8	1.505	0.821	0.597	0.483	1.464	1.523	0.826	0.598	0.484	1.501
a/t	$l/a=8,\ R_i/t=80$					$l/a=8,\ R_i/t\to\infty$				
	f_0^A	f_1^A	f_2^A	f_3^A	f_{bg}^A	f_0^A	f_1^A	f_2^A	f_3^A	f_{bg}^A
0	1.022	0.632	0.491	0.415	1.009	1.022	0.632	0.491	0.415	1.022
0.1	1.023	0.632	0.489	0.411	1.015	1.027	0.632	0.489	0.412	1.027
0.2	1.061	0.644	0.495	0.415	1.050	1.066	0.645	0.496	0.416	1.066
0.4	1.216	0.696	0.521	0.431	1.205	1.234	0.703	0.525	0.433	1.234
0.6	1.415	0.766	0.558	0.453	1.404	1.452	0.778	0.563	0.457	1.452
0.8	1.534	0.828	0.599	0.484	1.523	1.573	0.840	0.604	0.487	1.573

Table K15-4. Geometry functions for a part circumferential internal surface crack in a cylinder — deepest point of crack ($l/a = 16$).

a/t	$l/a=16,\quad R_i/t=1$					$l/a=16,\quad R_i/t=2$				
	f_0^A	f_1^A	f_2^A	f_3^A	f_{bg}^A	f_0^A	f_1^A	f_2^A	f_3^A	f_{bg}^A
0	1.088	0.664	0.512	0.431	0.544	1.088	0.664	0.512	0.431	0.725
0.1	1.035	0.643	0.499	0.420	0.581	1.064	0.653	0.504	0.424	0.731
0.2	1.021	0.638	0.497	0.419	0.562	1.077	0.658	0.507	0.425	0.758
0.4	1.079	0.672	0.520	0.438	0.594	1.163	0.692	0.525	0.436	0.840
0.6	1.200	0.730	0.557	0.464	0.675	1.353	0.771	0.572	0.468	0.966
0.8	1.549	0.904	0.669	0.545	0.892	1.829	1.003	0.721	0.577	1.247
a/t	$l/a=16,\quad R_i/t=5$					$l/a=16,\quad R_i/t=10$				
	f_0^A	f_1^A	f_2^A	f_3^A	f_{bg}^A	f_0^A	f_1^A	f_2^A	f_3^A	f_{bg}^A
0	1.088	0.664	0.512	0.431	0.907	1.088	0.664	0.512	0.431	0.989
0.1	1.083	0.660	0.508	0.426	0.912	1.090	0.663	0.509	0.427	0.996
0.2	1.126	0.676	0.516	0.431	0.958	1.146	0.683	0.520	0.433	1.054
0.4	1.291	0.736	0.547	0.450	1.112	1.361	0.760	0.560	0.458	1.258
0.6	1.522	0.824	0.596	0.482	1.323	1.640	0.861	0.615	0.493	1.522
0.8	1.921	0.996	0.699	0.552	1.653	1.984	1.008	0.701	0.552	1.844
a/t	$l/a=16,\quad R_i/t=20$					$l/a=16,\quad R_i/t=40$				
	f_0^A	f_1^A	f_2^A	f_3^A	f_{bg}^A	f_0^A	f_1^A	f_2^A	f_3^A	f_{bg}^A
0	1.088	0.664	0.512	0.431	1.036	1.088	0.664	0.512	0.431	1.061
0.1	1.094	0.664	0.510	0.427	1.045	1.096	0.665	0.510	0.427	1.071
0.2	1.157	0.687	0.522	0.434	1.109	1.163	0.689	0.523	0.435	1.139
0.4	1.410	0.776	0.568	0.463	1.357	1.439	0.786	0.573	0.466	1.412
0.6	1.737	0.893	0.630	0.502	1.678	1.809	0.916	0.641	0.509	1.778
0.8	2.043	1.022	0.706	0.554	1.979	2.106	1.039	0.714	0.558	2.073
a/t	$l/a=16,\quad R_i/t=80$					$l/a=16,\quad R_i/t\to\infty$				
	f_0^A	f_1^A	f_2^A	f_3^A	f_{bg}^A	f_0^A	f_1^A	f_2^A	f_3^A	f_{bg}^A
0	1.088	0.664	0.512	0.431	1.075	1.088	0.664	0.512	0.431	1.088
0.1	1.095	0.665	0.510	0.427	1.084	1.095	0.664	0.510	0.427	1.095
0.2	1.165	0.689	0.523	0.435	1.153	1.172	0.692	0.524	0.436	1.172
0.4	1.454	0.791	0.575	0.467	1.440	1.482	0.801	0.580	0.470	1.482
0.6	1.854	0.931	0.648	0.513	1.838	1.943	0.960	0.663	0.521	1.943
0.8	2.159	1.055	0.720	0.561	2.142	2.300	1.098	0.741	0.573	2.300

Table K15-5. Geometry functions for a part circumferential internal surface crack in a cylinder — deepest point of crack ($l/a = 32$).

a/t	$l/a=32,\quad R_i/t=1$					$l/a=32,\quad R_i/t=2$				
	f_0^A	f_1^A	f_2^A	f_3^A	f_{bg}^A	f_0^A	f_1^A	f_2^A	f_3^A	f_{bg}^A
0	1.105	0.673	0.518	0.435	0.553	1.105	0.673	0.518	0.435	0.737
0.1	1.054	0.653	0.505	0.425	0.562	1.086	0.665	0.512	0.430	0.746
0.2	1.050	0.656	0.510	0.430	0.564	1.108	0.674	0.517	0.433	0.778
0.4	1.079	0.672	0.520	0.438	0.594	1.234	0.730	0.553	0.459	0.853
0.6	1.200	0.730	0.557	0.464	0.675	1.421	0.811	0.601	0.492	0.973
0.8	1.549	0.904	0.669	0.545	0.892	1.829	1.003	0.721	0.577	1.247
a/t	$l/a=32,\quad R_i/t=5$					$l/a=32,\quad R_i/t=10$				
	f_0^A	f_1^A	f_2^A	f_3^A	f_{bg}^A	f_0^A	f_1^A	f_2^A	f_3^A	f_{bg}^A
0	1.105	0.673	0.518	0.435	0.921	1.105	0.673	0.518	0.435	1.005
0.1	1.111	0.674	0.517	0.433	0.937	1.120	0.677	0.519	0.434	1.025
0.2	1.173	0.697	0.530	0.441	0.996	1.202	0.708	0.535	0.444	1.102
0.4	1.377	0.774	0.572	0.467	1.181	1.479	0.810	0.590	0.479	1.361
0.6	1.690	0.896	0.639	0.512	1.428	1.881	0.959	0.671	0.531	1.734
0.8	2.193	1.113	0.769	0.601	1.809	2.446	1.188	0.802	0.619	2.226
a/t	$l/a=32,\quad R_i/t=20$					$l/a=32,\quad R_i/t=40$				
	f_0^A	f_1^A	f_2^A	f_3^A	f_{bg}^A	f_0^A	f_1^A	f_2^A	f_3^A	f_{bg}^A
0	1.105	0.673	0.518	0.435	1.052	1.105	0.673	0.518	0.435	1.078
0.1	1.125	0.679	0.519	0.434	1.075	1.127	0.679	0.520	0.435	1.102
0.2	1.220	0.714	0.539	0.447	1.169	1.231	0.718	0.541	0.448	1.204
0.4	1.556	0.837	0.604	0.488	1.496	1.609	0.856	0.614	0.494	1.577
0.6	2.042	1.013	0.698	0.547	1.966	2.175	1.058	0.721	0.561	2.135
0.8	2.627	1.240	0.826	0.630	2.571	2.776	1.284	0.845	0.641	2.726
a/t	$l/a=32,\quad R_i/t=80$					$l/a=32,\quad R_i/t\to\infty$				
	f_0^A	f_1^A	f_2^A	f_3^A	f_{bg}^A	f_0^A	f_1^A	f_2^A	f_3^A	f_{bg}^A
0	1.105	0.673	0.518	0.435	1.091	1.105	0.673	0.518	0.435	1.105
0.1	1.128	0.680	0.520	0.435	1.115	1.129	0.680	0.520	0.435	1.129
0.2	1.235	0.719	0.541	0.448	1.222	1.243	0.722	0.543	0.449	1.243
0.4	1.641	0.867	0.620	0.497	1.625	1.693	0.885	0.629	0.503	1.693
0.6	2.275	1.091	0.737	0.571	2.255	2.470	1.157	0.770	0.591	2.470
0.8	2.913	1.326	0.864	0.652	2.888	3.331	1.458	0.927	0.689	3.331

Table K15-6. Geometry functions for a part circumferential internal surface crack in a cylinder — deepest point of crack ($l/a \to \infty$).

a/t	$l/a \to \infty,\quad R_i/t = 1$					$l/a \to \infty,\quad R_i/t = 2$				
	f_0^A	f_1^A	f_2^A	f_3^A	f_{bg}^A	f_0^A	f_1^A	f_2^A	f_3^A	f_{bg}^A
0	1.122	0.683	0.526	0.441	0.561	1.122	0.683	0.526	0.441	0.748
0.1	1.067	0.660	0.511	0.431	0.555	1.107	0.676	0.520	0.436	0.751
0.2	1.050	0.656	0.510	0.430	0.564	1.130	0.686	0.527	0.441	0.777
0.4	1.079	0.672	0.520	0.438	0.594	1.234	0.730	0.553	0.459	0.853
0.6	1.200	0.730	0.557	0.464	0.675	1.421	0.811	0.601	0.492	0.973
0.8	1.549	0.904	0.669	0.545	0.892	1.829	1.003	0.721	0.577	1.247
a/t	$l/a \to \infty,\quad R_i/t = 5$					$l/a \to \infty,\quad R_i/t = 10$				
	f_0^A	f_1^A	f_2^A	f_3^A	f_{bg}^A	f_0^A	f_1^A	f_2^A	f_3^A	f_{bg}^A
0	1.122	0.683	0.526	0.441	0.935	1.122	0.683	0.526	0.441	1.020
0.1	1.140	0.688	0.527	0.441	0.954	1.155	0.694	0.530	0.443	1.049
0.2	1.211	0.718	0.544	0.453	1.019	1.255	0.735	0.554	0.459	1.144
0.4	1.440	0.808	0.595	0.487	1.207	1.583	0.861	0.625	0.506	1.436
0.6	1.768	0.937	0.669	0.535	1.462	2.060	1.046	0.726	0.572	1.848
0.8	2.281	1.161	0.804	0.629	1.867	2.700	1.307	0.880	0.676	2.410
a/t	$l/a \to \infty,\quad R_i/t = 20$					$l/a \to \infty,\quad R_i/t = 40$				
	f_0^A	f_1^A	f_2^A	f_3^A	f_{bg}^A	f_0^A	f_1^A	f_2^A	f_3^A	f_{bg}^A
0	1.122	0.683	0.526	0.441	1.069	1.122	0.683	0.526	0.441	1.095
0.1	1.165	0.699	0.532	0.444	1.106	1.171	0.700	0.534	0.445	1.138
0.2	1.287	0.747	0.561	0.464	1.224	1.310	0.756	0.566	0.467	1.273
0.4	1.706	0.908	0.651	0.523	1.614	1.807	0.946	0.672	0.537	1.746
0.6	2.362	1.153	0.785	0.610	2.217	2.660	1.262	0.844	0.647	2.551
0.8	3.212	1.485	0.973	0.734	3.015	3.834	1.702	1.086	0.805	3.695
a/t	$l/a \to \infty,\quad R_i/t = 80$					$l/a \to \infty,\quad R_i/t \to \infty$				
	f_0^A	f_1^A	f_2^A	f_3^A	f_{bg}^A	f_0^A	f_1^A	f_2^A	f_3^A	f_{bg}^A
0	1.122	0.683	0.526	0.441	1.108	1.122	0.683	0.526	0.441	1.122
0.1	1.175	0.702	0.535	0.446	1.155	1.185	0.706	0.537	0.447	1.185
0.2	1.326	0.762	0.569	0.469	1.303	1.364	0.777	0.578	0.475	1.364
0.4	1.886	0.976	0.688	0.547	1.842	2.109	1.061	0.736	0.584	2.109
0.6	2.935	1.362	0.898	0.682	2.844	4.030	1.764	1.115	0.822	4.030
0.8	4.570	1.960	1.221	0.889	4.460	11.949	4.546	2.573	1.734	11.949

Table K16-1. Geometry functions for a part circumferential internal surface crack in a cylinder — intersection of crack with free surface ($l/a = 2$).

a/t	$l/a=2,\ R_i/t=1$					$l/a=2,\ R_i/t=2$				
	f_0^B	f_1^B	f_2^B	f_3^B	f_{bg}^B	f_0^B	f_1^B	f_2^B	f_3^B	f_{bg}^B
0	0.744	0.129	0.005	0.002	0.372	0.744	0.129	0.005	0.002	0.496
0.1	0.721	0.121	0.005	0.002	0.367	0.731	0.122	0.005	0.002	0.492
0.2	0.711	0.120	0.005	0.002	0.364	0.727	0.122	0.005	0.002	0.492
0.4	0.696	0.123	0.005	0.003	0.317	0.726	0.127	0.005	0.003	0.495
0.6	0.730	0.136	0.006	0.003	0.381	0.769	0.141	0.006	0.003	0.527
0.8	0.807	0.163	0.007	0.004	0.432	0.837	0.161	0.007	0.004	0.577
a/t	$l/a=2,\ R_i/t=5$					$l/a=2,\ R_i/t=10$				
	f_0^B	f_1^B	f_2^B	f_3^B	f_{bg}^B	f_0^B	f_1^B	f_2^B	f_3^B	f_{bg}^B
0	0.744	0.129	0.005	0.002	0.620	0.744	0.129	0.005	0.002	0.676
0.1	0.737	0.122	0.005	0.002	0.616	0.739	0.125	0.005	0.002	0.673
0.2	0.738	0.124	0.005	0.002	0.619	0.742	0.124	0.005	0.002	0.677
0.4	0.753	0.131	0.005	0.003	0.635	0.765	0.133	0.005	0.003	0.699
0.6	0.805	0.147	0.006	0.003	0.681	0.821	0.150	0.006	0.003	0.753
0.8	0.870	0.164	0.006	0.003	0.741	0.888	0.166	0.007	0.003	0.817
a/t	$l/a=2,\ R_i/t=20$					$l/a=2,\ R_i/t=40$				
	f_0^B	f_1^B	f_2^B	f_3^B	f_{bg}^B	f_0^B	f_1^B	f_2^B	f_3^B	f_{bg}^B
0	0.744	0.129	0.005	0.002	0.709	0.744	0.129	0.005	0.002	0.726
0.1	0.740	0.123	0.005	0.002	0.705	0.740	0.123	0.005	0.002	0.723
0.2	0.744	0.124	0.005	0.002	0.710	0.745	0.124	0.005	0.002	0.727
0.4	0.772	0.134	0.005	0.003	0.738	0.776	0.135	0.005	0.003	0.758
0.6	0.830	0.151	0.006	0.003	0.795	0.835	0.152	0.006	0.003	0.817
0.8	0.899	0.168	0.007	0.003	0.862	0.904	0.169	0.007	0.003	0.886
a/t	$l/a=2,\ R_i/t=80$					$l/a=2,\ R_i/t\to\infty$				
	f_0^B	f_1^B	f_2^B	f_3^B	f_{bg}^B	f_0^B	f_1^B	f_2^B	f_3^B	f_{bg}^B
0	0.744	0.129	0.005	0.002	0.735	0.744	0.129	0.005	0.002	0.744
0.1	0.740	0.123	0.005	0.002	0.732	0.740	0.123	0.005	0.002	0.740
0.2	0.745	0.124	0.005	0.002	0.736	0.746	0.125	0.005	0.002	0.746
0.4	0.776	0.135	0.005	0.003	0.768	0.781	0.136	0.005	0.003	0.781
0.6	0.835	0.152	0.006	0.003	0.826	0.844	0.155	0.006	0.003	0.844
0.8	0.903	0.168	0.007	0.003	0.894	0.920	0.173	0.007	0.004	0.920

Table K16-2. Geometry functions for a part circumferential internal surface crack in a cylinder — intersection of crack with free surface ($l/a = 4$).

a/t	$l/a=4,\ R_i/t=1$					$l/a=4,\ R_i/t=2$				
	f_0^B	f_1^B	f_2^B	f_3^B	f_{bg}^B	f_0^B	f_1^B	f_2^B	f_3^B	f_{bg}^B
0	0.704	0.119	0.004	0.002	0.352	0.704	0.119	0.004	0.002	0.469
0.1	0.689	0.107	0.004	0.002	0.347	0.698	0.109	0.004	0.002	0.468
0.2	0.682	0.106	0.004	0.002	0.334	0.700	0.110	0.004	0.002	0.468
0.4	0.677	0.110	0.004	0.002	0.287	0.723	0.121	0.005	0.002	0.473
0.6	0.712	0.124	0.005	0.003	0.236	0.778	0.140	0.006	0.003	0.493
0.8	0.804	0.158	0.007	0.004	0.171	0.865	0.169	0.007	0.004	0.512
a/t	$l/a=4,\ R_i/t=5$					$l/a=4,\ R_i/t=10$				
	f_0^B	f_1^B	f_2^B	f_3^B	f_{bg}^B	f_0^B	f_1^B	f_2^B	f_3^B	f_{bg}^B
0	0.704	0.119	0.004	0.002	0.587	0.704	0.119	0.004	0.002	0.640
0.1	0.703	0.110	0.004	0.002	0.588	0.705	0.110	0.004	0.002	0.642
0.2	0.712	0.113	0.004	0.002	0.596	0.716	0.114	0.004	0.002	0.652
0.4	0.761	0.131	0.005	0.003	0.637	0.777	0.135	0.005	0.003	0.709
0.6	0.846	0.158	0.006	0.003	0.708	0.880	0.167	0.007	0.004	0.806
0.8	0.949	0.187	0.008	0.004	0.791	1.001	0.199	0.008	0.004	0.918
a/t	$l/a=4,\ R_i/t=20$					$l/a=4,\ R_i/t=40$				
	f_0^B	f_1^B	f_2^B	f_3^B	f_{bg}^B	f_0^B	f_1^B	f_2^B	f_3^B	f_{bg}^B
0	0.704	0.119	0.004	0.002	0.670	0.704	0.119	0.004	0.002	0.687
0.1	0.705	0.110	0.004	0.002	0.673	0.706	0.110	0.004	0.002	0.689
0.2	0.718	0.115	0.004	0.002	0.685	0.719	0.115	0.004	0.002	0.702
0.4	0.786	0.138	0.005	0.003	0.751	0.791	0.139	0.005	0.003	0.773
0.6	0.902	0.173	0.007	0.004	0.864	0.915	0.177	0.007	0.004	0.895
0.8	1.038	0.208	0.009	0.005	0.995	1.061	0.215	0.009	0.005	1.039
a/t	$l/a=4,\ R_i/t=80$					$l/a=4,\ R_i/t\to\infty$				
	f_0^B	f_1^B	f_2^B	f_3^B	f_{bg}^B	f_0^B	f_1^B	f_2^B	f_3^B	f_{bg}^B
0	0.704	0.119	0.004	0.002	0.695	0.704	0.119	0.004	0.002	0.704
0.1	0.706	0.110	0.004	0.002	0.698	0.706	0.101	0.004	0.002	0.706
0.2	0.719	0.115	0.004	0.002	0.711	0.720	0.116	0.004	0.002	0.720
0.4	0.792	0.139	0.005	0.003	0.783	0.800	0.142	0.006	0.003	0.800
0.6	0.918	0.178	0.007	0.004	0.909	0.940	0.185	0.008	0.004	0.940
0.8	1.069	0.217	0.009	0.005	1.059	1.110	0.229	0.009	0.005	1.110

Table K16-3. Geometry functions for a part circumferential internal surface crack in a cylinder — intersection of crack with free surface ($l/a=8$).

a/t	$l/a=8,\quad R_i/t=1$					$l/a=8,\quad R_i/t=2$				
	f_0^B	f_1^B	f_2^B	f_3^B	f_{bg}^B	f_0^B	f_1^B	f_2^B	f_3^B	f_{bg}^B
0	0.568	0.007	0.002	0.001	0.284	0.568	0.007	0.002	0.001	0.379
0.1	0.566	0.007	0.000	0.001	0.269	0.573	0.007	0.002	0.001	0.379
0.2	0.561	0.007	0.002	0.001	0.254	0.579	0.007	0.002	0.001	0.366
0.4	0.565	0.007	0.002	0.001	0.005	0.603	0.008	0.003	0.001	0.315
0.6	0.585	0.008	0.003	0.001	0.000	0.650	0.010	0.004	0.002	0.237
0.8	0.685	0.000	0.000	0.000	0.000	0.727	0.122	0.005	0.003	0.145
a/t	$l/a=8,\quad R_i/t=5$					$l/a=8,\quad R_i/t=10$				
	f_0^B	f_1^B	f_2^B	f_3^B	f_{bg}^B	f_0^B	f_1^B	f_2^B	f_3^B	f_{bg}^B
0	0.568	0.007	0.002	0.001	0.473	0.568	0.007	0.002	0.001	0.516
0.1	0.578	0.007	0.002	0.001	0.482	0.579	0.007	0.002	0.001	0.527
0.2	0.592	0.008	0.002	0.001	0.490	0.597	0.008	0.002	0.001	0.543
0.4	0.648	0.009	0.003	0.002	0.525	0.671	0.102	0.004	0.002	0.608
0.6	0.731	0.121	0.005	0.002	0.572	0.784	0.136	0.005	0.003	0.705
0.8	0.850	0.155	0.006	0.003	0.639	0.931	0.176	0.007	0.004	0.831
a/t	$l/a=8,\quad R_i/t=20$					$l/a=8,\quad R_i/t=40$				
	f_0^B	f_1^B	f_2^B	f_3^B	f_{bg}^B	f_0^B	f_1^B	f_2^B	f_3^B	f_{bg}^B
0	0.568	0.007	0.002	0.001	0.541	0.568	0.007	0.002	0.001	0.554
0.1	0.580	0.007	0.002	0.001	0.553	0.581	0.007	0.002	0.001	0.567
0.2	0.600	0.008	0.003	0.001	0.572	0.602	0.008	0.003	0.001	0.587
0.4	0.686	0.106	0.004	0.002	0.654	0.694	0.109	0.004	0.002	0.678
0.6	0.823	0.148	0.006	0.003	0.785	0.849	0.156	0.006	0.003	0.830
0.8	1.001	0.196	0.008	0.004	0.954	1.055	0.211	0.009	0.005	1.032
a/t	$l/a=8,\quad R_i/t=80$					$l/a=8,\quad R_i/t\to\infty$				
	f_0^B	f_1^B	f_2^B	f_3^B	f_{bg}^B	f_0^B	f_1^B	f_2^B	f_3^B	f_{bg}^B
0	0.568	0.007	0.002	0.001	0.561	0.568	0.007	0.002	0.001	0.568
0.1	0.581	0.007	0.002	0.001	0.574	0.580	0.007	0.002	0.001	0.580
0.2	0.602	0.008	0.003	0.001	0.595	0.603	0.008	0.003	0.001	0.603
0.4	0.698	0.110	0.004	0.002	0.690	0.708	0.114	0.004	0.002	0.708
0.6	0.864	0.161	0.006	0.003	0.854	0.894	0.171	0.007	0.004	0.894
0.8	1.088	0.221	0.009	0.005	1.076	1.160	0.242	0.101	0.005	1.160

Table K16-4. Geometry functions for a part circumferential internal surface crack in a cylinder — intersection of crack with free surface ($l/a=16$).

a/t	$l/a=16,\quad R_i/t=1$					$l/a=16,\quad R_i/t=2$				
	f_0^B	f_1^B	f_2^B	f_3^B	f_{bg}^B	f_0^B	f_1^B	f_2^B	f_3^B	f_{bg}^B
0	0.432	0.004	0.001	0.000	0.216	0.432	0.004	0.001	0.000	0.288
0.1	0.432	0.003	0.001	0.000	0.185	0.437	0.003	0.001	0.000	0.272
0.2	0.429	0.003	0.001	0.000	0.001	0.441	0.004	0.001	0.000	0.215
0.4	-	0.000	0.000	0.000	0.000	0.455	0.004	0.001	0.000	0.000
0.6	-	0.000	0.000	0.000	0.000	0.478	0.005	0.001	0.001	0.000
0.8	-	0.000	0.000	0.000	0.000	-	0.000	0.000	0.000	0.000
a/t	$l/a=16,\quad R_i/t=5$					$l/a=16,\quad R_i/t=10$				
	f_0^B	f_1^B	f_2^B	f_3^B	f_{bg}^B	f_0^B	f_1^B	f_2^B	f_3^B	f_{bg}^B
0	0.432	0.004	0.001	0.000	0.360	0.432	0.004	0.001	0.000	0.393
0.1	0.441	0.004	0.001	0.000	0.363	0.442	0.004	0.001	0.000	0.401
0.2	0.452	0.004	0.001	0.000	0.360	0.457	0.004	0.001	0.000	0.412
0.4	0.488	0.005	0.002	0.001	0.344	0.509	0.006	0.002	0.001	0.444
0.6	0.540	0.007	0.002	0.001	0.298	0.585	0.008	0.003	0.001	0.489
0.8	0.612	0.009	0.003	0.002	0.236	0.696	0.111	0.004	0.002	0.552
a/t	$l/a=16,\quad R_i/t=20$					$l/a=16,\quad R_i/t=40$				
	f_0^B	f_1^B	f_2^B	f_3^B	f_{bg}^B	f_0^B	f_1^B	f_2^B	f_3^B	f_{bg}^B
0	0.432	0.004	0.001	0.000	0.411	0.432	0.004	0.001	0.000	0.421
0.1	0.443	0.004	0.001	0.000	0.422	0.443	0.004	0.001	0.000	0.433
0.2	0.461	0.004	0.001	0.001	0.438	0.463	0.004	0.001	0.001	0.451
0.4	0.525	0.006	0.002	0.001	0.496	0.536	0.007	0.002	0.001	0.522
0.6	0.624	0.009	0.003	0.002	0.585	0.657	0.100	0.004	0.002	0.639
0.8	0.768	0.131	0.005	0.003	0.712	0.833	0.150	0.006	0.003	0.809
a/t	$l/a=16,\quad R_i/t=80$					$l/a=16,\quad R_i/t\to\infty$				
	f_0^B	f_1^B	f_2^B	f_3^B	f_{bg}^B	f_0^B	f_1^B	f_2^B	f_3^B	f_{bg}^B
0	0.432	0.004	0.001	0.000	0.427	0.432	0.004	0.001	0.000	0.432
0.1	0.443	0.004	0.001	0.000	0.438	0.441	0.004	0.001	0.000	0.441
0.2	0.463	0.004	0.001	0.001	0.458	0.465	0.004	0.001	0.001	0.465
0.4	0.543	0.007	0.002	0.001	0.536	0.554	0.007	0.003	0.001	0.554
0.6	0.680	0.108	0.004	0.002	0.672	0.720	0.121	0.005	0.003	0.720
0.8	0.887	0.166	0.007	0.004	0.876	1.000	0.200	0.008	0.005	1.000

Table K16-5. Geometry functions for a part circumferential internal surface crack in a cylinder — intersection of crack with free surface ($l/a = 32$).

a/t	$l/a=32,\quad R_i/t=1$					$l/a=32,\quad R_i/t=2$				
	f_0^B	f_1^B	f_2^B	f_3^B	f_{bg}^B	f_0^B	f_1^B	f_2^B	f_3^B	f_{bg}^B
0	0.282	0.002	0.000	0.000	0.141	0.282	0.002	0.000	0.000	0.188
0.1	0.326	0.002	0.000	0.000	0.000	0.329	0.002	0.000	0.000	0.155
0.2	-	0.000	0.000	0.000	0.000	0.331	0.002	0.000	0.000	0.000
0.4	-	0.000	0.000	0.000	0.000	-	0.000	0.000	0.000	0.000
0.6	-	0.000	0.000	0.000	0.000	-	0.000	0.000	0.000	0.000
0.8	-	0.000	0.000	0.000	0.000	-	0.000	0.000	0.000	0.000
a/t	$l/a=32,\quad R_i/t=5$					$l/a=32,\quad R_i/t=10$				
	f_0^B	f_1^B	f_2^B	f_3^B	f_{bg}^B	f_0^B	f_1^B	f_2^B	f_3^B	f_{bg}^B
0	0.282	0.002	0.000	0.000	0.235	0.282	0.002	0.000	0.000	0.256
0.1	0.331	0.002	0.000	0.000	0.263	0.332	0.002	0.000	0.000	0.299
0.2	0.338	0.002	0.000	0.000	0.231	0.342	0.002	0.000	0.000	0.296
0.4	0.356	0.002	0.001	0.000	0.010	0.368	0.003	0.001	0.000	0.276
0.6	0.373	0.003	0.001	0.000	0.000	0.400	0.003	0.001	0.000	0.227
0.8	0.391	0.003	0.001	0.000	0.000	0.439	0.004	0.001	0.001	0.156
a/t	$l/a=32,\quad R_i/t=20$					$l/a=32,\quad R_i/t=40$				
	f_0^B	f_1^B	f_2^B	f_3^B	f_{bg}^B	f_0^B	f_1^B	f_2^B	f_3^B	f_{bg}^B
0	0.282	0.002	0.000	0.000	0.269	0.282	0.002	0.000	0.000	0.275
0.1	0.333	0.002	0.000	0.000	0.316	0.333	0.002	0.000	0.000	0.325
0.2	0.345	0.002	0.000	0.000	0.325	0.347	0.002	0.000	0.000	0.338
0.4	0.379	0.003	0.001	0.000	0.345	0.388	0.003	0.001	0.000	0.375
0.6	0.426	0.004	0.001	0.001	0.367	0.448	0.005	0.002	0.001	0.428
0.8	0.498	0.006	0.002	0.001	0.402	0.548	0.008	0.003	0.002	0.516
a/t	$l/a=32,\quad R_i/t=80$					$l/a=32,\quad R_i/t\to\infty$				
	f_0^B	f_1^B	f_2^B	f_3^B	f_{bg}^B	f_0^B	f_1^B	f_2^B	f_3^B	f_{bg}^B
0	0.282	0.002	0.000	0.000	0.279	0.282	0.002	0.000	0.000	0.282
0.1	0.334	0.002	0.000	0.000	0.400	0.333	0.002	0.000	0.000	0.333
0.2	0.348	0.002	0.001	0.000	0.344	0.349	0.002	0.001	0.000	0.349
0.4	0.395	0.003	0.001	0.001	0.389	0.406	0.004	0.001	0.001	0.406
0.6	0.468	0.005	0.002	0.001	0.460	0.511	0.007	0.003	0.001	0.511
0.8	0.592	0.009	0.003	0.002	0.580	0.723	0.129	0.005	0.003	0.723

Table K16-6. Geometry functions for a part circumferential internal surface crack in a cylinder — intersection of crack with free surface ($l/a \to \infty$).

a/t	$l/a \to \infty,\quad R_i/t = 1$					$l/a \to \infty,\quad R_i/t = 2$				
	f_0^B	f_1^B	f_2^B	f_3^B	f_{bg}^B	f_0^B	f_1^B	f_2^B	f_3^B	f_{bg}^B
0	0.000	0.000	0.000	0.000	0.000	0.000	0.000	0.000	0.000	0.000
0.1	0.000	0.000	0.000	0.000	0.000	0.000	0.000	0.000	0.000	0.000
0.2	0.000	0.000	0.000	0.000	0.000	0.000	0.000	0.000	0.000	0.000
0.4	0.000	0.000	0.000	0.000	0.000	0.000	0.000	0.000	0.000	0.000
0.6	0.000	0.000	0.000	0.000	0.000	0.000	0.000	0.000	0.000	0.000
0.8	0.000	0.000	0.000	0.000	0.000	0.000	0.000	0.000	0.000	0.000
a/t	$l/a \to \infty,\quad R_i/t = 5$					$l/a \to \infty,\quad R_i/t = 10$				
	f_0^B	f_1^B	f_2^B	f_3^B	f_{bg}^B	f_0^B	f_1^B	f_2^B	f_3^B	f_{bg}^B
0	0.000	0.000	0.000	0.000	0.000	0.000	0.000	0.000	0.000	0.000
0.1	0.000	0.000	0.000	0.000	0.000	0.000	0.000	0.000	0.000	0.000
0.2	0.000	0.000	0.000	0.000	0.000	0.000	0.000	0.000	0.000	0.000
0.4	0.000	0.000	0.000	0.000	0.000	0.000	0.000	0.000	0.000	0.000
0.6	0.000	0.000	0.000	0.000	0.000	0.000	0.000	0.000	0.000	0.000
0.8	0.000	0.000	0.000	0.000	0.000	0.000	0.000	0.000	0.000	0.000
a/t	$l/a \to \infty,\quad R_i/t = 20$					$l/a \to \infty,\quad R_i/t = 40$				
	f_0^B	f_1^B	f_2^B	f_3^B	f_{bg}^B	f_0^B	f_1^B	f_2^B	f_3^B	f_{bg}^B
0	0.000	0.000	0.000	0.000	0.000	0.000	0.000	0.000	0.000	0.000
0.1	0.000	0.000	0.000	0.000	0.000	0.000	0.000	0.000	0.000	0.000
0.2	0.000	0.000	0.000	0.000	0.000	0.000	0.000	0.000	0.000	0.000
0.4	0.000	0.000	0.000	0.000	0.000	0.000	0.000	0.000	0.000	0.000
0.6	0.000	0.000	0.000	0.000	0.000	0.000	0.000	0.000	0.000	0.000
0.8	0.000	0.000	0.000	0.000	0.000	0.000	0.000	0.000	0.000	0.000
a/t	$l/a \to \infty,\quad R_i/t = 80$					$l/a \to \infty,\quad R_i/t \to \infty$				
	f_0^B	f_1^B	f_2^B	f_3^B	f_{bg}^B	f_0^B	f_1^B	f_2^B	f_3^B	f_{bg}^B
0	0.000	0.000	0.000	0.000	0.000	0.000	0.000	0.000	0.000	0.000
0.1	0.000	0.000	0.000	0.000	0.000	0.000	0.000	0.000	0.000	0.000
0.2	0.000	0.000	0.000	0.000	0.000	0.000	0.000	0.000	0.000	0.000
0.4	0.000	0.000	0.000	0.000	0.000	0.000	0.000	0.000	0.000	0.000
0.6	0.000	0.000	0.000	0.000	0.000	0.000	0.000	0.000	0.000	0.000
0.8	0.000	0.000	0.000	0.000	0.000	0.000	0.000	0.000	0.000	0.000

K3.2 Complete circumferential internal surface crack

K_I is given by

$$K_I = \frac{1}{\sqrt{2\pi a}} \int_0^a \sigma(u) \sum_{j=1}^{3} f_j\left(a/t, R_i/t\right) \left(1 - \frac{u}{a}\right)^{j-\frac{3}{2}} du \quad . \qquad \text{(K18)}$$

The stress state $\sigma = \sigma(u)$ is to be taken normal to the prospective crack plane in an uncracked cylinder. The coordinate *u* is defined in Fig. G3.2.

f_j (j = 1 to 3) are geometry functions which are given in Table K17 for the deepest point of the crack (f^A). See Fig. G3.2.

Remark: The cylinder should be long in the transverse direction to the crack so that edge effects do not influence the results.

Ref.: [K3].

Table K17. Geometry functions for a complete circumferential internal surface crack in a cylinder.

a/t	$R_i/t = 7/3$		
	f_1^A	f_2^A	f_3^A
0	2.000	1.327	0.218
0.1	2.000	1.337	0.200
0.2	2.000	1.543	0.201
0.3	2.000	1.880	0.228
0.4	2.000	2.321	0.293
0.5	2.000	2.879	0.373
0.6	2.000	3.720	0.282
a/t	$R_i/t = 4$		
	f_1^A	f_2^A	f_3^A
0	2.000	1.336	0.218
0.1	2.000	1.460	0.206
0.2	2.000	1.839	0.241
0.3	2.000	2.359	0.353
0.4	2.000	2.976	0.556
0.5	2.000	3.688	0.837
0.6	2.000	4.598	1.086
a/t	$R_i/t = 9$		
	f_1^A	f_2^A	f_3^A
0	2.000	1.346	0.219
0.1	2.000	1.591	0.211
0.2	2.000	2.183	0.279
0.3	2.000	2.966	0.518
0.4	2.000	3.876	0.956
0.5	2.000	4.888	1.614
0.6	2.000	5.970	2.543

K3.3 Part circumferential external surface crack

K_I is given by

$$K_I = \sqrt{\pi a}\left(\sum_{j=0}^{3}\sigma_j f_j\left(a/t, l/a, R_i/t\right) + \sigma_{bg} f_{bg}\left(a/t, l/a, R_i/t\right)\right) \quad . \tag{K19}$$

where σ_j (j = 0 to 3) are stress components which define the stress state σ according to

$$\sigma = \sigma(u) = \sum_{j=0}^{3}\sigma_j\left(\frac{u}{a}\right)^j \qquad \text{for } 0 \le u \le a \quad , \tag{K20}$$

and σ_{bg} is the global bending stress. σ and σ_{bg} are to be taken normal to the prospective crack plane in an uncracked cylinder. σ_j is determined by fitting σ to Eq. (K20). The coordinate u is defined in Fig. G3.3.

f_j (j = 0 to 3) and f_{bg} are geometry functions which are given in Tables K18 and K19 for the deepest point of the crack (f^A), and at the intersection of the crack with the free surface (f^B), respectively. See Fig. G3.3.

Remark: The cylinder should be long in the transverse direction to the crack so that edge effects do not influence.

Ref.: [K1] and [K8].

Table K18. Geometry functions for a part circumferential external surface crack in a cylinder — deepest point of crack.

a/t	$l/a=2,\quad R_i/t=5$					$l/a=2,\quad R_i/t=10$				
	f_0^A	f_1^A	f_2^A	f_3^A	f_{bg}^A	f_0^A	f_1^A	f_2^A	f_3^A	f_{bg}^A
0	0.659	0.471	0.387	0.337	0.659	0.659	0.471	0.387	0.337	0.659
0.2	0.661	0.455	0.367	0.313	0.645	0.662	0.456	0.368	0.313	0.653
0.4	0.673	0.462	0.374	0.321	0.642	0.676	0.464	0.376	0.322	0.659
0.6	0.686	0.467	0.378	0.325	0.638	0.690	0.470	0.381	0.328	0.664
0.8	0.690	0.477	0.387	0.333	0.626	0.695	0.482	0.392	0.337	0.660
a/t	$l/a=4,\quad R_i/t=5$					$l/a=4,\quad R_i/t=10$				
	f_0^A	f_1^A	f_2^A	f_3^A	f_{bg}^A	f_0^A	f_1^A	f_2^A	f_3^A	f_{bg}^A
0	0.886	0.565	0.430	0.352	0.886	0.886	0.565	0.430	0.352	0.886
0.2	0.905	0.560	0.425	0.347	0.885	0.903	0.559	0.425	0.347	0.891
0.4	0.972	0.586	0.443	0.363	0.932	0.969	0.586	0.443	0.363	0.947
0.6	1.060	0.618	0.462	0.378	0.995	1.051	0.616	0.462	0.378	1.016
0.8	1.133	0.659	0.493	0.403	1.041	1.108	0.654	0.491	0.403	1.059
a/t	$l/a=8,\quad R_i/t=5$					$l/a=8,\quad R_i/t=10$				
	f_0^A	f_1^A	f_2^A	f_3^A	f_{bg}^A	f_0^A	f_1^A	f_2^A	f_3^A	f_{bg}^A
0	1.025	0.600	0.441	0.356	1.025	1.025	0.600	0.441	0.356	1.025
0.2	1.078	0.638	0.476	0.386	1.055	1.073	0.637	0.475	0.386	1.060
0.4	1.253	0.702	0.513	0.413	1.202	1.246	0.700	0.512	0.413	1.219
0.6	1.502	0.790	0.561	0.446	1.413	1.489	0.786	0.559	0.445	1.443
0.8	1.773	0.900	0.625	0.490	1.631	1.711	0.880	0.616	0.484	1.640
a/t	$l/a=16,\quad R_i/t=5$					$l/a=16,\quad R_i/t=10$				
	f_0^A	f_1^A	f_2^A	f_3^A	f_{bg}^A	f_0^A	f_1^A	f_2^A	f_3^A	f_{bg}^A
0	1.079	0.635	0.473	0.388	1.079	1.079	0.635	0.473	0.388	1.079
0.2	1.186	0.685	0.504	0.406	1.162	1.182	0.684	0.504	0.405	1.168
0.4	1.482	0.797	0.570	0.454	1.419	1.491	0.800	0.571	0.454	1.458
0.6	1.907	0.951	0.654	0.508	1.779	1.949	0.962	0.658	0.511	1.883
0.8	2.461	1.166	0.776	0.591	2.220	2.479	1.165	0.772	0.587	2.363
a/t	$l/a=32,\quad R_i/t=5$					$l/a=32,\quad R_i/t=10$				
	f_0^A	f_1^A	f_2^A	f_3^A	f_{bg}^A	f_0^A	f_1^A	f_2^A	f_3^A	f_{bg}^A
0	1.101	0.658	0.499	0.413	1.101	1.101	0.658	0.499	0.413	1.101
0.2	1.252	0.716	0.525	0.422	1.225	1.252	0.716	0.525	0.421	1.237
0.4	1.599	0.854	0.607	0.482	1.525	1.651	0.869	0.614	0.485	1.611
0.6	2.067	1.036	0.713	0.555	1.926	2.243	1.089	0.736	0.566	2.157
0.8	2.740	1.313	0.875	0.666	2.491	3.011	1.387	0.904	0.678	2.845

Table K19. Geometry functions for a part circumferential external surface crack in a cylinder — intersection of crack with free surface.

a/t	$l/a=2,\quad R_i/t=5$					$l/a=2,\quad R_i/t=10$				
	f_0^B	f_1^B	f_2^B	f_3^B	f_{bg}^B	f_0^B	f_1^B	f_2^B	f_3^B	f_{bg}^B
0	0.715	0.117	0.040	0.020	0.717	0.713	0.117	0.041	0.020	0.713
0.2	0.748	0.125	0.045	0.023	0.744	0.748	0.125	0.046	0.023	0.745
0.4	0.781	0.133	0.050	0.026	0.771	0.783	0.133	0.051	0.026	0.777
0.6	0.837	0.147	0.057	0.030	0.821	0.841	0.149	0.058	0.030	0.832
0.8	0.905	0.163	0.063	0.033	0.880	0.912	0.166	0.064	0.033	0.898
a/t	$l/a=4,\quad R_i/t=5$					$l/a=4,\quad R_i/t=10$				
	f_0^B	f_1^B	f_2^B	f_3^B	f_{bg}^B	f_0^B	f_1^B	f_2^B	f_3^B	f_{bg}^B
0	0.654	0.088	0.028	0.013	0.657	0.649	0.087	0.028	0.013	0.649
0.2	0.724	0.110	0.040	0.020	0.719	0.723	0.110	0.040	0.020	0.720
0.4	0.794	0.132	0.052	0.027	0.781	0.797	0.133	0.052	0.027	0.791
0.6	0.915	0.168	0.069	0.037	0.888	0.925	0.172	0.071	0.038	0.912
0.8	1.059	0.208	0.087	0.046	1.012	1.081	0.215	0.089	0.048	1.058
a/t	$l/a=8,\quad R_i/t=5$					$l/a=8,\quad R_i/t=10$				
	f_0^B	f_1^B	f_2^B	f_3^B	f_{bg}^B	f_0^B	f_1^B	f_2^B	f_3^B	f_{bg}^B
0	0.527	0.047	0.010	0.003	0.537	0.518	0.043	0.009	0.002	0.521
0.2	0.610	0.074	0.024	0.011	0.603	0.610	0.074	0.024	0.011	0.607
0.4	0.693	0.101	0.038	0.019	0.669	0.702	0.105	0.039	0.020	0.693
0.6	0.818	0.139	0.055	0.029	0.762	0.856	0.152	0.062	0.033	0.834
0.8	0.972	0.185	0.077	0.041	0.868	1.060	0.211	0.088	0.047	1.019
a/t	$l/a=16,\quad R_i/t=5$					$l/a=16,\quad R_i/t=10$				
	f_0^B	f_1^B	f_2^B	f_3^B	f_{bg}^B	f_0^B	f_1^B	f_2^B	f_3^B	f_{bg}^B
0	0.425	0.029	0.004	0.001	0.454	0.409	0.023	0.003	0.000	0.417
0.2	0.459	0.040	0.010	0.004	0.443	0.461	0.040	0.011	0.004	0.455
0.4	0.493	0.050	0.016	0.007	0.432	0.513	0.057	0.019	0.009	0.493
0.6	0.529	0.058	0.018	0.008	0.390	0.589	0.078	0.028	0.014	0.542
0.8	0.542	0.057	0.016	0.006	0.294	0.671	0.099	0.037	0.018	0.582
a/t	$l/a=32,\quad R_i/t=5$					$l/a=32,\quad R_i/t=10$				
	f_0^B	f_1^B	f_2^B	f_3^B	f_{bg}^B	f_0^B	f_1^B	f_2^B	f_3^B	f_{bg}^B
0	0.307	0.017	0.005	0.000	0.379	0.299	0.021	0.002	0.000	0.323
0.2	0.306	0.016	0.003	0.000	0.265	0.309	0.020	0.003	0.000	0.296
0.4	0.305	0.014	0.001	0.000	0.151	0.319	0.019	0.004	0.000	0.269
0.6	0.299	0.008	0.000	0.000	0.024	0.322	0.016	0.002	0.000	0.208
0.8	0.292	0.003	0.000	0.000	0.255	0.305	0.005	0.000	0.000	0.103

K3.4 Complete circumferential external surface crack

K_I is given by

$$K_I = \frac{1}{\sqrt{2\pi a}} \int_0^a \sigma(u) \sum_{j=1}^{3} f_j(a/t, R_i/t) \left(1 - \frac{u}{a}\right)^{j-\frac{3}{2}} du \quad . \qquad \text{(K21)}$$

The stress state $\sigma = \sigma(u)$ is to be taken normal to the prospective crack plane in an uncracked cylinder. The coordinate *u* is defined in Fig. G3.4.

f_j (j = 1 to 3) are geometry functions which are given in Table K20 for the deepest point of the crack (f^A). See Fig. G3.4.

Remark: The cylinder should be long in the transverse direction to the crack so that edge effects do not influence the results.

Ref.: [K3].

Table K20. Geometry functions for a complete circumferential external surface crack in a cylinder.

a/t	$R_i/t = 7/3$		
	f_1^A	f_2^A	f_3^A
0	2.000	1.359	0.220
0.1	2.000	1.642	0.236
0.2	2.000	2.127	0.307
0.3	2.000	2.727	0.447
0.4	2.000	3.431	0.668
0.5	2.000	4.271	0.951
0.6	2.000	5.406	1.183
a/t	$R_i/t = 4$		
	f_1^A	f_2^A	f_3^A
0	2.000	1.362	0.221
0.1	2.000	1.659	0.221
0.2	2.000	2.220	0.303
0.3	2.000	2.904	0.535
0.4	2.000	3.701	0.857
0.5	2.000	4.603	1.311
0.6	2.000	5.671	1.851
a/t	$R_i/t = 9$		
	f_1^A	f_2^A	f_3^A
0	2.000	1.364	0.220
0.1	2.000	1.694	0.211
0.2	2.000	2.375	0.310
0.3	2.000	3.236	0.630
0.4	2.000	4.252	1.136
0.5	2.000	5.334	1.972
0.6	2.000	6.606	2.902

K3.5 Through-thickness crack

K_1 is given by

$$K_1 = \sqrt{\pi l_m / 2}\left(\sum_{j=0}^{4} \sigma_j f_j(l_m / R_m, R_i / t) + \sigma_{bg} f_{bg}(l_m / R_m, R_i / t) \right) \quad , \tag{K22}$$

where σ_j (j = 0 to 4) are stress components according to

$$\sigma = \sigma(u) = \sum_{j=0}^{4} \sigma_j \left(\frac{u}{t} \right)^j \qquad \text{for } 0 \le u \le t \quad , \tag{K23}$$

and σ_{bg} are global bending stress. The parameters l_m, R_i and R_m and the coordinate u is defined in Fig. G3.5.

The geometry functions f_j and f_{bg} are given in Tables K21 and K22 for the intersections of the crack with the free surface at $u = 0$ (f^A) and at $u = t$ (f^B), respectively. See Fig. G3.5.

Remarks: The cylinder should be long in the transverse direction to the crack so that edge effects do not influence the results. The small negative values given in Table K21-1 to K21-3 are the result of the fitting procedure in [K7].

Ref.: [K7].

Table K21-1. Geometry functions for a circumferential through-thickness crack in a cylinder — intersection of crack with free surface at $u = 0$ ($R_i / t = 5, 10$).

$R_i / t = 5$						
$l_m / \pi R_m$	f_0^A	f_1^A	f_2^A	f_3^A	f_4^A	f_{bg}^A
0.06	0.991	0.098	0.002	-0.025	-0.022	0.839
0.10	0.967	0.131	0.022	-0.011	-0.024	0.820
0.20	1.001	0.227	0.096	0.049	0.027	0.849
0.30	1.136	0.352	0.192	0.127	0.092	0.954
0.40	1.354	0.503	0.304	0.215	0.165	1.114
0.50	1.644	0.681	0.430	0.313	0.245	1.315
0.60	2.009	0.889	0.575	0.425	0.336	1.553
0.70	2.461	1.137	0.747	0.556	0.443	1.830
0.80	3.028	1.442	0.956	0.715	0.571	2.156
0.90	3.757	1.828	1.219	0.916	0.733	2.554
1.00	4.719	2.334	1.564	1.177	0.944	3.055
$R_i / t = 10$						
$l_m / \pi R_m$	f_0^A	f_1^A	f_2^A	f_3^A	f_4^A	f_{bg}^A
0.03	1.013	0.096	-0.002	-0.030	-0.038	0.930
0.06	0.972	0.128	0.013	-0.021	-0.036	0.891
0.10	0.958	0.167	0.043	0.003	-0.014	0.877
0.20	1.052	0.295	0.145	0.087	0.058	0.957
0.30	1.276	0.461	0.269	0.186	0.140	1.143
0.40	1.583	0.649	0.403	0.290	0.226	1.384
0.50	1.953	0.858	0.548	0.402	0.316	1.657
0.60	2.385	1.091	0.708	0.523	0.415	1.952
0.70	2.900	1.363	0.894	0.664	0.528	2.278
0.80	3.527	1.690	1.115	0.832	0.663	2.648
0.90	4.328	2.105	1.396	1.044	0.834	3.094
1.00	5.377	2.644	1.760	1.319	1.055	3.650

Table K21-2. Geometry functions for a circumferential through-thickness crack in a cylinder — intersection of crack with free surface at $u = 0$ ($R_i / t = 20, 50$).

$R_i / t = 20$						
$l_m / \pi R_m$	f_0^A	f_1^A	f_2^A	f_3^A	f_4^A	f_{bg}^A
0.015	1.026	0.095	-0.003	-0.028	-0.038	0.984
0.03	0.986	0.121	0.005	-0.037	-0.033	0.944
0.06	0.952	0.155	0.027	-0.013	-0.024	0.907
0.10	0.958	0.206	0.069	0.022	0.001	0.912
0.20	1.159	0.390	0.213	0.140	0.101	1.095
0.30	1.503	0.607	0.370	0.263	0.203	1.394
0.40	1.900	0.831	0.526	0.383	0.300	1.720
0.50	2.332	1.063	0.685	0.504	0.398	2.047
0.60	2.805	1.312	0.854	0.632	0.501	2.372
0.70	3.369	1.605	1.052	0.782	0.622	2.730
0.80	4.052	1.955	1.289	0.960	0.765	3.131
0.90	4.944	2.411	1.595	1.191	0.950	3.631
1.00	6.104	3.000	1.990	1.489	1.189	4.250
$R_i / t = 50$						
$l_m / \pi R_m$	f_0^A	f_1^A	f_2^A	f_3^A	f_4^A	f_{bg}^A
0.010	1.006	0.113	-0.000	-0.036	-0.044	0.991
0.025	1.046	0.165	0.019	-0.033	-0.056	1.026
0.05	0.944	0.178	0.037	-0.013	-0.018	0.922
0.10	1.018	0.280	0.119	0.057	0.019	0.991
0.20	1.465	0.586	0.349	0.242	0.183	1.415
0.30	1.983	0.880	0.556	0.404	0.316	1.883
0.40	2.452	1.131	0.729	0.536	0.423	2.271
0.50	2.926	1.380	0.898	0.665	0.527	2.622
0.60	3.435	1.643	1.076	0.799	0.635	2.959
0.70	4.079	1.973	1.298	0.966	0.769	3.359
0.80	4.856	2.367	1.562	1.165	0.928	3.805
0.90	5.910	2.899	1.919	1.433	1.143	4.394
1.00	7.270	3.582	2.375	1.775	1.416	5.120

Table K21-3. Geometry functions for a circumferential through-thickness crack in a cylinder — intersection of crack with free surface at $u = 0$ ($R_i / t = 100$).

$R_i / t = 100$						
$l_m / \pi R_m$	f_0^A	f_1^A	f_2^A	f_3^A	f_4^A	f_{bg}^A
0.006	0.933	0.107	0.004	-0.032	-0.040	0.928
0.015	0.949	0.147	0.020	-0.018	-0.036	0.944
0.03	0.932	0.193	0.060	0.015	-0.004	0.925
0.06	0.967	0.278	0.133	0.077	0.049	0.959
0.10	1.159	0.427	0.247	0.168	0.126	1.146
0.20	1.827	0.814	0.518	0.378	0.297	1.785
0.30	2.348	1.099	0.715	0.529	0.419	2.252
0.40	2.788	1.328	0.870	0.646	0.513	2.603
0.50	3.291	1.587	1.045	0.778	0.619	2.968
0.60	3.833	1.862	1.229	0.916	0.729	3.316
0.70	4.548	2.224	1.471	1.098	0.875	3.755
0.80	5.390	2.645	1.751	1.308	1.042	4.228
0.90	6.620	3.262	2.163	1.616	1.289	4.922
1.00	8.185	4.037	2.677	2.000	1.594	5.762

Table K22-1. Geometry functions for a circumferential through-thickness crack in a cylinder — intersection of crack with free surface at $u = t$ ($R_i / t = 5, 10$).

$R_i / t = 5$						
$l_m / \pi R_m$	f_0^B	f_1^B	f_2^B	f_3^B	f_4^B	f_{bg}^B
0.06	1.108	0.984	0.883	0.813	0.767	1.085
0.10	1.130	0.956	0.834	0.752	0.695	1.095
0.20	1.239	0.950	0.791	0.692	0.624	1.163
0.30	1.351	0.962	0.776	0.665	0.591	1.222
0.40	1.459	0.984	0.774	0.653	0.574	1.262
0.50	1.573	1.017	0.785	0.654	0.570	1.291
0.60	1.705	1.066	0.810	0.668	0.577	1.317
0.70	1.867	1.136	0.850	0.694	0.596	1.349
0.80	2.074	1.232	0.911	0.737	0.627	1.393
0.90	2.341	1.362	0.994	0.798	0.675	1.458
1.00	2.690	1.536	1.109	0.882	0.741	1.555
$R_i / t = 10$						
$l_m / \pi R_m$	f_0^B	f_1^B	f_2^B	f_3^B	f_4^B	f_{bg}^B
0.03	1.080	0.974	0.878	0.810	0.763	1.068
0.06	1.091	0.934	0.813	0.732	0.673	1.075
0.10	1.144	0.924	0.781	0.689	0.625	1.120
0.20	1.288	0.929	0.749	0.640	0.568	1.229
0.30	1.404	0.941	0.735	0.616	0.539	1.298
0.40	1.508	0.961	0.734	0.607	0.526	1.338
0.50	1.620	0.996	0.748	0.612	0.525	1.368
0.60	1.759	1.052	0.778	0.631	0.538	1.401
0.70	1.937	1.131	0.827	0.664	0.562	1.446
0.80	2.171	1.241	0.897	0.714	0.601	1.513
0.90	2.473	1.387	0.992	0.784	0.655	1.606
1.00	2.868	1.582	1.120	0.879	0.730	1.738

Table K22-2. Geometry functions for a circumferential through-thickness crack in a cylinder — intersection of crack with free surface at $u = t$ ($R_i / t = 20, 50$).

$R_i / t = 20$						
$l_m / \pi R_m$	f_0^B	f_1^B	f_2^B	f_3^B	f_4^B	f_{bg}^B
0.015	1.063	0.967	0.874	0.809	0.762	1.056
0.03	1.059	0.924	0.808	0.727	0.675	1.051
0.06	1.101	0.903	0.763	0.672	0.610	1.093
0.10	1.180	0.904	0.742	0.640	0.571	1.165
0.20	1.344	0.913	0.714	0.598	0.522	1.298
0.30	1.456	0.924	0.702	0.577	0.498	1.365
0.40	1.558	0.948	0.707	0.574	0.491	1.404
0.50	1.681	0.993	0.729	0.587	0.498	1.444
0.60	1.847	1.065	0.771	0.615	0.518	1.500
0.70	2.063	1.164	0.834	0.660	0.552	1.576
0.80	2.346	1.299	0.921	0.723	0.602	1.681
0.90	2.707	1.475	1.036	0.808	0.668	1.818
1.00	3.180	1.708	1.189	0.922	0.759	2.004
$R_i / t = 50$						
$l_m / \pi R_m$	f_0^B	f_1^B	f_2^B	f_3^B	f_4^B	f_{bg}^B
0.010	1.035	0.924	0.818	0.743	0.691	1.030
0.025	1.165	0.967	0.816	0.713	0.642	1.163
0.05	1.126	0.885	0.727	0.625	0.558	1.126
0.10	1.273	0.898	0.707	0.593	0.516	1.265
0.20	1.434	0.907	0.685	0.560	0.480	1.397
0.30	1.529	0.920	0.679	0.547	0.464	1.448
0.40	1.641	0.956	0.694	0.554	0.466	1.495
0.50	1.795	1.020	0.731	0.579	0.484	1.559
0.60	2.002	1.114	0.790	0.620	0.516	1.649
0.70	2.261	1.236	0.869	0.677	0.560	1.757
0.80	2.601	1.400	0.975	0.756	0.622	1.903
0.90	3.031	1.611	1.114	0.859	0.703	2.084
1.00	3.604	1.893	1.300	0.997	0.813	2.334

Table K22-3. Geometry functions for a circumferential through-thickness crack in a cylinder — intersection of crack with free surface at $u = t$ ($R_i / t = 100$).

$R_i / t = 100$						
$l_m / \pi R_m$	f_0^B	f_1^B	f_2^B	f_3^B	f_4^B	f_{bg}^B
0.006	0.951	0.845	0.746	0.675	0.628	0.947
0.015	1.015	0.851	0.720	0.632	0.569	1.011
0.03	1.082	0.837	0.684	0.586	0.519	1.077
0.06	1.219	0.850	0.667	0.556	0.483	1.211
0.10	1.327	0.855	0.649	0.531	0.454	1.314
0.20	1.407	0.833	0.610	0.488	0.411	1.370
0.30	1.457	0.828	0.593	0.469	0.391	1.378
0.40	1.608	0.891	0.631	0.494	0.409	1.464
0.50	1.767	0.962	0.674	0.524	0.432	1.537
0.60	1.997	1.070	0.744	0.575	0.471	1.650
0.70	2.261	1.197	0.825	0.635	0.518	1.764
0.80	2.613	1.368	0.937	0.717	0.583	1.924
0.90	3.082	1.598	1.089	0.830	0.673	2.139
1.00	3.714	1.908	1.293	0.982	0.793	2.434

K4. Cracks in a sphere

K4.1 Through-thickness crack

K_I is given by

$$K_I = \sqrt{\pi l/2}\left[\sigma_m f_m\left(l/t, R_i/t\right) + \sigma_b f_b\left(l/t, R_i/t\right)\right] \quad , \tag{K24}$$

where σ_m and σ_b are the membrane and through-thickness bending stress components, respectively, which define the axisymmetrical stress state σ according to

$$\sigma = \sigma(u) = \sigma_m + \sigma_b\left(1 - \frac{2u}{t}\right) \qquad \text{for } 0 \le u \le t \quad . \tag{K25}$$

σ is to be taken normal to the prospective crack plane in an uncracked sphere. σ_m and σ_b are determined by fitting σ to Eq. (K25). The coordinate u is defined in Fig. G4.1.

The geometry functions f_m and f_b are given in Table K23 for the intersections of the crack with the free surface at $u = 0$ (f^A) and at $u = t$ (f^B), respectively. See Fig. G4.1.

Ref.: [K9].

Table K23. Geometry functions for a through-thickness crack in a sphere.

	$R_i / t = 10$				$R_i / t = 20$			
l/t	f_m^A	f_b^A	f_m^B	f_b^B	f_m^A	f_b^A	f_m^B	f_b^B
0	1.000	1.000	1.000	-1.000	1.000	1.000	1.000	-1.000
2	0.919	0.993	1.240	-1.031	0.941	0.995	1.144	-1.020
4	0.894	0.993	1.637	-1.074	0.897	0.992	1.401	-1.050
6	0.944	0.997	2.083	-1.111	0.895	0.993	1.700	-1.080
8	1.059	1.003	2.549	-1.143	0.932	0.996	2.020	-1.106
10	1.231	1.011	3.016	-1.170	1.003	1.001	2.351	-1.130
15	1.915	1.031	4.124	-1.226	1.309	1.014	3.186	-1.180
20	2.968	1.050	5.084	-1.272	1.799	1.028	3.981	-1.219

K5. Cracks in a bar

K5.1 Part circumferential surface crack

K_{I} is given by

$$K_{\mathrm{I}} = \sqrt{\pi a}\left[\sigma_m f_m\left(a/R, a/b\right) + \sigma_b f_b\left(a/R, a/b\right)\right] \quad , \tag{K26}$$

where σ_m and σ_b are the membrane and through-thickness bending stress components, respectively, which define the stress state σ at the central line of the bar according to

$$\sigma = \sigma(u) = \sigma_m + \sigma_b\left(1 - \frac{u}{R}\right) \qquad \text{for } 0 \le u \le 2R \quad . \tag{K27}$$

σ is to be taken normal to the prospective crack plane in an uncracked bar. σ_m and σ_b are determined by fitting σ to Eq. (K27). The coordinate *u* is defined in Fig. G5.1.

The geometry functions f_m and f_b are given in Table K24 for the deepest point (f^A) and the intersections of the crack with the free surface (f^B), respectively. See Fig. G5.1.

Ref.: Based on a polynomial fit of the results given in [K10] and [K11].

Table K24-1. Geometry function f_m^A for a surface crack in a round bar at the deepest point.

a/b	$a/R=0.1$	$a/R=0.2$	$a/R=0.4$	$a/R=0.6$	$a/R=0.8$	$a/R=1.0$
0.0	1.0501	1.0698	1.1803	1.4217	1.8490	2.5990
0.2	0.9859	1.0123	1.1225	1.3542	1.7645	2.4871
0.4	0.9126	0.9423	1.0460	1.2575	1.6318	2.2918
0.6	0.8303	0.8599	0.9506	1.1314	1.4510	2.0133
0.8	0.7388	0.7651	0.8365	0.9761	1.2221	1.6514
1.0	0.6383	0.6578	0.7036	0.7915	0.9450	1.2062

Table K24-2. Geometry function f_b^A for a surface crack in a round bar at the deepest point.

a/b	$a/R=0.1$	$a/R=0.2$	$a/R=0.4$	$a/R=0.6$	$a/R=0.8$	$a/R=1.0$
0.0	0.9811	0.9323	0.8821	0.9060	1.0026	1.2070
0.2	0.9214	0.8825	0.8401	0.8653	0.9610	1.1611
0.4	0.8527	0.8209	0.7822	0.8029	0.8886	1.0702
0.6	0.7748	0.7474	0.7082	0.7188	0.7855	0.9343
0.8	0.6879	0.6622	0.6182	0.6130	0.6516	0.7535
1.0	0.5918	0.5652	0.5123	0.4855	0.4869	0.5277

Table K24-3. Geometry function f_m^B for a surface crack in a round bar at the intersections of the crack with the free surface.

a/b	$a/R=0.1$	$a/R=0.2$	$a/R=0.4$	$a/R=0.6$	$a/R=0.8$	$a/R=1.0$
0.0	0.3140	0.4090	0.5991	0.9318	1.2645	2.0131
0.2	0.4647	0.5454	0.7067	1.0541	1.4015	2.1863
0.4	0.5810	0.6530	0.7969	1.1480	1.4992	2.3037
0.6	0.6629	0.7318	0.8696	1.2136	1.5576	2.3652
0.8	0.7102	0.7818	0.9249	1.2508	1.5768	2.3709
1.0	0.7231	0.8030	0.9627	1.2597	1.5567	2.3207

Table K24-4. Geometry function f_b^B for a surface crack in a round bar at the intersections of the crack with the free surface.

a/b	$a/R=0.1$	$a/R=0.2$	$a/R=0.4$	$a/R=0.6$	$a/R=0.8$	$a/R=1.0$
0.0	0.3095	0.3390	0.3981	0.5116	0.6252	0.8361
0.2	0.4616	0.4834	0.5269	0.6291	0.7313	0.9657
0.4	0.5809	0.5990	0.6351	0.7332	0.8312	1.0811
0.6	0.6674	0.6858	0.7226	0.8239	0.9251	1.1822
0.8	0.7209	0.7438	0.7895	0.9012	1.0128	1.2691
1.0	0.7416	0.7730	0.8357	0.9651	1.0945	1.3417

K5. References

[K1] FETT T., MUNZ D., and J. NEUMANN, (1990), ”Local stress intensity factors for surface cracks in plates under power-shaped stress distributions”, *Engineering Fracture Mechanics*, Vol. 36, No. 4, pp 647-651.

[K2] CHAPULIOT, S., LACIRE,. M. H., and DELLIOU, P. Le., (1998), ”Stress intensity factors for internal circumferential cracks in tubes over a wide range of radius over thickness ratio”, *ASME PVP*, Vol. 365, pp 95-106.

[K3] WU X. R., and A. J. CARLSSON, (1991), *Weight functions and stress intensity factor solutions*, Pergamon Press, Oxford, U.K.

[K4] ZVEZDIN Y. I. et. al, (1990), ”Handbook - Stress intensity and reduction factors calculation”, MR 125-01-90, Central Research Institute for Technology of Machinery, Moscow, Russia.

[K5] SIH, G. C., PARIS, P. F., and F. ERDOGAN, (1962), ”Stress intensity factors for plane extension and plate bending problems”, *Journal of Applied Mechanics*, Vol. 29, pp. 306-312.

[K6] RAJU, I. S., and J. C. NEWMAN, (1978), ”Stress intensity factor influence coefficients for internal and external surface cracks in cylindrical vessels”, *ASME PVP*, Vol. 58, pp. 37-48.

[K7] ZANG, W., (1997), ”Stress intensity factor solutions for axial and circumferential trough-wall cracks in cylinders”, SINTAP/SAQ/02, SAQ Control AB, Stockholm, Sweden.

[K8] BERGMAN, M., (1995), ”Stress intensity factors for circumferential surface cracks in pipes”, *Fatigue & Fracture of Engineering Materials & Structures*, Vol. 18, No. 10, pp. 1155-1172.

[K9] ERDOGAN, F., and J. J. KIBLER, (1969), ”Cylindrical and spherical shells with cracks”, *International Journal of Fracture Mechanics*, Vol. 5, pp.229-237.

[K10] CORUNOEAU, N., and J. ROYER, (1998), “Simplified model for the fatigue growth analysis of surface cracks in round bars under mode I”, *International Journal of Fatigue*, Vol. 20, pp. 711-718.

[K11] KLASÉN, B., DILLSTRÖM, P., and W. ZANG., (2003), “Stress Intensity Factor and Limit Load Solutions for Surface Cracks in Round Bars”, RSE R&D Report No. 2001/04, Rev. 1, Det Norske Veritas AB.

APPENDIX L. LIMIT LOAD SOLUTIONS

L1. Cracks in a plate

L1.1 Finite surface crack

L_r is given by

$$L_r = \frac{(1-\zeta)^{1.58}\frac{\sigma_b}{3} + \sqrt{(1-\zeta)^{3.16}\frac{\sigma_b^2}{9} + (1-\zeta)^{3.14}\sigma_m^2}}{(1-\zeta)^2\sigma_Y} \quad , \tag{L1}$$

where

$$\zeta = \frac{al}{t(l+2t)} \tag{L2}$$

See Fig. G1.1. σ_m and σ_b are the membrane and bending stress components, respectively, which define the stress state σ according to

$$\sigma = \sigma(u) = \sigma_m + \sigma_b\left(1 - \frac{2u}{t}\right) \quad \text{for } 0 \le u \le t\,. \tag{L3}$$

σ is to be taken normal to the prospective crack plane in an uncracked plate. σ_m and σ_b are determined by fitting σ to Eq. (L3). The coordinate u is defined in Fig. G1.1.

Remarks: The solution is limited to $a/t \le 0.8$. Also, the plate should be large in comparison to the length of the crack so that edge effects do not influence.

Ref: [L1].

L1.2 Infinite surface crack

L_r is given by

$$L_r = \frac{\zeta\sigma_m + \frac{\sigma_b}{3} + \sqrt{\left(\zeta\sigma_m + \frac{\sigma_b}{3}\right)^2 + (1-\zeta)^2\sigma_m^2}}{(1-\zeta)^2\sigma_Y} \quad , \tag{L4}$$

where

$$\zeta = \frac{a}{t}. \tag{L5}$$

See Fig. G1.2. σ_m and σ_b are the membrane and bending stress components, respectively, which define the stress state σ according to

$$\sigma = \sigma(u) = \sigma_m + \sigma_b\left(1 - \frac{2u}{t}\right) \quad \text{for } 0 \le u \le t\,. \tag{L6}$$

σ is to be taken normal to the prospective crack plane in an uncracked plate. σ_m and σ_b are determined by fitting σ to Eq. (L6). The coordinate u is defined in Fig. G1.2.

Remarks: The solution is limited to $a/t \le 0.8$. Also, the plate should be large in the transverse direction to the crack so that edge effects do not influence.

Ref: [L2].

L1.3 Embedded crack

L_r is given by

$$L_r = \frac{\zeta\sigma_m + \frac{\sigma_b}{3} + \sqrt{\left(\zeta\sigma_m + \frac{\sigma_b}{3}\right)^2 + \left[(1-\zeta)^2 + 4\zeta\gamma\right]\sigma_m^2}}{\left[(1-\zeta)^2 + 4\zeta\gamma\right]\sigma_Y} \quad , \tag{L7}$$

where

$$\zeta = \frac{2al}{t(l+2t)} \quad , \tag{L8}$$

$$\gamma = \frac{1}{2} - \frac{a}{t} - \frac{e}{t} . \tag{L9}$$

See Fig. G1.3. σ_m and σ_b are the membrane and bending stress components, respectively, which define the stress state σ according to

$$\sigma = \sigma(u) = \sigma_m + \sigma_b\left(1 - \frac{2u}{t}\right) \quad \text{for } 0 \le u \le t . \tag{L10}$$

σ is to be taken normal to the prospective crack plane in an uncracked plate. σ_m and σ_b are determined by fitting σ to Eq. (L10). The coordinate u is defined in Fig. G1.3.

Remarks: The solution is limited to $a/t \le 0.8$ and $e/t \ge 0$. Also, the plate should be large in comparison to the length of the crack so that edge effects do not influence.

Ref: [L2].

L1.4 Through-thickness crack

L_r is given by

$$L_r = \frac{\frac{\sigma_b}{3} + \sqrt{\frac{\sigma_b^2}{9} + \sigma_m^2}}{\sigma_Y}. \qquad \text{(L11)}$$

See Fig. G1.4. σ_m and σ_b are the membrane and bending stress components, respectively, which define the stress state σ according to

$$\sigma = \sigma(u) = \sigma_m + \sigma_b \left(1 - \frac{2u}{t}\right) \quad \text{for } 0 \le u \le t. \qquad \text{(L12)}$$

σ is to be taken normal to the prospective crack plane in an uncracked plate. σ_m and σ_b are determined by fitting σ to Eq. (L12). The coordinate u is defined in Fig. G1.4.

Remark: The plate should be large in comparison to the length of the crack so that edge effects do not influence.

L2. Axial cracks in a cylinder

L2.1 Finite internal surface crack

L_r is given by

$$L_r = \frac{1}{\sqrt{\left(1-\zeta^{3.11}\right)^{1.9}}}\frac{\sigma_m}{\sigma_Y} \tag{L13}$$

where

$$\zeta = \frac{al}{t(l+2t)}. \tag{L14}$$

See Fig. G2.1. σ_m is the membrane stress component, which define the stress state σ according to

$$\sigma = \sigma(u) = \sigma_m \qquad \text{for } 0 \le u \le t. \tag{L15}$$

σ is to be taken normal to the prospective crack plane in an uncracked cylinder. σ_m is determined by fitting σ to Eq. (L15). The coordinate u is defined in Fig. G2.1.

Remarks: The solution is limited to $a/t \le 0.8$. Also, the cylinder should be long in comparison to the length of the crack so that edge effects do not influence.

Ref: [L1].

L2.2 Infinite internal surface crack

L_r is given by

$$L_r = \frac{\zeta\sigma_m + \frac{\sigma_b}{3} + \sqrt{\left(\zeta\sigma_m + \frac{\sigma_b}{3}\right)^2 + (1-\zeta)^2\sigma_m^2}}{(1-\zeta)^2\sigma_Y} \quad , \tag{L16}$$

where

$$\zeta = \frac{a}{t}. \tag{L17}$$

See Fig. G2.2. σ_m and σ_b are the membrane and bending stress components, respectively, which define the stress state σ according to

$$\sigma = \sigma(u) = \sigma_m + \sigma_b\left(1 - \frac{2u}{t}\right) \quad \text{for } 0 \le u \le t\,. \tag{L18}$$

σ is to be taken normal to the prospective crack plane in an uncracked cylinder. σ_m and σ_b are determined by fitting σ to Eq. (L18). The coordinate u is defined in Fig. G2.2.

Remark: The solution is limited to $a/t \le 0.8$.

Ref: [L2].

L2.3 Finite external surface crack

L_r is given by

$$L_r = \frac{1}{\sqrt{\left(1-\zeta^{3.11}\right)^{1.9}}}\frac{\sigma_m}{\sigma_Y} \tag{L19}$$

where

$$\zeta = \frac{al}{t(l+2t)}. \tag{L20}$$

See Fig. G2.3. σ_m is the membrane stress component, which define the stress state σ according to

$$\sigma = \sigma(u) = \sigma_m \qquad \text{for } 0 \le u \le t. \tag{L21}$$

σ is to be taken normal to the prospective crack plane in an uncracked cylinder. σ_m is determined by fitting σ to Eq. (L21). The coordinate u is defined in Fig. G2.3.

Remarks: The solution is limited to $a/t \le 0.8$. Also, the cylinder should be long in comparison to the length of the crack so that edge effects do not influence.

Ref: [L1].

L2.4 Infinite external surface crack

L_r is given by

$$L_r = \frac{\zeta\sigma_m + \frac{\sigma_b}{3} + \sqrt{\left(\zeta\sigma_m + \frac{\sigma_b}{3}\right)^2 + (1-\zeta)^2\sigma_m^2}}{(1-\zeta)^2\sigma_Y} \quad , \tag{L22}$$

where

$$\zeta = \frac{a}{t}. \tag{L23}$$

See Fig. G2.4. σ_m and σ_b are the membrane and bending stress components, respectively, which define the stress state σ according to

$$\sigma = \sigma(u) = \sigma_m + \sigma_b\left(1 - \frac{2u}{t}\right) \quad \text{for } 0 \le u \le t\,. \tag{L24}$$

σ is to be taken normal to the prospective crack plane in an uncracked cylinder. σ_m and σ_b are determined by fitting σ to Eq. (L24). The coordinate u is defined in Fig. G2.4.

Remark: The solution is limited to $a/t \le 0.8$.

Ref: [L2].

L2.5 Through-thickness crack

L_r is given by

$$L_r = \frac{\sigma_m}{\sigma_Y}\sqrt{1+1.05\lambda^2} \quad , \tag{L25}$$

where

$$\lambda = \frac{l}{2\sqrt{R_i t}} . \tag{L26}$$

See Fig. G2.5. σ_m is the membrane stress component, which defines the stress state σ according to

$$\sigma = \sigma(u) = \sigma_m \qquad \text{for } 0 \le u \le t . \tag{L27}$$

σ is to be taken normal to the prospective crack plane in an uncracked cylinder. σ_m is determined by fitting σ to Eq. (L27). The coordinate *u* is defined in Fig. G2.5.

Remarks: The cylinder should be long in comparison to the length of the crack so that edge effects do not influence.

Ref: [L3].

L3. Circumferential cracks in a cylinder

L3.1 Part circumferential internal surface crack

L_r is given by

$$L_r = \sqrt{\frac{\left(\frac{\sigma_m}{s'_m}\right)^2 + \left(\frac{\sigma_{bg}}{s'_{bg}}\right)^2}{\left(\frac{s_m}{s'_m}\right)^2 + \left(\frac{s_{bg}}{s'_{bg}}\right)^2}} \quad , \tag{L28}$$

where the parameters s_m, s'_m, s_{bg} and s'_{bg} are obtained by solving the equation system

$$\begin{cases} \dfrac{s_m}{\sigma_Y} = 1 - 2\dfrac{\beta}{\pi} - \dfrac{a}{t}\dfrac{\alpha}{\pi} \\ \dfrac{s_{bg}}{\sigma_Y} = \dfrac{4}{\pi}\sin\beta - \dfrac{2}{\pi}\dfrac{a}{t}\sin\alpha \\ \theta = \dfrac{l}{2R_i} \\ \alpha = \begin{cases} \theta & \text{if } \theta \le \pi - \beta \\ \pi - \beta & \text{if } \theta > \pi - \beta \end{cases} \\ \sigma_m s_{bg} - \sigma_{bg} s_m = 0 \\ s'_m = s_m \qquad \text{for } s_{bg} = 0 \\ s'_{bg} = s_{bg} \qquad \text{for } s_m = 0 \end{cases} . \tag{L29}$$

See Fig. G3.1. σ_m and σ_{bg} are the membrane and global bending stress components, respectively. σ_m defines the axisymmetrical stress state σ according to

$$\sigma = \sigma(u) = \sigma_m \qquad \text{for } 0 \le u \le t\,. \tag{L30}$$

σ is to be taken normal to the prospective crack plane in an uncracked cylinder. σ_m is determined by fitting σ to Eq. (L30). The coordinate u is defined in Fig. G3.1.

Remarks: The cylinder should be thin-walled. Also, the cylinder should be long in the transverse direction to the crack so that edge effects do not influence.

Ref: [L4].

L3.2 Complete circumferential internal surface crack

L_r is given by

$$L_r = \sqrt{\frac{\left(\frac{\sigma_m}{s'_m}\right)^2 + \left(\frac{\sigma_{bg}}{s'_{bg}}\right)^2}{\left(\frac{s_m}{s'_m}\right)^2 + \left(\frac{s_{bg}}{s'_{bg}}\right)^2}} \quad , \tag{L31}$$

where the parameters s_m, s'_m, s_{bg} and s'_{bg} are obtained by solving the equation system

$$\begin{cases} \dfrac{s_m}{\sigma_Y} = 1 - 2\dfrac{\beta}{\pi} - \dfrac{a}{t}\dfrac{\pi - \beta}{\pi} \\ \dfrac{s_{bg}}{\sigma_Y} = \dfrac{2}{\pi}\dfrac{2t-a}{t}\sin\beta \\ \sigma_m s_{bg} - \sigma_{bg} s_m = 0 \\ s'_m = s_m \qquad \text{for } s_{bg} = 0 \\ s'_{bg} = s_{bg} \qquad \text{for } s_m = 0 \end{cases} . \tag{L32}$$

See Fig. G3.2. σ_m and σ_{bg} are the membrane and global bending stress components, respectively. σ_m defines the axisymmetrical stress state σ according to

$$\sigma = \sigma(u) = \sigma_m \qquad \text{for } 0 \le u \le t \, . \tag{L33}$$

σ is to be taken normal to the prospective crack plane in an uncracked cylinder. σ_m is determined by fitting σ to Eq. (L33). The coordinate *u* is defined in Fig. G3.2.

Remarks: The cylinder should be thin-walled. Also, the cylinder should be long in the transverse direction to the crack so that edge effects do not influence.

Ref: [L4].

L3.3 Part circumferential external surface crack

L_r is given by

$$L_r = \sqrt{\frac{\left(\frac{\sigma_m}{s'_m}\right)^2 + \left(\frac{\sigma_{bg}}{s'_{bg}}\right)^2}{\left(\frac{s_m}{s'_m}\right)^2 + \left(\frac{s_{bg}}{s'_{bg}}\right)^2}} \quad , \tag{L34}$$

where the parameters s_m, s'_m, s_{bg} and s'_{bg} are obtained by solving the equation system

$$\begin{cases} \dfrac{s_m}{\sigma_Y} = 1 - 2\dfrac{\beta}{\pi} - \dfrac{a}{t}\dfrac{\alpha}{\pi} \\ \dfrac{s_{bg}}{\sigma_Y} = \dfrac{4}{\pi}\sin\beta - \dfrac{2}{\pi}\dfrac{a}{t}\sin\alpha \\ \theta = \dfrac{l}{2(R_i + t)} \\ \alpha = \begin{cases} \theta & \text{if } \theta \le \pi - \beta \\ \pi - \beta & \text{if } \theta > \pi - \beta \end{cases} \\ \sigma_m s_{bg} - \sigma_{bg} s_m = 0 \\ s'_m = s_m \qquad \text{for } s_{bg} = 0 \\ s'_{bg} = s_{bg} \qquad \text{for } s_m = 0 \end{cases} . \tag{L35}$$

See Fig. G3.3. σ_m and σ_{bg} are the membrane and global bending stress components, respectively. σ_m defines the axisymmetrical stress state σ according to

$$\sigma = \sigma(u) = \sigma_m \qquad \text{for } 0 \le u \le t\,. \tag{L36}$$

σ is to be taken normal to the prospective crack plane in an uncracked cylinder. σ_m is determined by fitting σ to Eq. (L36). The coordinate *u* is defined in Fig. G3.3.

Remarks: The cylinder should be thin-walled. Also, the cylinder should be long in the transverse direction to the crack so that edge effects do not influence.

Ref: [L4].

L3.4 Complete circumferential external surface crack

L_r is given by

$$L_r = \sqrt{\frac{\left(\frac{\sigma_m}{s'_m}\right)^2 + \left(\frac{\sigma_{bg}}{s'_{bg}}\right)^2}{\left(\frac{s_m}{s'_m}\right)^2 + \left(\frac{s_{bg}}{s'_{bg}}\right)^2}} \quad , \tag{L37}$$

where the parameters s_m, s'_m, s_{bg} and s'_{bg} are obtained by solving the equation system

$$\begin{cases} \dfrac{s_m}{\sigma_Y} = 1 - 2\dfrac{\beta}{\pi} - \dfrac{a}{t}\dfrac{\pi - \beta}{\pi} \\ \dfrac{s_{bg}}{\sigma_Y} = \dfrac{2}{\pi}\dfrac{2t-a}{t}\sin\beta \\ \sigma_m s_{bg} - \sigma_{bg} s_m = 0 \\ s'_m = s_m \qquad \text{for } s_{bg} = 0 \\ s'_{bg} = s_{bg} \qquad \text{for } s_m = 0 \end{cases} . \tag{L38}$$

See Fig. G3.4. σ_m and σ_{bg} are the membrane and global bending stress components, respectively. σ_m defines the axisymmetrical stress state σ according to

$$\sigma = \sigma(u) = \sigma_m \qquad \text{for } 0 \le u \le t \, . \tag{L39}$$

σ is to be taken normal to the prospective crack plane in an uncracked cylinder. σ_m is determined by fitting σ to Eq. (L39). The coordinate *u* is defined in Fig. G3.4.

Remarks: The cylinder should be thin-walled. Also, the cylinder should be long in the transverse direction to the crack so that edge effects do not influence.

Ref: [L4].

L3.5 Through-thickness crack

L_r is given by

$$L_r = \sqrt{\frac{\left(\frac{\sigma_m}{s'_m}\right)^2 + \left(\frac{\sigma_{bg}}{s'_{bg}}\right)^2}{\left(\frac{s_m}{s'_m}\right)^2 + \left(\frac{s_{bg}}{s'_{bg}}\right)^2}} \quad , \tag{L40}$$

where the parameters s_m, s'_m, s_{bg} and s'_{bg} are obtained by solving the equation system

$$\begin{cases} \dfrac{s_m}{\sigma_Y} = 1 - 2\dfrac{\beta}{\pi} - \dfrac{\theta}{\pi} \\ \dfrac{s_{bg}}{\sigma_Y} = \dfrac{4}{\pi}\sin\beta - \dfrac{2}{\pi}\sin\theta \\ \theta = \dfrac{l}{2R_i} \\ \sigma_m s_{bg} - \sigma_{bg} s_m = 0 \\ s'_m = s_m \qquad \text{for } s_{bg} = 0 \\ s'_{bg} = s_{bg} \qquad \text{for } s_m = 0 \end{cases} . \tag{L41}$$

See Fig. G3.5. σ_m and σ_{bg} are the membrane and global bending stress components, respectively. σ_m defines the axisymmetrical stress state σ according to

$$\sigma = \sigma(u) = \sigma_m \qquad \text{for } 0 \le u \le t \, . \tag{L42}$$

σ is to be taken normal to the prospective crack plane in an uncracked cylinder. σ_m is determined by fitting σ to Eq. (L42). The coordinate *u* is defined in Fig. G3.5.

Remarks: The cylinder should be thin-walled. Also, the cylinder should be long in the transverse direction to the crack so that edge effects do not influence.

Ref: [L4].

L4. Cracks in a sphere

L4.1 Through-thickness crack

L_r is given by

$$L_r = \frac{\sigma_m}{\sigma_Y} \frac{1+\sqrt{1+8(\lambda/\cos\theta)^2}}{2} \quad , \tag{L43}$$

where

$$\lambda = \frac{l}{2\sqrt{R_i t}} \quad , \tag{L44}$$

$$\theta = \frac{l}{2R_i} . \tag{L45}$$

See Fig. G4.1. σ_m is the membrane stress component. σ_m defines the axisymmetrical stress state σ according to

$$\sigma = \sigma(u) = \sigma_m \qquad \text{for } 0 \le u \le t . \tag{L46}$$

σ is to be taken normal to the prospective crack plane in an uncracked sphere. σ_m is determined by fitting σ to Eq. (L46). The coordinate *u* is defined in Fig. G4.1.

Remark: The sphere should be thin-walled.

Ref: [L5].

L5. Cracks in a bar

L5.1 Part circumferential surface crack

L_r is given by

$$L_r = \frac{M_0}{M_{limit}} \quad , \tag{L47}$$

where M_0 is the applied bending moment on the bar and M_{limit} is obtained by solving the equation system

$$\begin{cases} N_{limit} = \sigma_Y R^2 \left(2 \cdot \phi + 2\cos(\phi)\sin(\phi) + \cos(\beta)\sin(\beta) + \beta - \frac{1}{2} \cdot \pi \right) \\ M_{limit} = \sigma_Y R^3 \left(\frac{4}{3}\cos(\phi)^3 - \frac{2}{3}\cos(\beta)^3 \right) \\ \frac{M_{limit}}{M_f} = \frac{M_0 / M_f}{N_0 / N_f} \cdot \frac{N_{limit}}{N_f} \end{cases} \tag{L48}$$

See Fig. G5.1. N_0 and M_0 are the applied tensile force and the applied bending moment on the bar, N_f is the pure tensile limit load and M_f is the pure bending limit load.

Ref.: [L6]

L5. References

[L1] DILLSTRÖM, P., and I. SATTARI-FAR., (2002), "Limit load solutions for surface cracks in plates and cylinders", RSE R&D Report No. 2002/01, Det Norske Veritas AB.

[L2] WILLOUGHBY, A. A., and T. G. DAVEY., (1989), "Plastic collapse in part-wall flaws in plates", *ASTM STP 1020*, American Society for Testing and Materials, Philadelphia, U.S.A., pp. 390-409.

[L3] KIEFNER, J. F., MAXEY, W. A., EIBER, R. J., and A. R. DUFFY, (1973), "Failure stress levels of flaws in pressurized cylinders", *ASTM STP 536*, American Society for Testing and Materials, Philadelphia, U.S.A., pp. 461-481.

[L4] DELFIN, P., (1996), "Limit load solutions for cylinders with circumferential cracks subjected to tension and bending", SAQ/FoU-Report 96/05, SAQ Kontroll AB, Stockholm, Sweden.

[L5] BURDEKIN, F. M., and T. E. TAYLOR, (1969), "Fracture in spherical vessels", *Journal of Mechanical Engineering and Science*, Vol. 11, pp. 486-497.

[L6] KLASÉN, B., DILLSTRÖM, P., and W. ZANG., (2003), "Stress Intensity Factor and Limit Load Solutions for Surface Cracks in Round Bars", RSE R&D Report No. 2001/04, Rev. 1, Det Norske Veritas AB.

APPENDIX M. MATERIAL DATA FOR NUCLEAR APPLICATIONS

In order to perform fracture mechanics assessments according to this handbook knowledge about yield strength σ_Y, ultimate tensile strength σ_U, critical stress intensity factor K_{cr} and J_r-curves is needed. In addition, crack growth calculations require knowledge about the growth rate per load cycle or per time unit for fatigue cracking and stress corrosion cracking, respectively. All material data should preferably be determined by testing of the material of the considered component in the environment and at the temperature for which the fracture assessment is to be performed. Below, some recommendations are given for steels and nickel base alloys common in nuclear applications. The data is intended for use in cases when test data for the actual materials are lacking. In many cases the data given below are conservative estimates.

M1. Yield strength, ultimate tensile strength

For many steels used in nuclear applications information about minimum levels of σ_Y and σ_U as functions of the temperature can be found in ASME Sect. III, Appendices. For other materials minimum levels are in general specified by the respective manufacturer. In cases where higher values than the specified can be verified, actual data may be used. In some cases, as for fracture assessments according to ASME Sect. XI, Appendix C, only minimum yield stress data are allowed.

M2. Fracture toughness and J_R-curves

In cases when the fracture toughness could not be directly determined, J_{Ic}–data converted according to Eq. (2.3), section 2.5 has been used. In this case an elastic modulus of 180000 MPa for stainless steels at 288 °C has been used and 195000 MPa for ferritic steels in materials on the upper shelf region. Poisson's ratio has been set to 0.3 in all cases except for nickel base alloys, where the Poisson's ratio was set to 0.29.

M2.1 Ferritic steel, plates, pressure vessels

For the materials SA-533 Grad B Class 1, SA-508 Class 2 and SA-508 Class 3 the fracture toughness K_{Ia} (conservative fracture toughness value at crack arrest) is given as a function of the difference between actual temperature T and the nil ductility transition temperature RT_{NDT} in ASME 1995, Sect.XI, Appendix A, Fig. A-4200-1. For the temperatures above the transition region higher values than 220MPa$\sqrt{\text{m}}$ are usually not assumed. This so called upper-shelf level is assumed to be reached for temperatures 102 °C above RT_{NDT}. Note that neutron irradiation can decrease this level and also increase RT_{NDT}. Fig. A-4200-1 corresponds to the analytic expression (T in °C)

$$K_{Ia} = 29.45 + 1.344 \exp\left[0.0261\left(T - RT_{NDT}\right) + 2.32\right] \quad \text{MPa}\sqrt{\text{m}} \tag{M1}$$

M2.2 Ferritic steel, pipes

The following data are taken from [M1]. They can be used in the absence of heat specific data. They are also referenced by ASME 1995, sect. XI, Appendix H and are intended for the following material categories:

Category 1: Seamless or welded carbon steel piping with a minimum yield strength lower than or equal to 276 MPa (base material) and welds with electrodes of type E7015, E7016 or E7018 (basic electrodes with a yield strength of the order of 500 MPa, Charpy-V toughness 27 J at –29 °C).

Category 2: All other welded ferritic piping with shielded metal arc welds (SMAW) or submerged arc welds (SAW) with minimum ultimate tensile strength lower than or equal to 522 MPa.

The table below differentiates between temperatures above or below the upper-shelf region. In addition, in [M1] it is distinguished between circumferential and axial cracks. The fracture properties are often worse for cracks oriented along the texture direction (axial cracks) than for cracks oriented across the texture direction (circumferential cracks). In the absence of heat specific data, the upper shelf temperature for class 1 ferritic piping steels can be taken as 93 °C.

Table M1. Fracture toughness data for carbon steel base metals and weldments, ref. [M1].

Material category	Temperature interval	Crack orientation	J_{Ic} (kJ/m^2)	K_{cr} (MPa$\sqrt{\text{m}}$)
1	$T \geq$ upper shelf	Circumferential	105	150
1	$T <$ upper shelf	Circumferential	7.9	42
2	$T \geq$ upper shelf	Circumferential	61.3	115
2	$T <$ upper shelf	Circumferential	7.9	42
1, 2	$T \geq$ upper shelf	Axial	52.5	106
1, 2	$T <$ upper shelf	Axial	7.9	42

M2.3 Austenitic stainless steel, pipes

The following data are mainly taken from ref. [M2], [M4] and [M5] at room temperature and 288 °C. Stainless steels base material is of type 304 or type 316, and the welding material is type 308. The different welding performances are shielded metal arc welds (SMAW), submerged arc welds (SAW) or gas tungsten arc welds (GTAW) which are the same as TIG-welding. The data are given in table M2.

Table M2. Fracture toughness data, J_{Ic}, for austenitic stainless steel 304, ref, [M2], [M4] and [M5]. The welding methods are shielded metal arc welds (SMAW), submerged arc welds (SAW) or gas tungsten arc welds (GTAW) which are same as TIG-welding.

Material type	Temperature °C	J_{Ic} (kJ/m^2)	K_{cr} (MPa$\sqrt{\text{m}}$)
Base material	25	1000	480
Base material	288	> 620	> 350
SMAW	25	259	239
SMAW	288	168	182
SAW	25	99	148
SAW	288	76	122
GTAW	25	500	339
GTAW	288	355	286

In general the fracture toughness for welded stainless steel, type 304, is depending on the welding performance method. The fracture toughness data for GTAW are better than for SMAW, and SMAW are better than for SAW. The high fracture toughness of GTAW welding material is due to advantageous microstructure during cooling after welding. In SAW welding silicon takes up from the fluxing material, forming equality inclusions distributed in the material, which acts as crack initiations points. In GTAW welding the material takes up only a small amount of silicon.

Fracture toughness data for GTAW-welds at 288 °C are only slightly below those of the base material. The heat affected zone (HAZ) and the base material have the same toughness. HAZ shows better properties than the weld material. The fracture toughness decreases with increasing temperature.

The standard test method ASTM E1820-01 [M3] is used to qualify the experimental data. A large number of experimental data points have been carried out for the tests, and the mean, lower and upper limits of J_{Ic} can be calculated. For gas tungsten arc welds (GTAW) and heat affected

zone (HAZ), the experimental data show a large scatter and only a few results were available. Thus the J_R-curve which forms the lowest experimental limit was provided. The J_R-curves for different welding performance are also given in Figures M1-M6.

The experimental J_R-curves for SAW welding performance are given in Figure M1 and M2. The statistical mean, lower and upper limits are also presented in the figures.

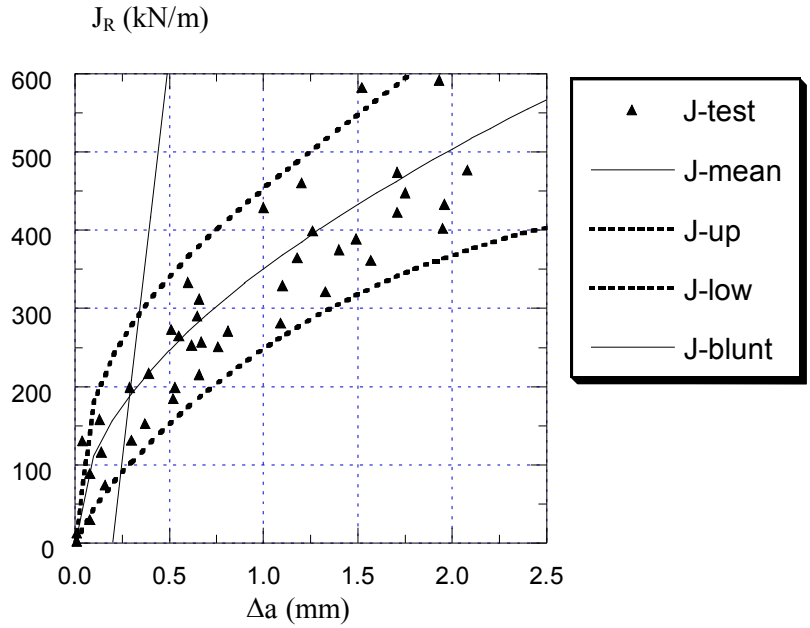

Figure M1. J_R-curves for SAW welding (304) at room temperature, ref. [M2]. The equation for J-mean is $J_R = 352.69(\Delta a)^{0.5086}$, J-upper is $J_R = 466.36(\Delta a)^{0.4361}$ and J-lower is $J_R = 235.49(\Delta a)^{0.6820}$.

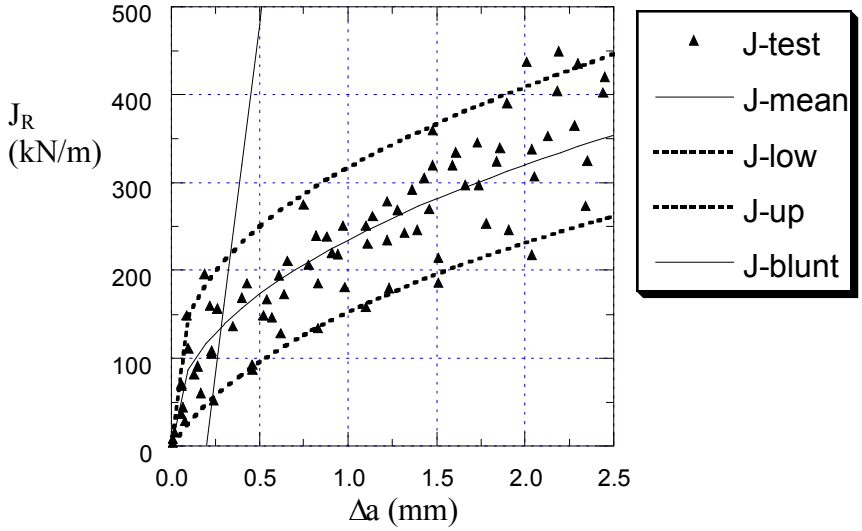

Figure M2. J_R-curves for SAW welding (304) at 288 °C, ref. [M2]. The equation for *J*-mean is $J_R = 235.65(\Delta a)^{0.4378}$, *J*-upper is $J_R = 320.07(\Delta a)^{0.3452}$ and *J*-lower is $J_R = 147.39(\Delta a)^{0.6838}$.

The experimental J_R-curves for SMAW welding at room temperature and at 288 °C are shown in Figure M3 and M4 respectively. The statistical mean, lower and upper limits are also presented in the figures. In lower limit 5 % of the data points are under the curve, and for upper limit 95 % of the data points are under the curve.

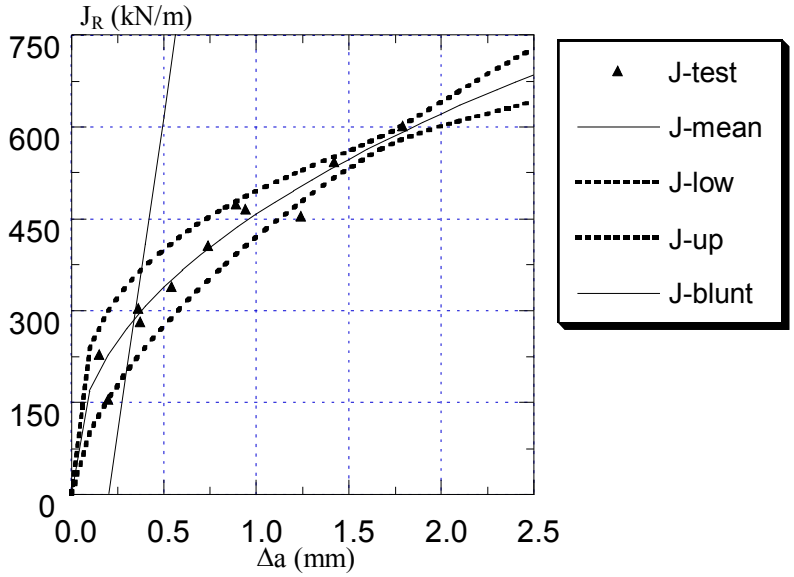

Figure M3. J_R-curves for SMAW welding (304) at room temperature, ref. [M2]. The equation for *J*-mean is $J_R = 458.87(\Delta a)^{0.4357}$, *J*-upper is $J_R = 504.91(\Delta a)^{0.3365}$ and *J*-lower is $J_R = 407.90(\Delta a)^{0.5794}$.

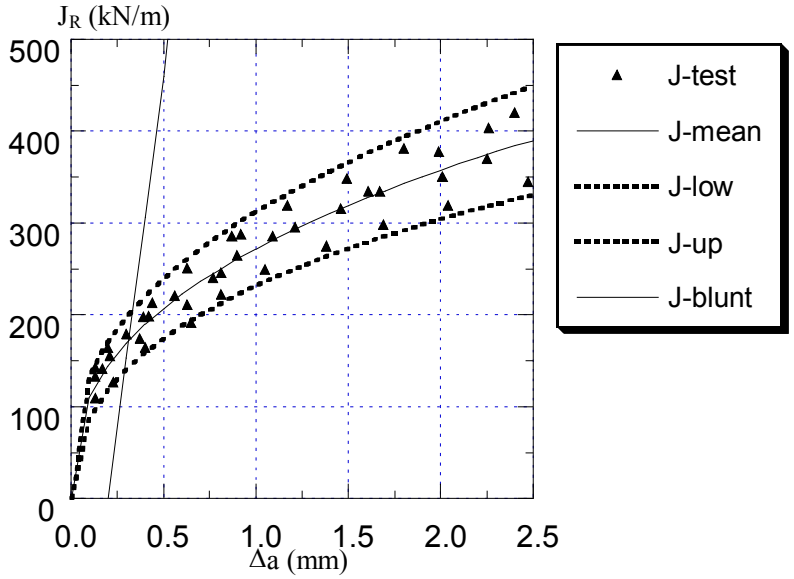

Figure M4. J_R-curves for SMAW welding (304) at 288 °C, ref. [M2]. The equation for *J*-mean is $J_R = 272.02(\Delta a)^{0.3939}$, *J*-upper is $J_R = 313.96(\Delta a)^{0.3824}$ and *J*-lower is $J_R = 230.03(\Delta a)^{0.4102}$.

The experimental J_R-curves for GTAW at room temperature and at 288 °C is shown in Figure M5 and M6 respectively. The statistical mean, lower and upper limits are also presented in the figures. It is noticed that the experimental data show a large scatter and only a few results are available. The results by the statistical analysis are therefore not very good. The application of the statistical lower limit may be too conservative. Thus the J_R-curve which forms the lowest experimental limit is also provided. This experimental lowest J_R-curve is denoted as *J*-lowest in Figure M5 and M6.

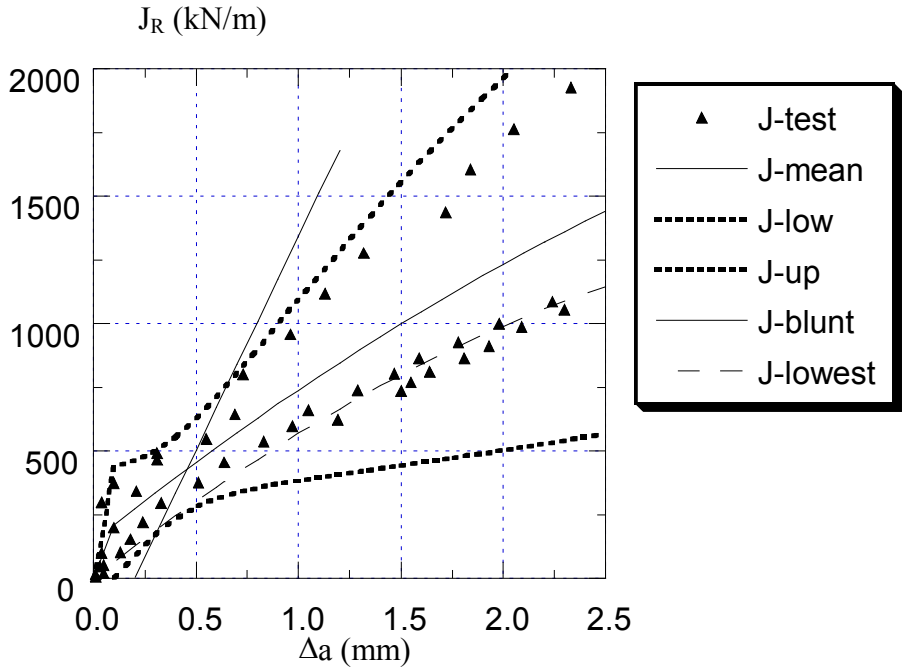

Figure M5. J_R-curves for GTAW welding (304) at room temperature, ref. [M2]. The equation for *J*-mean is $J_R = 765.47(\Delta a)^{0.6454}$, *J*-upper is $J_R = 1183.7(\Delta a)^{0.6273}$ and *J*-lowest is $J_R = 545.76(\Delta a)^{0.8908}$.

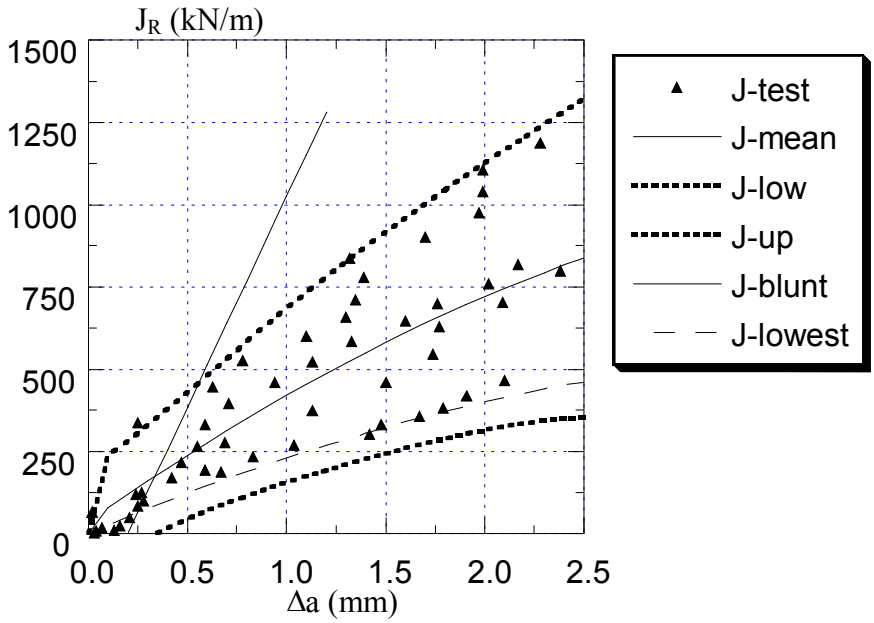

Figure M6. J_R-curves for GTAW welding (304) at 288 °C, ref. [M2]. The equation for *J*-mean is $J_R = 418.45(\Delta a)^{0.7740}$, *J*-upper is $J_R = 717.44(\Delta a)^{0.5949}$ and *J*-lowest is $J_R = 220.13(\Delta a)^{0.8911}$.

M2.4 Irradiated austenitic stainless steel, pipes

In this section, fracture toughness data from irradiated austenitic stainless steels are presented. It is known that the fracture toughness will vary with the degree of irradiation. Neutron fluence (integrated damage) is reported in n/cm^2 or dpa (displacement per atom). For stainless steel, 1dpa $\approx 7 \cdot 10^{20}$ n/cm^2 for $E > 1$ MeV. In Sweden, the neutron fluence for a moderator tank in a BWR station is about 0.3 dpa $\approx 2 \cdot 10^{20}$ n/cm^2. The effect of the irradiation can be divided in three domains:

i) The irradiation has marginal effect on the fracture toughness.

At a low neutron fluence level, about 0.3 dpa, it is shown by experiments that the irradiation has only a marginal effect on the fracture toughness for base materials. Experiments show that the neutron fluence has some negative effects on the fracture toughness for base materials subjected to moderate neutron fluence level about 1 dpa. In this study, only specimens fabricated from materials removed from service were used. Fracture toughness data are listed in table M3 for austenitic base materials.

Table M3. Fracture toughness data for irradiated austenitic base material, ref [M2].

Material type	Temperature °C	Dose (dpa)	J_{Ic} (kN/m)	Crack growth
304	20	0,8	596	Stable
304	199	0,9	395	Stable
304	249	0,9	297	Stable

ii) The irradiation between 1-10 dpa, the toughness decrease with the time of irradiation.

At 2 dpa for base stainless steel type 304 the fracture toughness is about 200 kN/m at 125 °C. However, no experiments have been performed for materials subjected a neutron fluence of about 3-5 dpa. In this neutron fluence there is lack of data.

iii) The irradiation over 10 dpa, the toughness is independent of the irradiation time.

Comparison between fracture toughness for unirradiated and irradiated material indicates radiated base material 304 in the range 10 till 19 dpa, have a decrease in the fracture toughness with a factor of 10, Ref [M4]. The fracture toughness for radiated stainless steel is in the range 25–35 kN/m.

M2.5 Irradiated austenitic stainless steel, welding components

Unirradiated welded austenitic stainless steels, type 308, have better fracture toughness than irradiated welded stainless steels. Fracture toughness for typical irradiated austenitic welding material, 308 L, at different irradiation levels, is given in table M4.

Table M4. Fracture toughness data for irradiated austenitic welds, ref [M2] and [M4]. The welding methods are shielded metal arc welds (SMAW).

Material type	Temperature °C	Dose (dpa)	J_{Ic} (kN/m)
308L / SMAW	25	0,7	143
308L / SMAW	199	0,6	125
308L / SMAW	25	11	10-15
308L / SMAW	150	11	10-15
308L / SMAW	259	11	10-15

M2.6 Cast stainless steel

Cast stainless steels are normally ductile and have a fracture toughness of the same level as the stainless steel base material in table M2. However, cast duplex stainless steels are subjected to thermal ageing which causes an embrittlement of the ferritic phase. The degree of embrittlement is determined mainly by the ferritic content, ageing time and exposure temperature. For a ferritic content of less than 10 %, the risk of embrittlement should be small for component aged at about 300 °C. A lower bound value for J_{Ic} of 100 kJ/m^2 has been measured for highly embrittled materials. Fracture toughness data are reported in [M6], [M7] and [M8].

M2.7 Stainless steel cladding

Many ferritic pressure vessels and piping used for nuclear applications are cladded with a stainless steel layer. Fracture properties for these materials are scarce. J_R-curves for three-wire series-arc weld overlay cladding with combinations of type 304, 308 and 309 stainless steel are reported in [M9]. Unirradiated fracture toughness data (mean values of three tests) are given in table M5. Fracture toughness data for cladding are also reported in [M10] at 60 °C, which is of the same order as those of [M9]. In [M9], the influence from neutron irradiation on the fracture toughness properties of the cladding is also quantified. At 2 mm of stable crack growth, a J_R-value of 450 kJ/m^2 at 120 °C is reported in [M9] in the unirradiated condition, which also agrees well with [M10] at 60 °C.

Table M5. Fracture toughness data for unirradiated stainless steel cladding, ref. [M9].

Temperature °C	J_{Ic} (kJ/m^2)	K_{cr} (MPa$\sqrt{\text{m}}$)
20	157	186
120	132	167
288	75	122

M2.8 Nickel base alloys

Very few fracture toughness data for nickel base alloys are found in the literature. Alloy 600 is normally very ductile and should have a fracture toughness of the same level as the stainless steel base material in Table M2. For the weld material alloy 182, room temperature data and high temperature data are published in [M11], [M12], [M13], [M14] and [M15]. Table M6 summarizes the results. It should be noted that formally the thickness requirement according to ASTM E-813 was not fulfilled in the testing in [M12] and [M13], and new testing data have been performed at room and high temperatures for alloy 182 according to ASTM E-1820, ref [M14] and [M15]. Data including a small amount of stable crack growth ($\Delta a = 1 - 2$ mm) is also included in Table M6 [M15].

Table M6. Fracture toughness data for alloy 182, ref [M14] and [M15].

Temperature °C	J_{Ic} (kJ/m^2)	K_{cr} (MPa$\sqrt{\text{m}}$)	$K_{1\text{mm}}$ (MPa$\sqrt{\text{m}}$)	$K_{2\text{mm}}$ (MPa$\sqrt{\text{m}}$)
20	182	205	—	—
≥ 190	377	285	335	411

Typical experimental J_R-curves for SMAW for alloy 182 at room temperature and at 288 °C is shown in figure M7 and figure M8 respectively. In this case the fracture toughness increase with the testing temperature. A comparison between the tests at 50 °C and 288 °C shows that the toughness increase with the testing temperature, and that the J_R-curve is steeper at high temperatures. Alloy 182 is a tough material compared to austenitic welding stainless steel (SAW and SMAW), which have lower toughness at high temperatures. For alloy 182 the yield stress is rather independent of the temperature, but for stainless steels the yield stress decrease with increasing temperature.

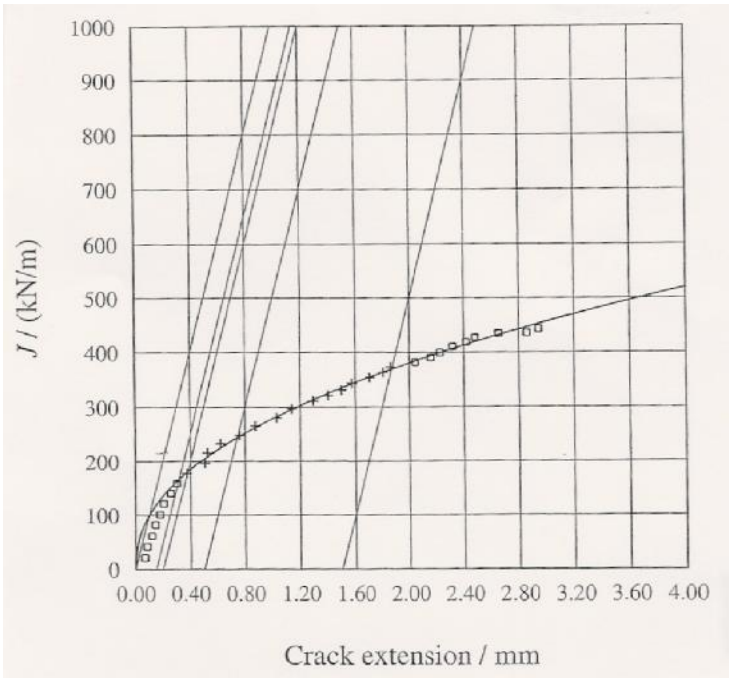

Figure M7. Typical J_R-curve for alloy 182 (SMAW-welding) at 50 °C, ref. [M14].

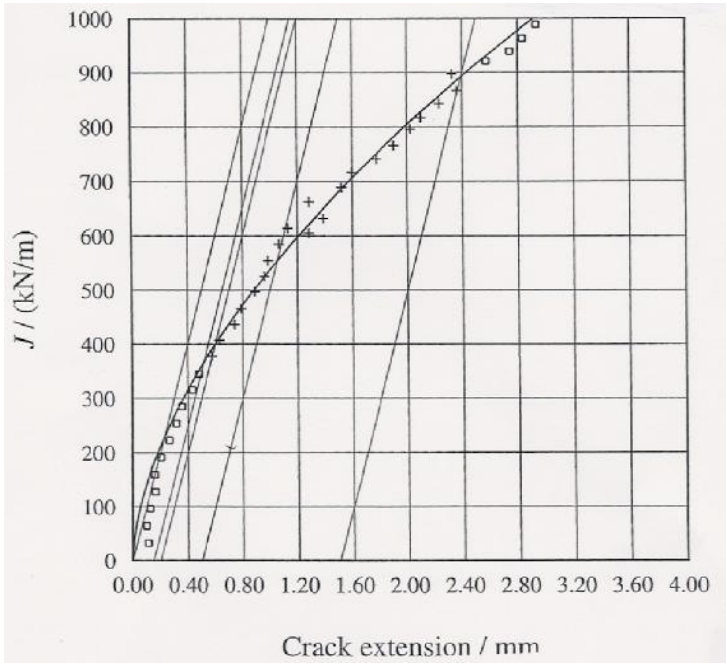

Figure M8. Typical J_R-curve for alloy 182 (SMAW-welding) at 190 °C (similar at 288 °C), ref. [M14]. The equation for *J*-mean, with 90 % confidence, is $J_R = 519.70(\Delta a)^{0.5956}$ [M15].

M3. Crack growth data, fatigue

Fatigue crack growth data for nuclear applications according to the 1995 edition of ASME sect. XI are presented below. Data for other materials and environments can be found in ref. [M16].

Generally the fatigue crack growth rate is written as

$$\frac{da}{dN} = C\left(\Delta K_{\mathrm{I}}\right)^{n} \quad \text{mm/cycle.} \tag{M2}$$

C and n are constants, and ΔK_{I} is the range of applied stress intensity factor during the load cycle, i.e.

$$\Delta K_{\mathrm{I}} = K_{\mathrm{I}}^{max} - K_{\mathrm{I}}^{min} \quad . \tag{M3}$$

Beside the environment, C and n may also depend on the so-called R-value defined as

$$R = \frac{K_{\mathrm{I}}^{min}}{K_{\mathrm{I}}^{max}} \quad . \tag{M4}$$

Both R and ΔK_{I} may be corrected with respect to a compressive phase during a load cycle. Below K_{I} is input in MPa$\sqrt{\mathrm{m}}$, which according to Eq. (M2) gives the growth rate in mm/cycle as output.

M3.1 Ferritic steel, plates, pressure vessels

Fatigue crack growth data for the material SA-533 Grade B Class 1, SA-508 Class 2 and SA-508 Class 3 can be found in ASME Sect. XI, article A-4000 for cracks both in air and reactor water environment. Values of C, n and ΔK_{I} are given in Table M7 for air environment.

Table M7. Crack growth data for fatigue of ferritic steel in air environment.

R	n	C [mm/(MPa$\sqrt{\mathrm{m}}$)^n]	ΔK_{I} [MPa$\sqrt{\mathrm{m}}$]
$R < -2$	3.07	$3.785 \cdot 10^{-9}$	$(1-R)K_{\mathrm{I}}^{max}/3$
$-2 \le R < 0$	3.07	$3.785 \cdot 10^{-9}$	K_{I}^{max}
$R \ge 0$	3.07	$9.734 \cdot 10^{-8}(2.88-R)^{-3.07}$	$K_{\mathrm{I}}^{max} - K_{\mathrm{I}}^{min}$

For reactor water environment, R is not allowed to fall below 0. ΔK_{I} is entitled low or high depending on if ΔK_{I} falls below or exceeds the parameter K defined in Table M8. Values of C, n is given in Table M9 and Table M10.

Table M8. Parameter K at different R-values.

R	K [MPa$\sqrt{\mathrm{m}}$]
$0 \le R \le 0.25$	19.49
$0.25 < R < 0.65$	$19.49\left(\frac{3.75R+0.06}{26.9R-5.725}\right)^{0.25}$
$0.65 \le R \le 1.0$	13.23

Table M9. Crack growth data for fatigue of ferritic steel in reactor water environment, with low ΔK_{I}-values $\Delta K_{\mathrm{I}} < K$.

R	n	C [mm/(MPa$\sqrt{\mathrm{m}}$)^n]
$0 \le R \le 0.25$	5.95	$1.479 \cdot 10^{-11}$
$0.25 < R < 0.65$	5.95	$1.479 \cdot 10^{-11}\left(26.9R - 5.725\right)$
$0.65 \le R \le 1.0$	5.95	$1.739 \cdot 10^{-10}$

Table M10. Crack growth data for fatigue of ferritic steel in reactor water environment, with high ΔK_{I}-values $\Delta K_{\mathrm{I}} \ge K$.

R	n	C [mm/(MPa$\sqrt{\mathrm{m}}$)^n]
$0 \le R \le 0.25$	1.95	$2.135 \cdot 10^{-6}$
$0.25 < R < 0.65$	1.95	$2.135 \cdot 10^{-6}\left(3.75R + 0.06\right)$
$0.65 \le R \le 1.0$	1.95	$5.337 \cdot 10^{-6}$

The fatigue crack growth rate for reactor water environment is not allowed to fall below the one for air environment.

M3.2 Austenitic stainless steel, pipes

Fatigue crack growth data for austenitic stainless steel, 304, at different frequencies are given in tables M11 ($f \geq 1$ Hz), M12 (0.1 Hz $\leq f < 1$ Hz) and M13 ($f < 0.1$ Hz).

Table M11. Crack growth data for fatigue of stainless steel, 304, in reactor water environment, $f \geq 1$ Hz [M16].

Environment	ΔK_{I} [MPa$\sqrt{\mathrm{m}}$]	da/dN [mm/cycle]
BWR + PWR	> 5	$6.41 \cdot 10^{-9} \left(1+1.8R\right) \Delta K_{\mathrm{I}}^{3.30}$
BWR + PWR	≤ 5	$3.10 \cdot 10^{-23} \Delta K_{\mathrm{I}}^{24.75}$

Threshold definition at $f \geq 1$ Hz; the ΔK_{I} where the crack growth rate is 10^{-9} mm/cycle, which gives the value 3.5 MPa$\sqrt{\mathrm{m}}$.

Table M12. Crack growth data for fatigue of stainless steel, 304, in reactor water environment, 0.1 Hz $\leq f < 1$ Hz [M16].

Environment	ΔK_{I} [MPa$\sqrt{\mathrm{m}}$]	da/dN [mm/cycle]
BWR + PWR	≥ 0	$6.41 \cdot 10^{-9} \left(1+1.8R\right) \Delta K_{\mathrm{I}}^{3.30}$

Table M13. Crack growth data for fatigue of stainless steel, 304, in reactor water environment, $f < 0.1$ Hz [M16].

Environment	ΔK_{I} [MPa$\sqrt{\mathrm{m}}$]	da/dN [mm/cycle]
BWR + PWR	≥ 0	$4.55 \cdot 10^{-8} \Delta K_{\mathrm{I}}^{3.35}$

M3.3 Alloy 182

Fatigue crack growth data for alloy 182, at different frequencies are given in tables M14 ($f \geq 0.1$ Hz) and M15 ($f < 0.1$ Hz).

Table M14. Crack growth data for fatigue of Alloy 182, in reactor water environment, $f \geq 0.1$ Hz [M16].

Environment	ΔK_I [MPa$\sqrt{\text{m}}$]	da/dN [mm/cycle]
BWR + PWR	> 5.45	$6.41 \cdot 10^{-9} \Delta K_I^{3.30}$
BWR + PWR	≤ 5.45	$5.63 \cdot 10^{-20} \Delta K_I^{18.31}$

Threshold definition; the ΔK_I where the crack growth rate is 10^{-9} mm/cycle, which gives the value 3.6 MPa$\sqrt{\text{m}}$.

Table M15. Crack growth data for fatigue of Alloy 182, in reactor water environment, $f < 0.1$ Hz [M16].

Environment	ΔK_I [MPa$\sqrt{\text{m}}$]	da/dN [mm/cycle]
BWR + PWR	≥ 0	$1.55 \cdot 10^{-8} \Delta K_I^{3.30}$

M3.4 Alloy 600

Fatigue crack growth data for alloy 600, at different frequencies are given in tables M16 ($f \geq 0.1$ Hz) and M17 ($f < 0.1$ Hz).

Table M16. Crack growth data for fatigue of Alloy 600, in reactor water environment, $f \geq 0.1$ Hz [M16].

Environment	ΔK_I [MPa$\sqrt{\text{m}}$]	da/dN [mm/cycle]
BWR + PWR+ air	> 6	$1.58 \cdot 10^{-9} \Delta K_I^{3.59}$
BWR + PWR+ air	≤ 6	$1.95 \cdot 10^{-23} \Delta K_I^{21.47}$

Threshold definition; the ΔK_I where the crack growth rate is 10^{-9} mm/cycle, which gives the value 4.3 MPa$\sqrt{\text{m}}$.

Table M17. Crack growth data for fatigue of Alloy 600, in reactor water environment, $f < 0.1$ Hz [M16].

Environment	ΔK_I [MPa$\sqrt{\text{m}}$]	da/dN [mm/cycle]
BWR + PWR	≥ 0	$6.41 \cdot 10^{-9} \Delta K_I^{3.30}$

M4. Crack growth data, stress corrosion

M4.1 BWR-environment

Stress corrosion crack growth data for stainless steels and nickel base alloys can be found in ref. [M17]. These data have been reviewed in ref. [M18] and ref. [M19]. The data are given in tables M18 (stainless steel in normal water chemistry), M19 (stainless steel in hydrogen water chemistry), M20 (Alloy 182 in normal water chemistry), M21 (Alloy 182 in hydrogen water chemistry), M22 (Alloy 600 in normal water chemistry) and M23 (Alloy 600 in hydrogen water chemistry).

Table M18. Stress corrosion crack growth rate for stainless steel in normal water chemistry.

Environment	K_I [MPa$\sqrt{\text{m}}$]	da/dt [mm/s]
BWR	< 55.5	$1.46 \cdot 10^{-12} K_I^{3.0}$
BWR	≥ 55.5	$2.5 \cdot 10^{-7}$

Table M19. Stress corrosion crack growth rate for stainless steel in hydrogen water chemistry [M17, M20].

Environment	K_I [MPa$\sqrt{\text{m}}$]	da/dt [mm/s]
BWR	< 55.5	$7.04 \cdot 10^{-14} K_I^{3.0}$
BWR	≥ 55.5	$1.2 \cdot 10^{-8}$

Table M20. Stress corrosion crack growth rate for Alloy 182 in normal water chemistry.

Environment	K_I [MPa$\sqrt{\text{m}}$]	da/dt [mm/s]
BWR	< 39	$2.56 \cdot 10^{-14} K_I^{4.96}$
BWR	≥ 39	$1.99 \cdot 10^{-6}$

Table M21. Stress corrosion crack growth rate for Alloy 182 in hydrogen water chemistry [M17, M21].

Environment	K_I [MPa$\sqrt{\text{m}}$]	da/dt [mm/s]
BWR	< 48	$6.77 \cdot 10^{-13} K_I^{3.23}$
BWR	≥ 48	$1.82 \cdot 10^{-7}$

Table M22. Stress corrosion crack growth rate for Alloy 600 in normal water chemistry.

Environment	K_I [MPa$\sqrt{\text{m}}$]	da/dt [mm/s]
BWR	—	$3.52 \cdot 10^{-12} K_I^{3.0}$

Table M23. Stress corrosion crack growth rate for Alloy 600 in hydrogen water chemistry [M22].

Environment	K_I [MPa$\sqrt{\text{m}}$]	da/dt [mm/s]
BWR	—	$1.5 \cdot 10^{-11} K_I^{3.0}$

M4.2 PWR-environment

For Alloy 182 in PWR-environment the stress corrosion crack growth rate at different temperatures are given in table M24 [M24, M25]. For Alloy 600 in PWR-environment the stress corrosion crack growth rate at different temperatures are given in table M25 [M23].

Table M24. Stress corrosion crack growth rate for Alloy 182 in PWR-environment.

Environment / Temperature	K_I [MPa$\sqrt{\text{m}}$]	da/dt [mm/s]
PWR / 290 °C	—	$1.47 \cdot 10^{-7}$
PWR / 320 °C	< 27.5	$3.61 \cdot 10^{-15} K_I^{5.76}$
	≥ 27.5	$7.0 \cdot 10^{-7}$
PWR / 345 °C	< 26.7	$1.05 \cdot 10^{-14} K_I^{5.76}$
	≥ 26.7	$1.74 \cdot 10^{-6}$

Table M25. Stress corrosion crack growth rate for Alloy 600 in PWR-environment.

Environment / Temperature	K_I [MPa$\sqrt{\text{m}}$]	da/dt [mm/s]
PWR / 290 °C	< 30	$4.00 \cdot 10^{-19} K_I^{7.5}$
	≥ 30	$4.79 \cdot 10^{-8}$
PWR / 320 °C	< 30	$7.0 \cdot 10^{-17} K_I^{6.5}$
	≥ 30	$2.79 \cdot 10^{-7}$
PWR / 345 °C	< 30	$1.6 \cdot 10^{-16} K_I^{6.5}$
	≥ 30	$6.39 \cdot 10^{-7}$

M5. References

[M1] NORRIS, D.M., (1988), "Evaluation of flaws in ferritic piping", Final Report EPRI NP-6045, EPRI Research Institute, U.S.A.

[M2] ZANG, W., and J. LINDER, (1998), "Fracture toughness and tensile properties for austenitic stainless steels and welds", SAQ/FoU-Report 98/01.

[M3] —, (2001), "Standard test method for measurement of fracture toughness", ASTM Standard E1820-01, American Society for Testing and Materials, Philadelphia.

[M4] SUND, G, (1991), "Fracture toughness of stainless steel", Report No. M-91/26 (in Swedish), Studsvik AB, Studsvik, Sweden.

[M5] LANDES, J. D., and D. E. McCABE, (1986), "Toughness of Austenitic Stainless Steel Pipe Welds", TopicalReport EPRI NP-4768, EPRI Research Institute, U.S.A.

[M6] Mc DONALD, P., and J. W., SHECKHERD, (1987), "Fracture toughness characterization of thermally aged cast stainless steels", EPRI NP-5439, EPRI Research Institute, U.S.A.

[M7] HISER, L., (1988), "Tensile and JR-curve characterization of thermally aged cast stainless steels", NUREG/CR-5024, USNRC, Washington D.C., U.S.A.

[M8] JANSSON, C., (1995), "Degradation of cast stainless steels-a literature survey", SKI Rapport 95:96 (in Swedish), Swedish Nuclear Power Inspectorate, Stockholm, Sweden.

[M9] HAGGAG, F. M., CORWIN, W. R., and R. K., NANSTAD, (1989), "Effects of irradiation on the fracture properties of stainelss steels weld overlay cladding", Post-SMIRT Conference No 2, Monterey, U.S.A.

[M10] SATTARI-FAR, I., (1995), "Constraint effects on ductile crack growth in cladded components subjected to uniaxial loading", *Fatigue & Fracture of Engineering Materials & Structures*, Vol.18, No.10, pp 1051-1069.

[M11] YOSHIDA, K., KOJIMA, M., IIDA, M. and I., TAKAHASHI, (1990), "Fracture toughness of weld metals in steel piping for nuclear power plants", *The International Journal of Pressure Vessels and Piping*, Vol. 43, pp. 273-284.

[M12] BERGENLID, U., (1991), "Fracture toughness of alloy 182 at room temperature", Report No. M-91/129 (in Swedish), Studsvik AB, Studsvik, Sweden.

[M13] BERGENLID, U., (1991), "Fracture toughness of alloy 182 at 285 °C", Report No. M-91/95 (in Swedish), Studsvik AB, Studsvik, Sweden.

[M14] ÖBERG, H., (2001), "Fracture mechanical testing of alloy 182", Report DNV 0102, Rev. 010312, The institution of fracture mechanics, Royal Technical School, Sweden.

[M15] DILLSTRÖM, P., (2002), "Fracture toughness data and JR-curves for Inconel 182", Technical Report 10827200-1 (in Swedish), Rev. 0, Det Norske Veritas AB.

[M16] JANSSON, C., and U. MORIN, (1995), "Fatigue crack growth in reactor material", MD-02 (in Swedish), Report GEK 87/95, Vattenfall Energisystem AB and Sydkraft Konsult, Sweden.

[M17] JANSSON, C., (1999), "Stress corrosion growth in BWR environment", MD-01, Rev. 3, Report T-SEK 41/99, SwedPower AB, Sweden.

[M18] SUND, G., (2000), "Review of MD-01 Rev.3", Report No 102424000-1 (in Swedish), DNV Nuclear Technology, Sweden.

[M19] RASHID, B., and G. SUND, (2001), "Review of new data points for the plateau of Alloy 182 and 304 in NWC according to MD-01 rev 3", BAR-01-06-28; 17:45, 11143301, Letter 2001-06-28 (in Swedish), DNV Nuclear Technology, Sweden.

[M20] ITOW, M., et al., (2000), "SCC crack growth rates of type 304 stainless steel at high K region in simulated BWR environment", *Corrosion 2000*, Paper No 00221.

[M21] ITOW, M., et al., (1997), "The effect of corrosion potential on alloy 182 crack growth rate in high temperature water", *8th International symposium on environmental degradation of Materials in Nuclear Power systems*, Amelia Island.

[M22] —, (1994), *SKIFS 1994:1*, Swedish Nuclear Inspectorate, Stockholm, Sweden.

[M23] RASHID, B., and G. SUND, (2002), "Review of stress corrosion crack growth rates curves of alloy 600 in PWR environment", BAR-02-02-14; 18:45, 1136601, Letter 2002-02-14 (in Swedish), DNV Nuclear Technology, Sweden.

[M24] RASHID, B., and G. SUND, G., (2002), "Review of stress corrosion crack growth rates curves of alloy 182 in PWR environment", BAR-02-04-25; 13:50, 11400701, Letter 2002-04-25 (in Swedish), DNV Nuclear Technology, Sweden.

[M25] SUND, G., (2002), "Crack growth at 290 °C in PWR-environment", Letter in Swedish at 2002-05-03, DNV Nuclear Technology, Sweden.

APPENDIX S. SAFETY FACTORS FOR NUCLEAR APPLICATIONS

For the choice of safety factors SF_K and SF_L, the objective has been to retain the safety margins expressed in ASME 1995, Sect. III and XI. The value of SF_L during normal and upset conditions originates from the ASME code requirement that the primary general membrane stress $P_m \le S_m$ and the flow stress σ_f, at which net section plastic collapse is assumed to occur, can be estimated to $2.4S_m$ and $3.0S_m$ for ferritic and austenitic materials, respectively. S_m is defined in section 2.10 in the main document. SF_K is the safety factor on K_{cr} and corresponds to the safety factor SF_J on J_{Ic}. They are related through $SF_K = \sqrt{SF_J}$. More information about the development of these safety factors can be found in Ref. [S1]. Tables S1 to S3 show the safety factors aimed for ferritic steel components, austenitic piping and ferritic piping, respectively. For austenitic components other than pipes we recommend the same safety factors as for an axial crack in an austenitic piping.

Table S1. Safety factors for ferritic steel components other than pipes.

Type of load event	SF_K	SF_L
Normal/Upset	$\sqrt{10}$	2.4 (1)
Emergency/Faulted	$\sqrt{2}$	1.2

(1) May be divided by 1.5 if the only primary stress is a local membrane stress P_L.

Table S2. Safety factors for austenitic piping.

	Circumferential crack		Axial crack	
Type of load event	SF_K	SF_L	SF_K	SF_L
Normal/Upset	$\sqrt{10}$	2.77 (2)	$\sqrt{10}$	3.0 (2)
Emergency /Faulted	$\sqrt{2}$	1.39	$\sqrt{2}$	1.5

(2) May be divided by 1.5 if the only primary stress is a local membrane stress P_L.

Table S3. Safety factors for ferritic piping.

	Circumferential crack		Axial crack	
Type of load event	SF_K	SF_L	SF_K	SF_L
Normal/Upset	$\sqrt{10}$	2.22 (3)	$\sqrt{10}$	2.4 (3)
Emergency/Faulted	$\sqrt{2}$	1.11	$\sqrt{2}$	1.2

(3) May be divided by 1.5 if the only primary stress is a local membrane stress P_L.

One drawback with the deterministic safety evaluation system above is that it may overestimate the contribution from secondary stresses (i.e. welding residual stresses or stresses from a thermal transient) for ductile materials. This has to do with the fact that there is only a large influence of residual stresses on load carrying capacity at low L_r-values. The influence reduces as L_r increases and for larger L_r values there is no effect at all. This has been shown by different experimental programmes [S2]. The Swedish Nuclear Power Inspectorate and Det Norske Veritas has therefore started a project that will lead to a quantitative recommendation on how to treat secondary stresses for high L_r-values in a R6 fracture assessment. This recommendation will define new safety factors against fracture described by K_{I} and differentiate between $SF_K^{Primary}$ (relating to primary stresses) and $SF_K^{Secondary}$ (relating to secondary stresses). The results from this project will be incorporated in the next revision of the handbook.

The safety margins expressed in the latest edition of ASME, Sect. XI are different from the margins given in the tables above [S3]. In table S1 to S3, one safety factor is specified for Normal/Upset load events and one for Emergency/Faulted load events. In the 2002 Addenda to Sect. XI, separate safety factors for the load events Normal, Upset, Emergency and Faulted were introduced [S3]. Also for circumferential cracks, there are now separate safety factors for membrane and bending stresses [S3]. These changes will be incorporated in a coming edition of the handbook.

S1. References

[S1] BRICKSTAD, B., and M. BERGMAN, (1996), "Development of safety factors to be used for evaluation of cracked nuclear components", SAQ/FoU-Report 96/07, SAQ Kontroll AB, Stockholm, Sweden.

[S2] SHARPLES, J. K., SANDERSON, D. J., BOWDLER, B. R., WIGHTMAN, A. P. and R. A. AINSWORTH, (1995), "Experimental programme to assess the effect of residual stresses on fracture behaviour", *Proceedings of the 1995 ASME Pressure Vessels & Piping Conference*, V. 437, pp. 539-551.

[S3] SCARTH, D. A., WILKOWSKI, G. M., CIPOLLA, R. C., DAFTUAR, S. K., and K. K. KASHIMA, (2003), "Flaw evaluation procedures and acceptance criteria for nuclear piping in ASME Code Section XI", *Proceedings of the 2003 ASME Pressure Vessels & Piping Conference*, V. 463, pp. 45-61.

APPENDIX P. PROBABILISTIC ANALYSIS

In this forth edition of the handbook, a new probabilistic procedure has been included to calculate two different failure probabilities, P_F :

- Probability of failure, defect size given by NDT/NDE.
- Probability of failure, defect not detected by NDT/NDE.

P1. Failure probabilities

The procedure [P1-P2] uses two different limit state functions, $g(X)$ ($g_{FAD}(X)$ and $g_{L_r^{max}}(X)$).

$$g_{FAD}(X) = f_{FAD}(X) - K_r(X) \quad , \tag{P1}$$

$$g_{L_r^{\max}}(X) = L_r^{\max}(X) - L_r(X) \quad . \tag{P2}$$

These limit state functions are based on a simplified R6 failure assessment curve [P3-P4]. To calculate the probability of failure, a multi-dimensional integral has to be evaluated [P1-P2]:

$$P_F = \Pr\left[g(X) < 0\right] = \int_{g(X)<0} f_X(x)dx \quad . \tag{P3}$$

The set where the above analysed event is fulfilled, is formulated as $g(X) < 0$, and is called the failure set. The set where $g(X) > 0$ is called the safe set. $f_X(x)$ is a known joint probability density function of the random vector *X*. This integral is very hard (impossible) to evaluate, by numerical integration, if there are many random parameters.

P2. Parameters

Within the procedure, the following parameters are treated as random parameters:

- Fracture toughness
- Yield strength
- Ultimate tensile strength
- Primary stresses
- Secondary stresses
- Defect size (depth) given by NDT/NDE
- Defect distribution (when a defect is not detected by NDT/NDE)
- POD-curve (when a defect is not detected by NDT/NDE)
- Constants in the fatigue crack growth law
- Constants in the SCC crack growth law

These random parameters are treated as not being correlated with one another. The parameters can follow a normal, lognormal, Weibull or an exponential distribution.

P2.1 Fracture toughness

The fracture toughness can follow a normal, lognormal or Weibull distribution.

The normal probability density function has the following form:

$$f(K_I) = \frac{1}{\sigma_{K_{Ic}} \cdot \sqrt{2 \cdot \pi}} \exp\left(-\frac{1}{2} \cdot \left[\frac{K_I - \mu_{K_{Ic}}}{\sigma_{K_{Ic}}} \right]^2 \right) \quad , \tag{P4}$$

where $\mu_{K_{Ic}}$ (mean) and $\sigma_{K_{Ic}}$ (standard deviation) are input data to ProSACC.

The lognormal probability density function has the following form:

$$f(K_I) = \frac{1}{K_I \cdot \sigma_{LogNor} \cdot \sqrt{2 \cdot \pi}} \exp\left(-\frac{1}{2} \cdot \left[\frac{\ln(K_I) - \mu_{LogNor}}{\sigma_{LogNor}} \right]^2 \right) \quad , \tag{P5}$$

where μ_{LogNor} and σ_{LogNor} are the log-normal distribution parameters. $\mu_{K_{Ic}}$ (mean) and $\sigma_{K_{Ic}}$ (standard deviation) are input data to ProSACC and are related to the lognormal distribution parameters as follow:

$$\mu_{LogNor} = \ln\left(\mu_{K_{Ic}}\right) - \frac{1}{2} \cdot \left(\sigma_{LogNor}\right)^2 \quad , \tag{P6}$$

$$\sigma_{LogNor} = \sqrt{\ln\left[1 + \left(\frac{\sigma_{K_{Ic}}}{\mu_{K_{Ic}}}\right)^2\right]} \quad . \tag{P7}$$

The Weibull probability density function has the following form:

$$f(K_I) = \frac{k}{\theta} \cdot \left(\frac{K_I}{\theta}\right)^{k-1} \cdot \exp\left(-\left(\frac{K_I}{\theta}\right)^k \right) \quad , \tag{P8}$$

where θ (scale) and k (shape) are the Weibull distribution parameters. $\mu_{K_{Ic}}$ (mean) and $\sigma_{K_{Ic}}$ (standard deviation) are input data to ProSACC and are related to the Weibull distribution parameters as follow:

$$\mu_{K_{Ic}} = \frac{\theta}{k} \cdot \Gamma\left(\frac{1}{k}\right) \quad , \tag{P9}$$

$$\sigma_{K_{Ic}} = \sqrt{\frac{\theta^2}{k} \cdot \left[2 \cdot \Gamma\left(\frac{2}{k}\right) - \frac{1}{k} \cdot \Gamma\left(\frac{1}{k}\right)^2 \right]} \quad , \tag{P10}$$

where $\Gamma(z)$ is the gamma function, defined by the integral

$$\Gamma(z) = \int_0^\infty t^{z-1} \cdot e^{-t} dt \qquad \text{(P11)}$$

This non-linear system of equations is solved (within ProSACC) using a globally convergent method with line search and an approximate Jacobian matrix.

P2.2 Yield strength and Ultimate tensile strength

The Yield strength and the Ultimate tensile strength can follow a normal, lognormal or Weibull distribution. For information regarding input data and distribution parameters, see section P2.1 above.

P2.3 Primary stresses / Secondary stresses

The Primary stresses and the Secondary stresses can follow a normal distribution. For information regarding input data and distribution parameters, see section P2.1 above.

P2.4 Defect size given by NDT/NDE / Defect size distribution

The defect size given by NDT/NDE or the defect size distribution can follow a normal, lognormal or exponential distribution. For information regarding input data and distribution parameters, using a normal or lognormal distribution, see section P2.1 above.

The exponential probability density function has the following form:

$$f(a) = \lambda \cdot \exp(-\lambda \cdot a) \quad , \qquad \text{(P12)}$$

where λ is the exponential distribution parameter. μ_a (mean) is input data to ProSACC (equal to the standard deviation, σ_a, for this distribution) and is related to λ as follows:

$$\mu_a = \sigma_a = \frac{1}{\lambda} \quad . \qquad \text{(P13)}$$

P2.5 POD-curve / Defect not detected by NDT/NDE

The parameter defect not detected by NDT/NDE can follow a non-constant POD-distribution (POD – Probability Of Detection):

$$\mathrm{POD} = F_{\mathrm{POD}}\left(\frac{a}{t}\right) = \Phi\left(c_1 + c_2 \ln\left(\frac{a}{t}\right)\right) \quad , \tag{P14}$$

where $\Phi(\ldots)$ is the cumulative distribution function in a standard normal space, a is the defect depth and t is the wall thickness.

P2.6 Constants in the fatigue crack growth law / SCC crack growth law

The Constants in the fatigue crack growth law and the Constants in the SCC crack growth law can follow a normal distribution. For information regarding input data and distribution parameters, see section P2.1 above.

P3. Calculation of failure probabilities

As mentioned above, the failure probability integral is very hard to solve using numerical integration. Instead, the following numerical algorithms are included within the procedure [P1-P2]:

- Simple Monte Carlo Simulation (MCS)
- First-Order Reliability Method (FORM)

P3.1 Simple Monte Carlo Simulation (MCS)

MCS is a simple method that uses the fact that the failure probability integral can be interpreted as a mean value in a stochastic experiment [P6]. An estimate is therefore given by averaging a suitably large number of independent outcomes (simulations) of this experiment.

The basic building block of this sampling is the generation of random numbers from a uniform distribution (between 0 and 1). Simple algorithms ”repeats themselves” (already) after approximately $2 \cdot 10^3$ to $2 \cdot 10^9$ simulations and are therefore not suitable to calculate medium to small failure probabilities [P6-P7]. The algorithm chosen for ProSACC repeats itself after approx. $2 \cdot 10^{18}$ simulations [P7]. This algorithm is approximately 20 times slower than the simpler algorithms mentioned above, but it is recommended if one needs more than $1 \cdot 10^8$ simulations.

Once a random number u, between 0 and 1, has been generated, it can be used to generate a value of the desired random variable with a given distribution. A common method is the inverse transform method. Using the cumulative distribution function $F_X(x)$, the random variable would then be given as:

$$x = F_X^{-1}(u) \quad . \tag{P15}$$

To calculate the failure probability, one performs N deterministic simulations and for every simulation checks if the component analysed has failed (i. e. if $g(X) < 0$). The number of failures is N_F, and an estimate of the mean probability of failure is:

$$P_{F,MCS} = \frac{N_F}{N} \quad . \tag{P16}$$

An advantage with MCS, is that it is robust and easy to implement into a computer program, and for a sample size $N \to \infty$, the estimated probability converges to the exact result. Another advantage is that MCS works with any distribution of the random variables and there is no restriction on the limit state functions.

However, MCS is inefficient when calculating failure probabilities, since most of the contribution to P_F is in a limited part of the integration interval.

In ProSACC a simple error estimate (of the probability of failure) is calculated [P8]:

$$\varepsilon_{MCS} = \sqrt{\frac{1 - P_{F,MCS}}{N \cdot P_{F,MCS}}} \cdot \Phi^{-1}\left(\frac{1+\alpha}{2}\right) \quad , \tag{P17}$$

where $\Phi(\ldots)$ is the cumulative distribution function in a standard normal space and α is a given confidence level (in ProSACC a constant value of 95% confidence is used).

P3.2 Monte Carlo Simulation with Importance Sampling (MCS-IS)

MCS-IS is an algorithm that concentrates the samples in the most important part of the integration interval. Instead of sampling around the mean values (MCS), one samples around the most probable point of failure (MCS-IS). This point, called MPP, is generally evaluated using information from a FORM / SORM analysis (see section P3.3 below). This algorithm is not included in the present release of ProSACC.

P3.3 First/Second-Order Reliability Method (FORM / SORM)

FORM / SORM uses a combination of both analytical and approximate methods, when estimating the probability of failure [P6, P9].

First, one transforms all the variables into equivalent normal variables in standard normal space (i. e. with mean = 0 and standard deviation = 1). This means that the original limit state surface $g(x)=0$ then becomes mapped onto the new limit state surface $g_U(u)=0$.

Secondly, one calculates the shortest distance between the origin and the limit state surface (in a transformed standard normal space *U*). The answer is a point on this surface, and it is called the most probable point of failure (MPP), design point or β-point. The distance between the origin and the MPP is called the reliability index β_{HL} (see figure P1).

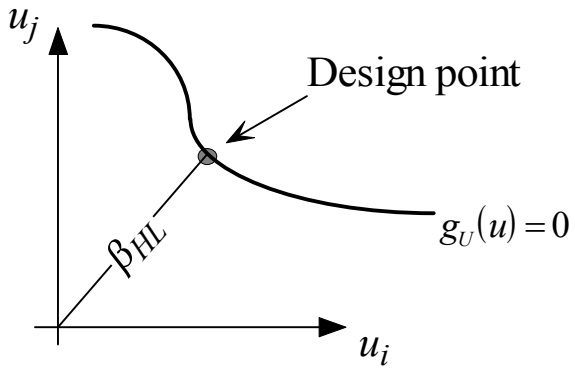

Figure P1. The definition of design point / MPP and reliability index β_{HL}.

In general, it requires an appropriate non-linear optimisation algorithm to calculate the most probable point of failure.

One suitable choice to calculate the MPP is the NLPQL-algorithm by Schittkowski [P10]. This algorithm, for example used in the general-purpose probabilistic analysis program PROBAN [P11], was also tested in ProSACC [P1]. It gave excellent results for the geometry ”a plate with an infinite surface defect”, using analytic geometry functions. However, for the other geometries

(with tabulated geometry functions), it gave quite slow convergence (or no convergence at all for the geometry ”a cylinder with a part circumferential internal surface defect”). Therefore, the NLPQL-algorithm was not chosen for ProSACC.

In [P9] a linearization of the limit state function is used to calculate the MPP.

$$y_{i+1} = \frac{1}{\left|\nabla g_U(y_i)\right|^2} \cdot \left[\nabla g_U(y_i) \cdot y_i - g_U(y_i)\right] \cdot \nabla g_U(y_i)^T \quad , \tag{P18}$$

where y_i is the current approximation to the MPP and $\nabla g_U(y_i)$ is the gradient of the limit state function. This algorithm, generally called the Rackwitz & Fiessler (R & F) algorithm [P12], is commonly used when evaluating P_F, mainly because it is very easy to implement and it converges fast in many cases. However, the R & F algorithm converges extremely slowly in some cases or oscillates about the solution without any convergence at all. In ProSACC both of these problems occur when $P_F > 0.8$ or when $P_F < 10^{-7}$ (also between these values in some cases). Therefore, the R & F algorithm was not chosen for ProSACC.

In ProSACC, a modified Rackwitz & Fiessler algorithm [P13-P14] was chosen. It works by ”damping” the gradient contribution of the limit state function and this algorithm is very robust and converges quite fast for most cases. In this algorithm one defines a search direction vector d_i:

$$d_i = \frac{1}{\left|\nabla g_U(y_i)\right|^2} \cdot \left[\nabla g_U(y_i) \cdot y_i - g_U(y_i)\right] \cdot \nabla g_U(y_i)^T - y_i \quad . \tag{P19}$$

A new approximation to the MPP can then be calculated:

$$y_{i+1} = y_i + s_i \cdot d_i \quad . \tag{P20}$$

The step size s_i as given in [P13] gave quite slow convergence (or no convergence at all for the geometry ”a cylinder with a part circumferential internal surface defect”), especially when dealing with the L_r^{max} limit state function in Eq. (P2). Instead a step size s_i was selected as given in [P14] such that the inequality $m(y_i + s_i d_i) < m(y_i)$ holds, where $m(y_i)$ is the merit function:

$$m(y_i) = \frac{1}{2} \cdot \left|y_i\right|^2 + c \cdot \left|g_U(y_i)\right| \quad , \tag{P21}$$

in which c is a parameter satisfying the condition $c > |y_i| / |\nabla g_U(y_i)|$ at each step i. This algorithm is globally convergent, i. e., the sequence is guaranteed to converge to a minimum-distance point on the limit state surface, provided $g_U(u)$ is continuous and differentiable [P14].

Finally, one calculates the failure probability using an approximation of the limit state surface at the most probable point of failure [P6, P9]. Using FORM, the surface is approximated to a hyperplane (a first order / linear approximation). SORM uses a second order / quadratic approximation to a hyperparaboloid (see figure P2.).

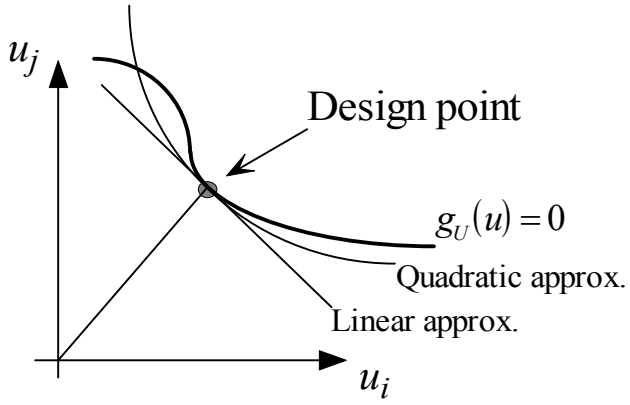

Figure P2. Schematic difference between a linear and a quadratic approximation of the limit state surface.

The probability of failure is given as [P6, P9]:

$$P_{F,FORM} = \Pr\left[g_{Linear}(u) < 0\right] = \Phi(-\beta_{\mathrm{HL}}) \quad , \tag{P22}$$

$$P_{F,SORM} = \Pr\left[g_{Quadratic}(u) < 0\right] \approx \Phi(-\beta_{\mathrm{HL}}) \cdot \prod_{i=1}^{N-1} \left(1 - \kappa_i \cdot \beta_{\mathrm{HL}}\right)^{-1/2} \quad , \tag{P23}$$

where $\Phi(u)$ is the cumulative distribution function in standard normal space and κ_i are the principal curvatures of the limit state surface at the most probable point of failure (MPP).

FORM / SORM are, as regards CPU-time, extremely efficient as compared to MCS. Using the FORM implementation within ProSACC, you get quite accurate results for failure probabilities between 10^{-1} to 10^{-15}. A disadvantage is that the random parameters must be continuous, and every limit state function must also be continuous. SORM is not included in the present release of ProSACC.

P3.4 Failure probability after an inspection

The algorithms presented above are applied when calculating the probability of failure before an inspection. When an inspection has been carried out, there are three levels of information available from the inspection [P15]:

- No detection: This implies that there either does not exist any defect, or that the defect size is less than the detection ability of the inspection method used.
- Detection without any sizing: This implies that a defect has been detected, but the size of the defect has not been sized.
- Detection with sizing: This implies that a defect has been detected and the size of the defect has been measured.

In addition there is a possibility of false identification, which is not included in our model.

Now the following events are defined [P15]:

- The limit state event: $G(t)$ This event is given by the R6-limit state functions defined in section P1. $G(t)$ less than zero implies failure at time *t*.
- The detection event: $D(t_i)$ This event is defined by evaluating the detectable defect size against the actual defect size at time t_i. $D(t_i)$ less than zero implies that the defect has been detected at time t_i.

Finally, the following failure probabilities are defined [P15]:

- The probability of failure at time *t*, before an inspection is then

$$P_F(t) = \Pr[G(t) \le 0] \quad . \tag{P24}$$

- The probability of failure at time *t*, after an inspection at time t_i without any defect detection is then ($t > t_i$)

$$P_F(t) = \Pr[G(t) \le 0 \mid D(t_1) > 0] \quad . \tag{P25}$$

- The probability of failure at time *t*, after *N* multiple inspections without any defect detection is then ($t > t_N > \ldots > t_2 > t_1$)

$$P_F(t) = \Pr[G(t) \le 0 \mid D(t_1) > 0 \cap D(t_2) > 0 \cap \ldots \cap D(t_N) > 0] \quad . \tag{P26}$$

The additional information from the inspection is included in the probability formulation through a conditioning, implying that the failure probability is estimated conditioned on the observed outcome from the inspections that have been carried out. The more available information that is

included in the modelling of the failure probability, the more accurately the integrity of the system may be assessed.

In risk based inspection (RBI) studies, our main concern is non-detection of defects. Therefore, we want to evaluate the probability of failure at time t, after an inspection at time t_1 not resulting in any defect detection. Using Bayes theorem, Eq. (P25) becomes

$$P_F(t) = \frac{\Pr\left[G(t) \le 0 \cap D(t_1) > 0\right]}{\Pr\left[D(t_1) > 0\right]} \quad . \tag{P27}$$

The limit state event $G(t)$ and the detection event $D(t_1)$ should not be mutually exclusive, since we are interested in events where $\Pr\left[G(t) \le 0 \cap D(t_1) > 0\right] \neq 0$. If the two events were independent events, we would get the trivial solution $\Pr\left[G(t) \le 0 \mid D(t_1) > 0\right] = \Pr\left[G(t) \le 0\right]$. Therefore, the two events must be dependent of each other.

To simplify the calculations, we now assume that the outcome of the detection event is linked to a repair strategy for the component (when a defect is detected, it is assumed that either an effective repair is made or that the defect is kept under close surveillance until the next inspection). Detected defects are then assumed not to contribute to the failure probability. We therefore suggest the following simplification, when calculating the failure probability (the detection event is evaluated at the most probable point of failure).

$$P_F(t) \approx \Pr\left[G(t) \le 0\right] \cdot \Pr\left[D(t_1) > 0\right] = \Pr\left[G(t) \le 0\right] \cdot \left(1 - \Pr\left[D(t_1) \le 0\right]\right) \tag{P28}$$

The assumption above is not valid for a general case, but the resulting error in a RBI study of a reactor pressure vessel is insignificant. This is verified in App. B.

P4. Some remarks

No formal sensitivity analysis is done within the procedure [P1-P2]. However, simple sensitivity factors are calculated when using FORM. These sensitivity factors use the most probable point of failure (MPP) in a standard normal space. Using ProSACC [P5], it is possible to estimate partial safety factors, given a target failure probability and characteristic values for the random parameters included in the analysis.

Verification has been carried out, using the probabilistic computer program STAR6 from Nuclear Electric [P16] and the deterministic program SACC from Det Norske Veritas AB [P17]. This is presented in App. B. Another important aspect in the development of a new probabilistic flaw evaluation procedure is to compare the behaviour against other published procedures and software. Such a benchmark is presented in App. B.

The statistical distribution used for an input parameter has an important impact on the resulting failure probabilities. This is especially true when calculating small failure probabilities. Another important factor is the data used in the probabilistic analysis. Examples on distributions and data to be used are discussed in App. B [P1-P2].

P5. References

[P1] DILLSTRÖM, P., (2000), ”Probabilistic Safety Evaluation - Development of Procedures with Applications on Components Used in Nuclear Power Plants”, SKi Report 00:58, Swedish Nuclear Power Inspectorate.

[P2] DILLSTRÖM, P., (2000), “ProSINTAP - A probabilistic program implementing the SINTAP assessment procedure”, *Engng Fract Mech*, V. 67, pp. 647-668.

[P3] MILNE, I., AINSWORTH, R. A., DOWLING, A. R., and A. T. STEWART, (1988), “Assessment of the integrity of structures containing defects”, *The International Journal of Pressure Vessels and Piping*, Vol. 32, pp. 3-104.

[P4] —, (2003), “Assessment of the Integrity of Structures Containing Defects”, R6 – Revision 4, Up to amendment record No.2, British Energy Generation Ltd.

[P5] DILLSTRÖM, P., and W. ZANG., (2004), “User manual ProSACC Version 1.0”, DNV Research Report 2004/02, Det Norske Veritas AB, Stockholm, Sweden.

[P6] DITLEVSEN, O., and H. O. MADSEN., (1996), *Structural reliability methods*, John Wiley & Sons Ltd, Baffins Lane, Chichester, 372p.

[P7] PRESS, W. H., and S. A. TEUKOLSKY., (1992), ”Portable Random Number Generators”, *Computers in Physics*, V 6, n 6, pp 522-524.

[P8] MONTGOMERY, D. C., and G. C. RUNGER., (1994), *Applied Statistics and Probability for Engineers*, John Wiley & Sons, Inc, New York, 895p.

[P9] MADSEN, H. O., KRENK, S., and N. C. LIND., (1986), *Methods of structural safety*, Prentice-Hall, Inc., Englewood Cliffs, New Jersey, 403p.

[P10] SCHITTKOWSKI, K., (1985/6), ”NLPQL: A Fortran Subroutine Solving Constrained Nonlinear Programming Problems”, *Annals of Operations Research*, V 5, pp 485-500.

[P11] —, (1996), ”SESAM Theory Manual, PROBAN, General Purpose Probabilistic Analysis Program”, DNV Software Report No. 96-7017/Rev. 0, Det Norske Veritas, 145p.

[P12] RACKWITZ, R., and B. FIESSLER., (1978), ”Structural Reliability Under Combined Random Load Sequences”, *Journal of Computers and Structures*, V 9, pp 489-494.

[P13] LIU, P-L., and A. DER KIUREGHIAN., (1986), ”Optimization Algorithms for Structural Reliability Analysis”, Report UCB/SESM-86/09, Department of Civil Engineering, University of California, Berkeley, 37p.

[P14] DER KIUREGHIAN, A., and T. DAKESSIAN., (1998), ”Multiple design points in first and second-order reliability”, *Structural Safety*, V 20, pp 37-49.

[P15] CRAMER, E., and G. SIGURDSSON., (1998-03-30), “RBI Offshore, Probabilistic Modelling”, Technical Report 97-3789, Rev. 2, Det Norske Veritas AS.

[P16] WILSON, R., (1995), “A User`s Guide to the Probabilistic Fracture Mechanics Computer Code: STAR6 - Version 2.2”, Memorandum TEM/MEM/0005/95, Nuclear Electric, Engineering Division, 75p.

[P17] BERGMAN, M., (1996), “User`s manual SACC version 4.0”, SAQ/FoU-Report 96/09, SAQ Kontroll AB, 9p.

APPENDIX B. BACKGROUND

This appendix gives the background to the current edition of the handbook and it's accompanying PC-program ProSACC [B1]. The objectives have been to remove some of the unnecessary conservatism that existed in the previous edition, to update the handbook with respect to recent research and finally to make the new edition of the handbook and PC-program even more user-friendly. We will continue this work and as better knowledge and solutions become available, or specific user demands are expressed new editions of the handbook and PC-program will be released. Some of the planned future work is also described below.

B1. Assessment method

The method utilized in this handbook is based on the R6-method developed at Nuclear Electric plc. [B2]. The third revision of the R6-metod contains three different options for determination of the safe region in the failure assessment diagram. The option 1 is a general non-material specific failure assessment diagram intended to use as a first approach. If a more accurate failure assessment diagram is needed either option 2 can be used where the failure assessment curve is derived from the materials stress-strain curve, or option 3 where the failure assessment curve is based on complete numerical *J*-integral calculations for different levels of primary load. In addition, the R6-method contains three different types of analysis, categories, depending on how stable crack growth shall be considered. For category 1 no stable crack growth is allowed while for category 2 and 3 some amount of ductile tearing can be accounted for in the assessment. During the development of this edition of the handbook, the forth revision of the R6-document were released [B3]. It contains many new features and updates that will be included in the next edition of this handbook. As an example, newly developed failure assessment diagrams are included that more realistically can handle cases with large L_r-values (now only positive values are accepted).

In order to make the procedure safe and easy to use, the procedure has been restricted to the option 1 and category 1 type of the R6-method [B2]. The option 1 type is however, not intended for materials with a discontinuous yield point, such as some carbon-manganese steels at low temperatures. For such materials, the failure assessment curve exhibits a sharp drop for L_r close to 1.0. In the procedure this has been handled rather conservatively by restricting L_r to 1.0. This should be considered as a compromise when applying option 1 to a problem that is actually much better described by the option 2 failure assessment curve. However, for nuclear applications the restriction is not severe but the option 2 type failure assessment curve could be included as an alternative to the option 1 type. In the forth revision of the R6-document [B3], new failure assessment curves are introduced that handles this in a more consistent manner. These new curves may therefore be included in the next edition of this handbook.

Ductile materials, e.g. stainless steel base and weld material, normally show a significant raise of the *J*-resistance curve after initiation. Setting fracture equal to initiation without any account for possible stable crack growth, as in the category 1 type analysis, is rather strict especially if an adequate safety margin is used against fracture. A drawback caused by this is that deformation controlled stresses such as thermal transient and weld residual stresses receive a much too large influence on the fracture assessment since these are not likely to cause unstable crack growth in ductile materials. Therefore, in this edition of the handbook we have included a method similar to the category 2 and 3 type analysis where stable crack growth is accounted for. The amount of ductile tearing Δa must be limited to values where *J* still is likely to characterize the crack-tip conditions (see section B3 below).

B2. Secondary stress

The interaction between secondary and primary stresses on *J* is in the R6-method [B2] handled by the ρ-factor. See Chapter 2.9. ρ is derived by Ainsworth and his original work has been used to derive ρ [B4]. This reduces some of the conservatism in earlier editions of the handbook for low and moderate L_r-values. However, ρ is still restricted to non-negative values. At DNV research work is currently in progress on secondary stresses, i.e. how weld residual stresses contribute to the fracture risk. One drawback with the current deterministic safety evaluation system is that it may overestimate the contribution from secondary stresses for ductile materials. The Swedish Nuclear Power Inspectorate and Det Norske Veritas has therefore started a project that will lead to a quantitative recommendation on how to treat secondary stresses for high L_r-values in a R6 fracture assessment. This recommendation will define new safety factors against fracture described by K_{I} and differentiate between $SF_K^{Primary}$ (relating to primary stresses) and $SF_K^{Secondary}$ (relating to secondary stresses). The results from this project will be incorporated in the next revision of the handbook.

The R6-method prescribes that the elastic stress state is to be used when calculating the stress intensity factor for secondary stresses, K_{I}^s. For high secondary stresses, such as may be induced by thermal transients, the actual *J*-value is overestimated due to plastic relaxation. The problem is further discussed in Ref. [B5], [B6] and [B7]. In the computer program ProSACC a modified version of the method suggested by Budden [B8] has been built in. The secondary stress intensity factor used to determine K_r according to Eq. (2.9) is then calculated by

$$K_I^s = \max(\sqrt{K_1(a)K_2(a)},\ \sqrt{K_1(\overline{a})K_2(\overline{a})}) \quad , \tag{B1}$$

where K_1 and K_2 are stress intensity factors calculated for the elastic and elastic-plastic stress state, respectively. The maximum value of the geometric mean of K_1 and K_2 calculated for the

actual crack size of interest a, and the actual crack size with a plastic zone correction according to Irwin

$$\overline{a} = a + \frac{1}{2\pi\beta}\left(\frac{K_{\mathrm{I}}(a)}{\sigma_Y}\right)^2 \quad , \tag{B2}$$

is to replace K_{I}^s in Eq. (2.9). β is set to 1 for plane stress and to 3 for plane strain. In comparison to Ref. [B8], the elastic stress response to the elastic-plastic strain state has been replaced by the elastic stress state. This makes the method somewhat more easy to use and since the load is strain controlled the two stress states should be close to each other. Eq. (B1) is to be considered as an estimate of an effective secondary stress intensity factor that approximates J for high secondary stresses. Numerical evidence exists that the method works well, see Refs. [B5], [B9] and [B10]. Some minor non-conservatism may exist, partly depending on how stresses are categorised as primary or secondary. However, since the method here is used for safety assessment where a safety margin of the order of 1.4 to 3.2 is used against initiation, this is can be neglected.

B3. Fracture assessment, including stable crack growth

Many materials with high toughness do not fail at a particular value of J [B11]. Rather; these materials display a rising resistance curve, where J increases with crack growth. The traditional measure of fracture toughness, J_{Ic}, is defined near the initiation of stable crack growth. While this initiation toughness provides some information about the fracture behaviour of a ductile material, the entire resistance curve gives a more complete description. The slope of the resistance curve at a given amount of crack extension is indicative of the relative stability of the crack growth; a material with a steep resistance curve is less likely to experience unstable crack propagation. This slope is usually quantified by a dimensionless parameter, tearing modulus,

$$T_R = \frac{E}{\sigma_Y^2}\frac{dJ_R}{da} \quad . \tag{B3}$$

The condition that governs the stability of crack growth is that instability occurs when the driving force is tangent to the resistance curve. It is convenient to express this driving force in terms of an applied tearing modulus,

$$T_{app} = \frac{E}{\sigma_Y^2}\left(\frac{dJ}{da}\right)_{\Delta_{total}} \quad , \tag{B4}$$

where Δ_{total} is the total displacement of the system. This displacement consists of terms related to applied displacements and to applied forces. However, load control is usually less stable than displacement control. Since the structural stiffness / compliance are unknown in ProSACC [B1], it is therefore assumed that load control is dominating and the non-critical region is defined by (see Fig. B1)

$$J = J_R \quad , \tag{B5}$$

$$T_{app} \le T_R \quad , \tag{B6}$$

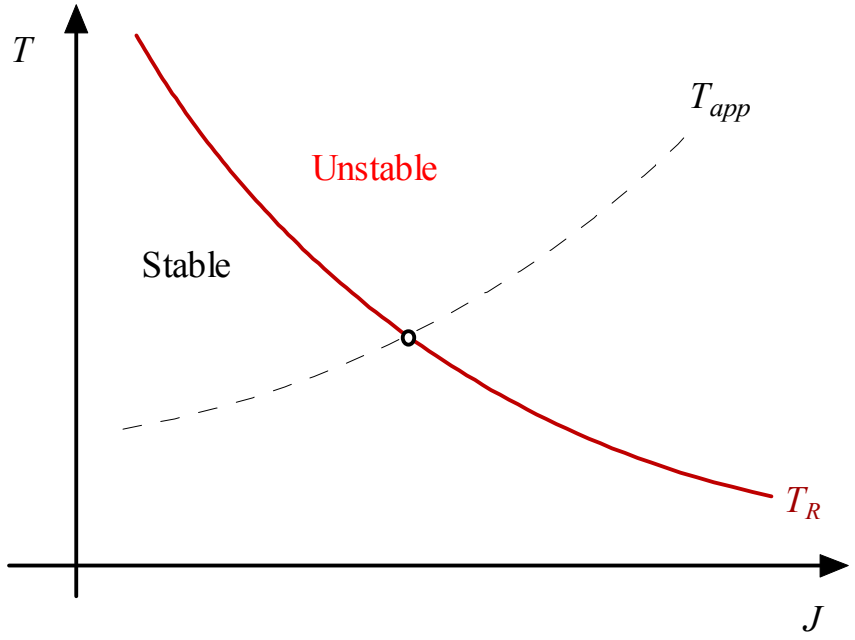

Figure B1. Schematic stability assessment diagram [B11].

B4. Safety assessment

The second edition of the handbook contained a safety assessment system based on partial coefficients. The nominal values of fracture toughness and yield strength were replaced with design quantities according to

$$K_{cr}^{d} = \frac{K_{cr}}{\gamma_m^k} \quad , \tag{B7}$$

$$\sigma_Y^d = \frac{\sigma_Y}{\gamma_m^y} \quad , \tag{B8}$$

where γ_m^k and γ_m^y are so-called partial coefficients. The assessment was then performed with the design quantities instead of the nominal values. The size of the partial coefficients was chosen to give the same overall safety margins against fracture initiation and plastic collapse as applied in ASME Sect. XI and III. For normal and upset conditions, typical values of γ_m^k and γ_m^y were $\sqrt{10}$ and 1.5, respectively.

In the failure assessment diagram γ_m^k and γ_m^y move the assessment point (L_r, K_r) to the right with a factor γ_m^y and upwards with a factor γ_m^k. Since the failure assessment curve drops for higher L_r-values a non-uniform safety margin to fracture initiation is obtained depending on the value of L_r. This can be further quantified by looking at the criterion for fracture initiation based on the *J*-integral [B12].

$$J = J_{\mathrm{Ic}} \quad . \tag{B9}$$

The R6 revision 3, option 1 type failure assessment curve gives the following expressions for *J* and J_{Ic}.

$$J = \frac{(1-\nu^2)K_{\mathrm{I}}^2}{E} \frac{1}{[f_{R6}(L_r) - \rho]^2} \quad , \tag{B10}$$

$$J_{\mathrm{Ic}} = \frac{(1-\nu^2)K_{cr}^2}{E} \quad , \tag{B11}$$

where

$$f_{R6} = (1 - 0.14L_r^2)[0.3 + 0.7\exp(-0.65L_r^6)] \quad . \tag{B12}$$

With the partial coefficients γ_m^k and γ_m^y applied, the criterion becomes

$$J = J_{acc} \quad , \tag{B13}$$

where, with the same definition of *J* as above,

$$J_{acc} = \frac{(1-\nu^2)K_{cr}^2}{(\gamma_m^k)^2 E} \frac{[f_{R6}(\gamma_m^y L_r) - \rho]^2}{[f_{R6}(L_r) - \rho]^2} \quad . \tag{B14}$$

The safety margin against fracture initiation is then given by

$$SF = \frac{J_{Ic}}{J_{acc}} = (\gamma_m^k)^2 \frac{[f_{R6}(L_r) - \rho]^2}{[f_{R6}(\gamma_m^y L_r) - \rho]^2} \quad . \tag{B15}$$

The result is shown in Fig. B2 for the case $\gamma_m^k = \sqrt{10}$, $\gamma_m^y = 1.5$ and $\rho = 0$. For low values of L_r, the desired safety margin becomes 10 to *J*-controlled initiation as in accordance with the flaw assessment procedure in ASME 1995, Sect. XI, App. A. But for L_r-values exceeding 0.6, the margin increases dramatically with a maximum peak of about 90.

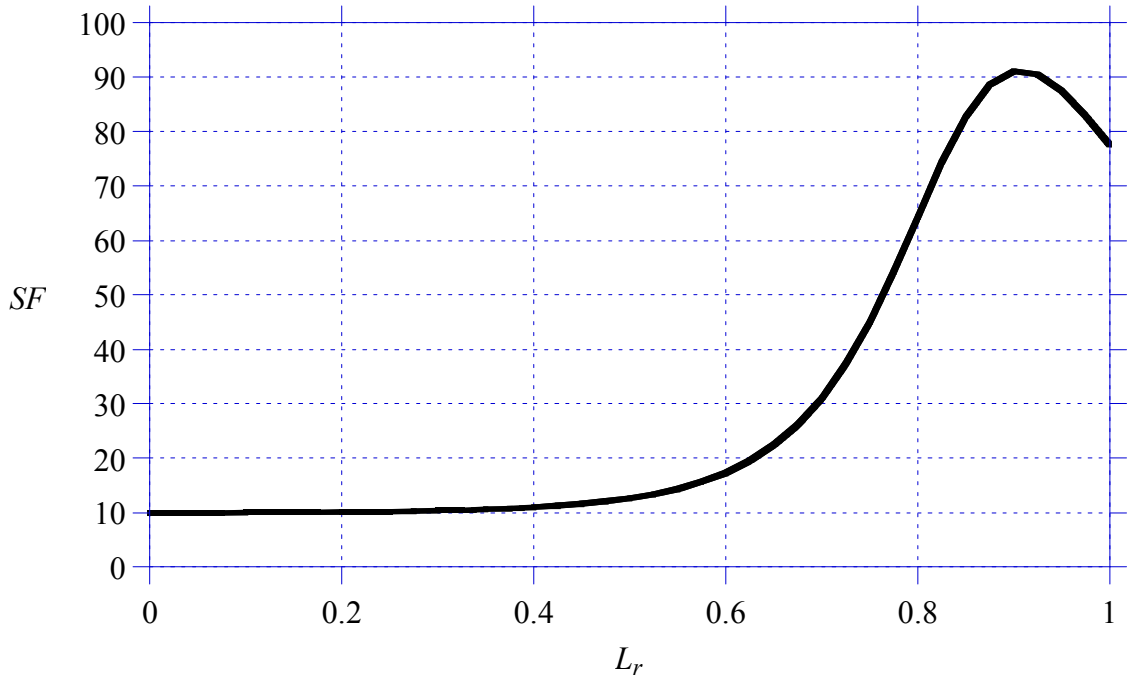

Fig. B2. Increase of safety margin for initiation due to shape of R6 revision 3, option 1 type failure assessment curve.

The above behaviour seemed much too conservative in comparison to the flaw assessment procedure in ASME 1995, Sect. XI, App. A. The presented example corresponds to a maximum safety factor of about 9.5 instead of 3.16 as in ASME 1995, Sect. XI, App. A. For that reason a new safety assessment procedure was developed as described in Ref. [B12] and presented in the third edition of the handbook. The new safety assessment procedure gave a uniform safety margin to fracture initiation.

As pointed out in Ref. [B12], we still believe a safety assessment procedure based on partial coefficients to be a more preferable one as long as the partial coefficients reflect the actual scatter of each input quantity. In the old safety assessment procedure (the second edition of the handbook), the overall safety margins were taken from ASME 1995, Sect. XI and III and basically only applied to a few input quantities, here the material properties. Since the overall margins are quite large the uncertainty of the material properties were exaggerated which gave the effect shown above. To resolve this, a project has recently been finalised at DNV to develop a probabilistic safety assessment procedure which is included in the software ProSACC. One outcome of this work has been the possibility to use a procedure based on several interacting partial coefficients for defect size, loads, material properties etc. where the value of each partial coefficient is a function of the uncertainty of its corresponding input quantity.

B5. Weld residual stresses

Appendix R contains guidelines on weld residual stresses. The appendix has been revised and for instance new recommendations for residual stresses for bimetallic butt welded pipes based on numerical calculations [B13-B14] have been included.

B6. Stress intensity factor and limit load solutions

Appendix K and L containing stress intensity factor and limit load solutions have been extensively revised. The objective has been to improve the accuracy of the solutions and to remove unnecessary conservatism in some of the solutions.

For finite surface cracks in plates a new stress intensity factor solution for large l/a-ratios has been included [B15]. Also, a new limit load solution is introduced [B16]. This solution removes the unnecessary conservatism in the previous solution and it is also valid for larger a/t-ratios.

For finite axial surface cracks in cylinders a new limit load solution is introduced [B16]. This solution removes the unnecessary conservatism in the previous solution and it is also valid for larger a/t-ratios.

For axial through-thickness cracks in cylinders a new stress intensity factor solution for large R_i/t-ratios has been included [B17]. This solution is also valid for more complex stress distributions.

For part circumferential surface cracks in cylinders a new stress intensity factor solution for both small and large R_i/t-ratios has been included [B15].

For circumferential through-thickness cracks in cylinders a new stress intensity factor solution for large R_i / t-ratios has been included [B17]. This solution is also valid for more complex stress distributions.

Part circumferential surface cracks in bars is now included as a new geometry [B18] in revision 4 of the handbook.

B7. Fit of stress distribution for stress intensity factor calculation

Beginning with the third edition of the handbook, stress intensity factor solutions are included for a polynomial stress distribution through the thickness up to the order of 5. A problem then arises how the actual stress distribution is fitted to a polynomial to estimate K_I as accurate as possible. Depending on type of situation, the following alternatives are suggested:

a) For a smooth continuous stress distribution, the actual stress distribution over the extension of the crack is least-square fitted to a polynomial with an order within the range available. The order of the polynomial that gives the agreement with the actual stress is chosen.

b) For a discontinuous stress distribution such as may arise if dissimilar materials through the thickness are present, an accurate least-square polynomial fit may not be possible since the order of the polynomial is restricted. Instead a linearization is recommended where the linear stress distribution is given the same resulting normal force and moment as the actual stress distribution over the extension of the crack.

The PC-program ProSACC assists the user to select the best alternative. The program displays a graph where the actual and fitted stress distributions are shown. By testing different alternatives and looking at the outcome on the graph the user can find out which alternative to select. When in doubt the fitting procedure that gives the most conservative result in the assessment should be used.

B8. Probabilistic analysis

Verification has been carried out, using the probabilistic computer program STAR6 from Nuclear Electric [B19] and the deterministic program SACC from Det Norske Veritas AB [B20]. This is presented in section B8.1. Another important aspect in the development of a new probabilistic flaw evaluation procedure is to compare the behaviour against other published procedures and software. Such a benchmark is presented in section B8.2.

The statistical distribution used for an input parameter has an important impact on the resulting failure probabilities. This is especially true when calculating small failure probabilities. Another

important factor is the data used in the probabilistic analysis. Examples on distributions and data to be used are discussed in section B8.3 [B21-B22].

B8.1 Verification

The procedure and program ProSACC has been verified using three different verification procedures.

- Firstly, a general verification of ProSACC was made [B21-B22] and presented in section B8.1.1.
- Secondly, a specific verification, using input data relevant to risk based inspection studies of a reactor pressure vessel, was made and presented in section B8.1.2.
- Finally, a verification of the assumptions for the POD-model was made and presented in section B8.1.3.

B8.1.1 General verification of ProSACC

To verify the procedure and the program ProSACC, a comparison was made against two different computer programs:

- STAR6 from Nuclear Electric [B19], which calculates the probability of failure using a combination of analytical and numerical integration.
- SACC from SAQ Kontroll AB / Det Norske Veritas [B20], used to validate the deterministic parts of ProSACC.

Also, a comparison among the different numerical algorithms within ProSACC was made.

Deterministic validation

To check the deterministic parts of ProSACC, a comparison was made against the computer program SACC from SAQ Kontroll AB [B20]. SACC contains several options and for this validation a fracture assessment procedure based on the R6-method was used.

Validation with normally distributed parameters

To check the probabilistic parts of ProSACC, a comparison was made against the computer program STAR6 from Nuclear Electric [B19]. First a validation using normally distributed parameters was made.

Two different cases were investigated:

- P_F as a function of primary membrane stress, using two different values of standard deviation for the dominating parameter sizing probability.
- P_F as a function of standard deviation for the dominating parameter sizing probability, using two different values of primary membrane stress.

Probability of failure as a function of primary membrane stress

The following data was used for this validation:

- Probability of failure, defect size given by NDT/NDE was analysed, using the following algorithms:
  - First-Order Reliability Method (FORM).
  - Simple Monte Carlo Simulation (MCS).
  - Monte Carlo Simulation with Importance Sampling (MCS-IS), using a special MCS-IS version of ProSACC.
- The STAR6 geometry ”extended edge defect in a plate under tension” was chosen (thickness t = 103 mm).
- Fracture toughness, mean = 200 MPa$\sqrt{m}$ and standard deviation = 10 MPa$\sqrt{m}$ [B21].
- Yield strength, mean = 350 MPa and standard deviation = 30 MPa [B21].
- Ultimate tensile strength, mean = 500 MPa and standard deviation = 30 MPa [B21].
- Defect size given by NDT/NDE, for two different NDE procedures [B23]. The data given is from component 1 in [B23]:
  - An advanced NDE procedure, mean = 26.0 mm and standard deviation = 6.5 mm.
  - A bad NDE procedure, mean = 30.2 mm and standard deviation = 18.1 mm.

In figure B3, one can find the result using an advanced NDE procedure.

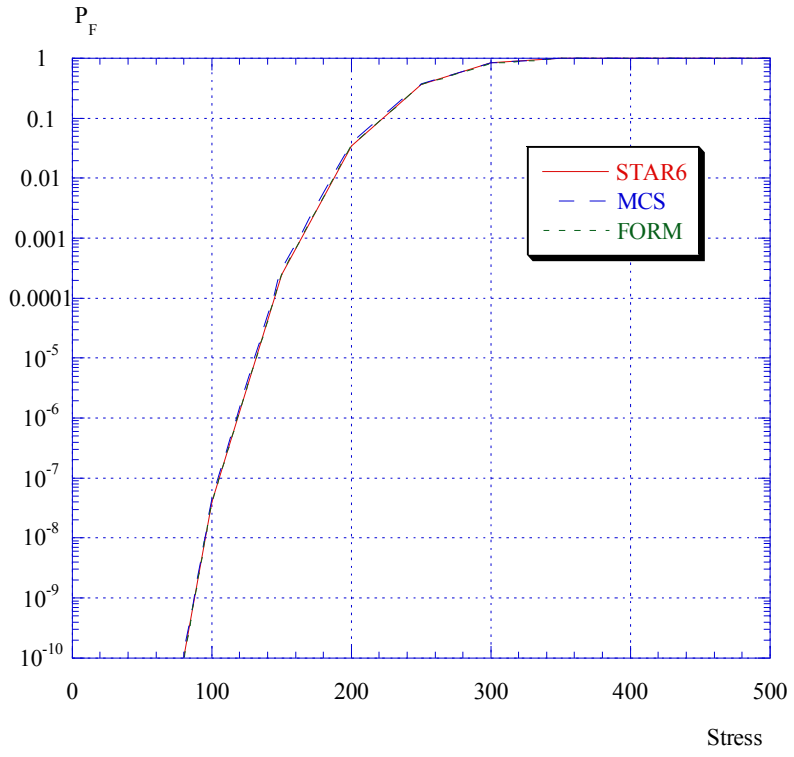

Figure B3. Probability of failure as a function of primary membrane stress, using an advanced NDE procedure.

For both cases (the result using a bad NDE procedure is not shown), there were an excellent agreement between ProSACC and STAR6.

Probability of failure as a function of sizing standard deviation

The main data used were the same as in the example above. The difference was that this time one calculated the probability of failure as a function of standard deviation for the dominating parameter sizing probability, using two different values of primary membrane stress (150 and 200 MPa). The results can be found in figure B4 below.

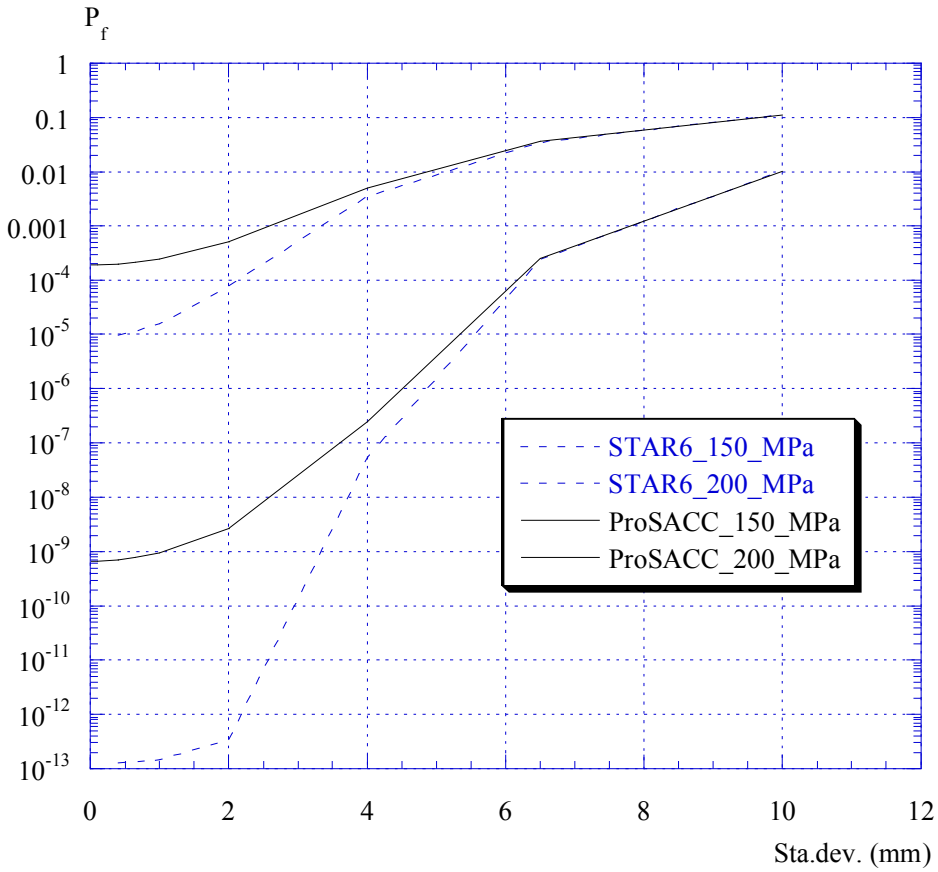

Figure B4. Probability of failure as a function of standard deviation for the dominating parameter sizing probability, using two different values of primary membrane stress.

As shown in figure B4, the agreement between ProSACC and STAR6 is very bad for small values of sizing standard deviation. After investigating this difference, it was shown that the results from ProSACC were correct, and that the algorithms used in STAR6 were not intended to work for a general problem, when the standard deviation is either ”small” or ”large”.

Validation with non-normally distributed parameters

The main data used were the same as above. The difference was that this time one calculated the probability of failure using an exponential sizing probability (with two different mean values). The results can be found in figure B5 below.

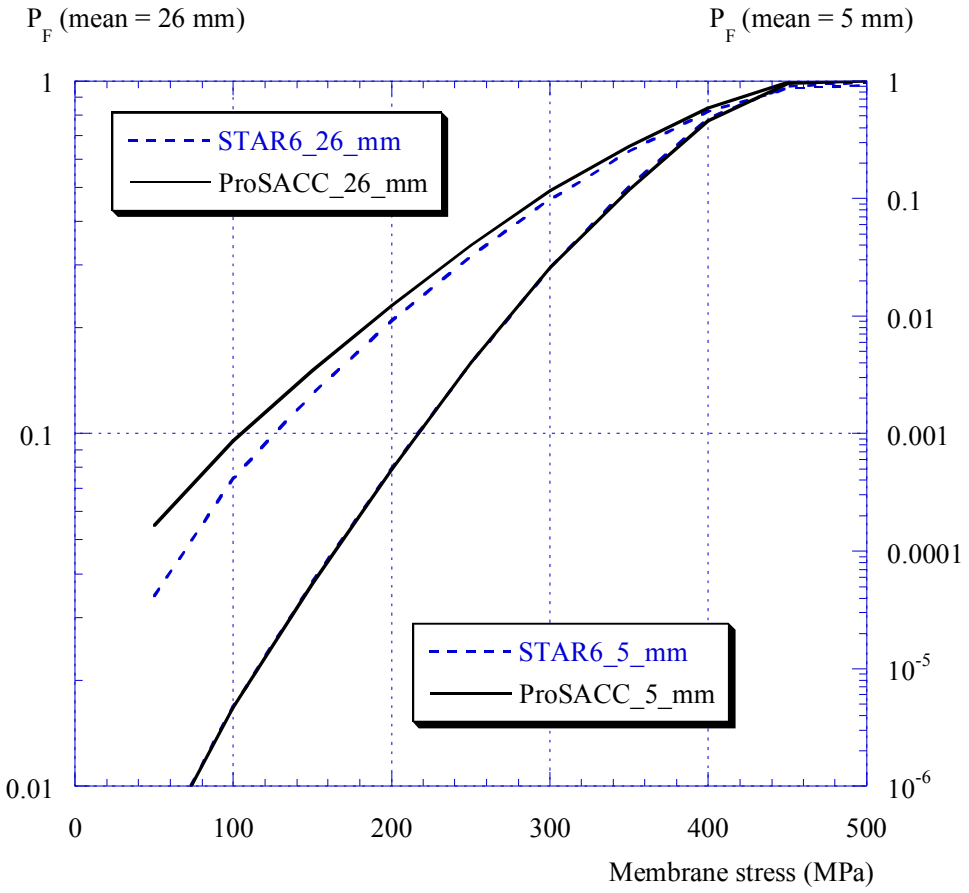

Figure B5. Probability of failure using an exponential sizing probability, with two different mean values.

As shown in figure B5, the agreement between ProSACC and STAR6 is quite bad for the case with a large mean value (and also a large standard deviation). After investigating this difference, it was shown that the results from ProSACC were correct, and that the algorithms used in STAR6 were not intended to work for a general problem, when the standard deviation is either "small" or "large".

Validation of a case with secondary stresses

The main data used was the same as above. The difference was that this time one calculated the probability of failure as a function of the applied secondary membrane stress (using a constant primary membrane stress equal to 100 MPa). The results can be found in figure B6 below.

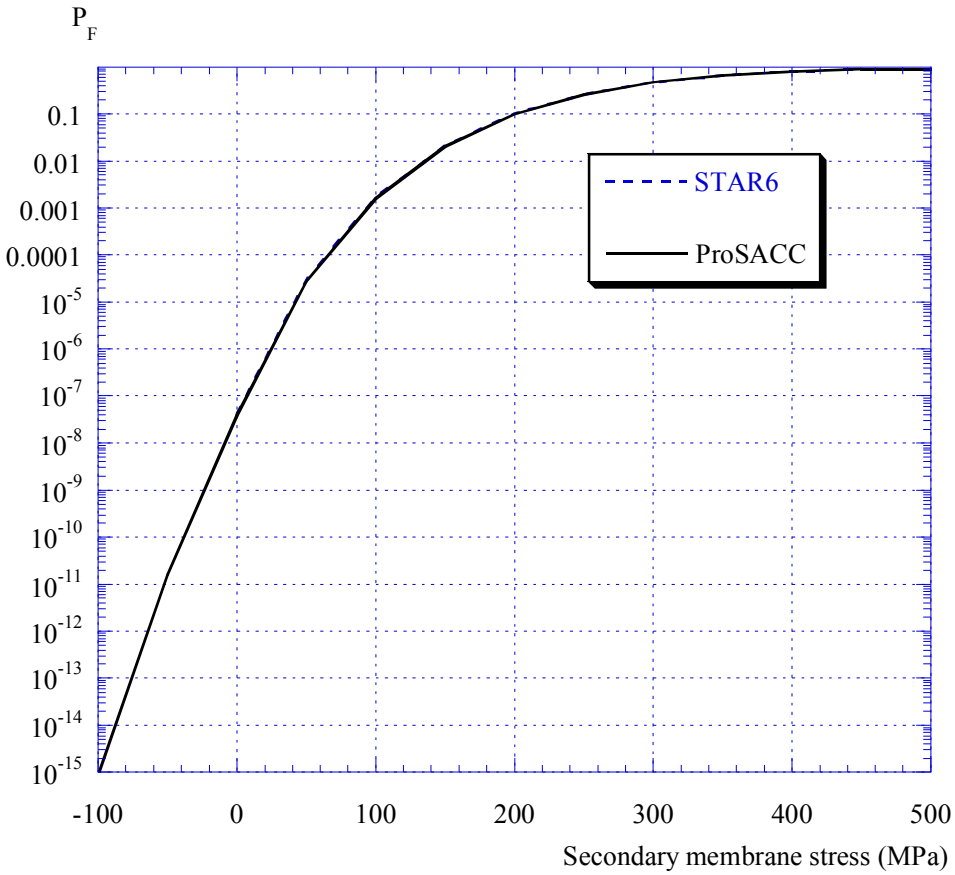

Figure B6. Probability of failure as a function of applied secondary membrane stress.

As shown in figure B6, the agreement between ProSACC and STAR6 is excellent in this case, using a simple ρ definition for the validation exercise only.

B8.1.2 Verification using input data relevant to RBI studies of a reactor pressure vessel

The verification in section B8.1.1 showed that the results from ProSACC, in general, are very accurate. A specific verification, using input data relevant to risk based inspection studies of a reactor pressure vessel, is also presented below.

In this verification a comparison of the results using FORM (an approximate method) and MCS (an exact method, when using sufficient number of simulations) is made. The reason for this verification is that in the RBI studies of different RPV`s, only FORM were used. The weld

W1111 from the Ringhals 1 RPV was chosen (Weld ID = RW1111_1_F1) [B24], using an exponential defect depth distribution and with no in-service inspection event taken into account (when calculating the probability of failure). The results are summarised in Table B1, using different mean values of defect depth μ_a.

Table B1. Verification using input data relevant to RBI studies of a reactor pressure vessel.

μ_a [mm]	P_F (FORM)	P_F (MCS, $N = 10^5$)	P_F (MCS, $N = 10^7$)
5.0	$4.29 \cdot 10^{-8}$	0.0	0.0
6.3	$1.37 \cdot 10^{-6}$	0.0	$1.80 \cdot 10^{-6}$
7.5	$1.17 \cdot 10^{-5}$	$1.00 \cdot 10^{-5}$	$1.20 \cdot 10^{-5}$
10.0	$1.96 \cdot 10^{-4}$	$1.90 \cdot 10^{-4}$	$2.02 \cdot 10^{-4}$
12.5	$1.07 \cdot 10^{-3}$	$0.91 \cdot 10^{-3}$	$1.12 \cdot 10^{-3}$
15.0	$3.33 \cdot 10^{-3}$	$3.29 \cdot 10^{-3}$	$3.37 \cdot 10^{-3}$
17.5	$7.50 \cdot 10^{-3}$	$7.84 \cdot 10^{-3}$	$7.51 \cdot 10^{-3}$
20.0	$1.38 \cdot 10^{-2}$	$1.42 \cdot 10^{-2}$	$1.38 \cdot 10^{-2}$

As shown in table B1, the agreement between FORM and MCS is excellent when a sufficiently large number of simulations are used. P_F (MCS) = 0.0 indicates that more simulations are needed to get an accurate estimate of the failure probability.

B8.1.3 Verification of the assumptions for the POD-model in ProSACC

To simplify the calculation of the probability of failure when a defect is not detected by NDT/NDE (using FORM) a simplified expression (see Eq. (P28)) is used instead of Eq. (P27). How this influences the resulting failure probabilities is shown in figures B7 to B9. The POD-data is taken from section B8.3.4, and the analysis using Eq. (P28) is done by Monte Carlo simulation.

The following data was used for this verification:

- An exponential defect depth distribution was chosen (mean = 6.3 mm).
- POD-data from three different UT procedures was used (Low effectiveness UT, Good practice UT and Advanced UT).

In figures B7 to B9 the probability of failure before an inspection (*i. e.* no inspection) are given on the x-axis and the probability of failure after an inspection not resulting in any defect detection are given on the y-axis.

The resulting most probable point of failure, with respect to crack depth, was between 1 mm and 80 mm (this extended range covered most of the practical cases in the RBI study [B24]).

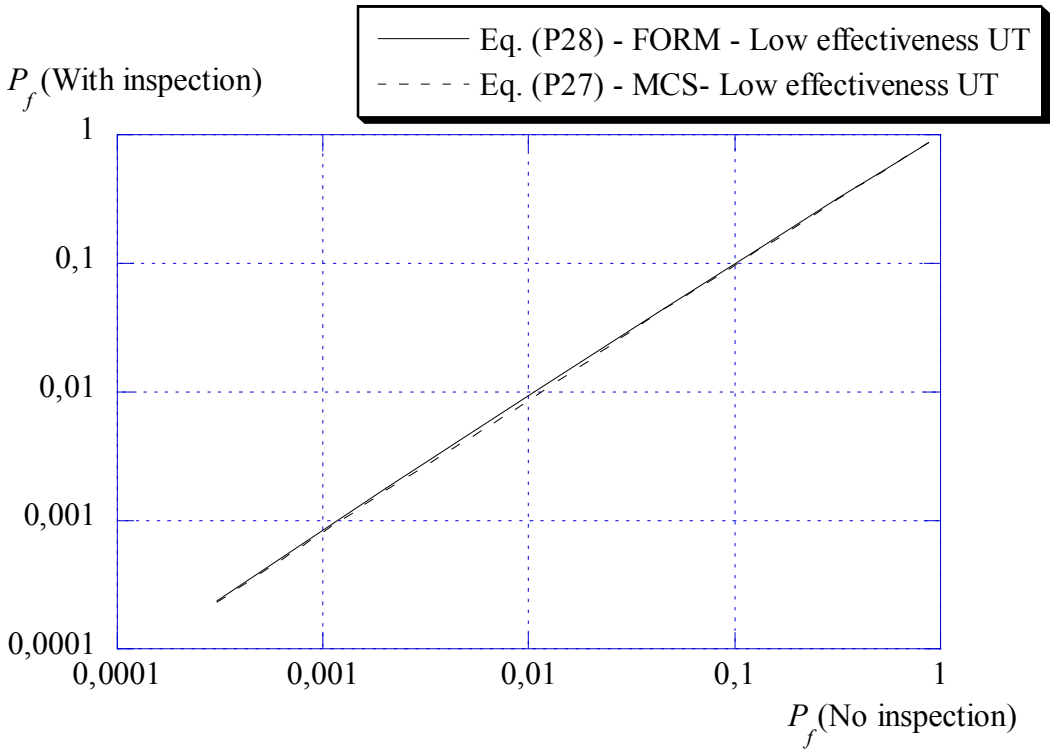

Figure B7. Probability of failure, using different assumptions in the analysis and using a low effectiveness UT procedure.

As can be seen in Fig. B7, there is almost no difference between the results using the two methods to calculate the probability of failure. This has to do with the fact that that there is no real benefit from using a low effectiveness UT procedure.

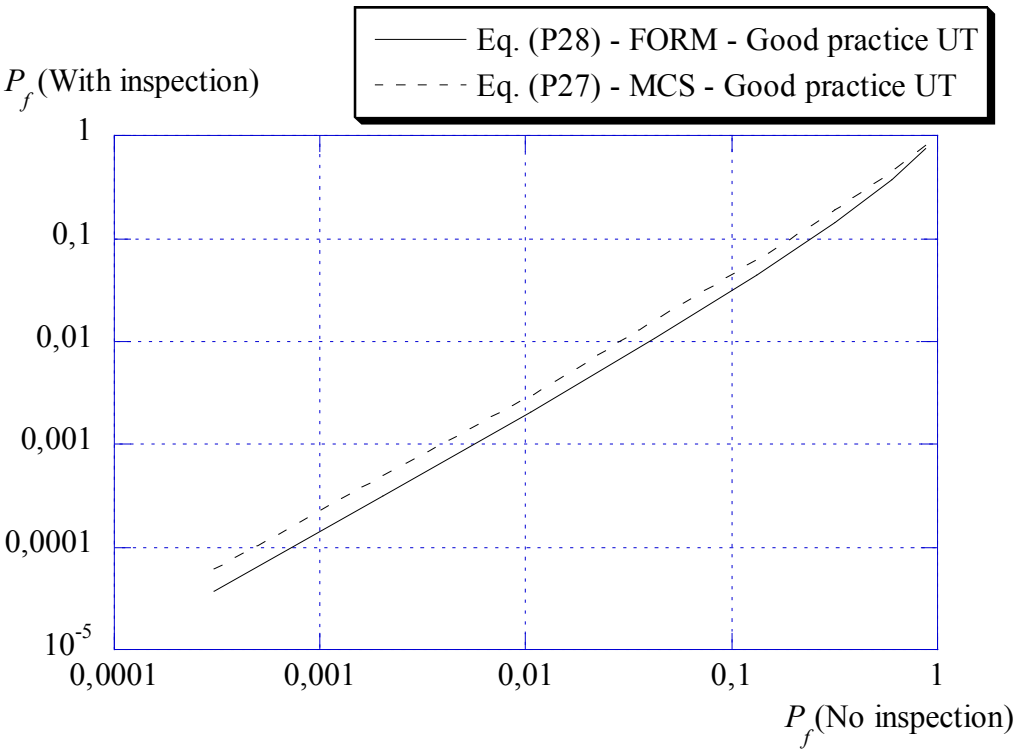

Figure B8. Probability of failure, using different assumptions in the analysis and using a good practice UT procedure.

As can be seen in Fig. B8, there is a small difference between the results using the two methods to calculate the probability of failure (using a good practice UT procedure). This difference, however, is consistent for all cases in a RBI study and should therefore be of no importance when comparing failure probabilities for different regions (welds) in a reactor pressure vessel.

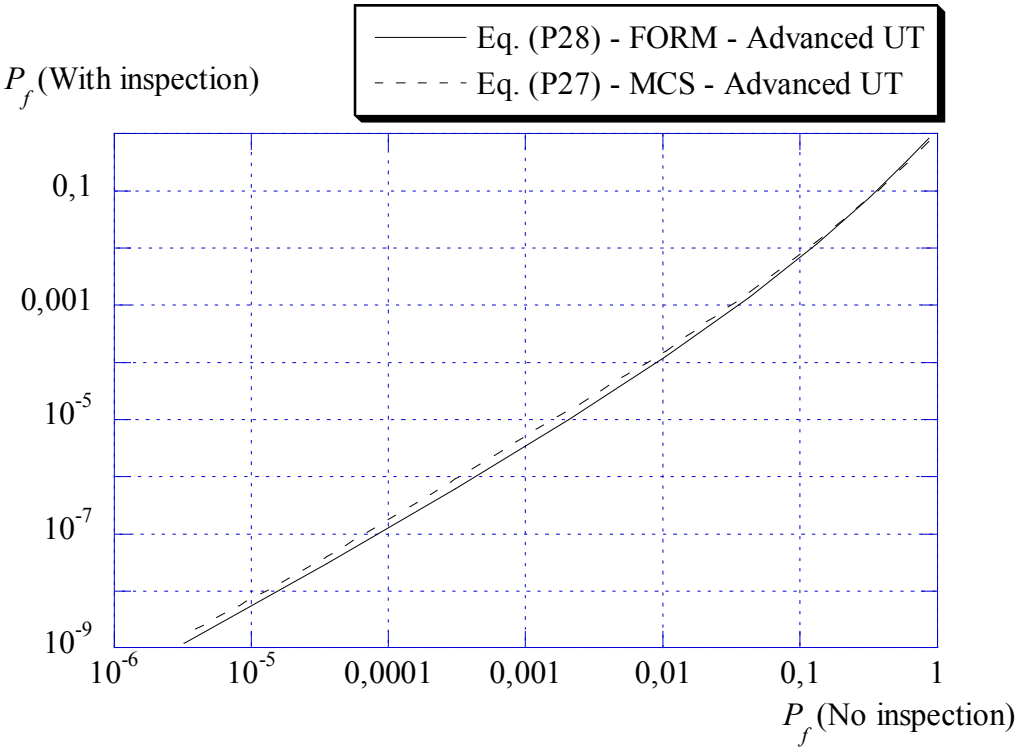

Figure B9. Probability of failure, using different assumptions in the analysis and using an advanced UT procedure.

As can be seen in Fig. B9, there is almost no difference between the results using the two methods to calculate the probability of failure (when using an advanced UT procedure).

This verification (as presented in Fig. B7 to Fig. B9) shows that the error in using a simplified POD model is insignificant when used to compare different regions (welds) in a reactor pressure vessel.

B8.2 Benchmarking probabilistic procedures and software

One important aspect in the development of a new probabilistic flaw evaluation procedure is to compare the behaviour against other published procedures and software. The objective of such a benchmark study could be to:

- Review probabilistic procedures and associated software in terms of main features, capabilities and limitations.
- Benchmark probabilistic procedures and associated software by performing a comprehensive sensitivity study and compare the results.
- Investigate the reasons for differences in results from the benchmark study and identify strengths and weaknesses of the probabilistic procedures and associated software.

We are currently (beginning of 2004) participating in a benchmark study within the Fifth Framework of the European Atomic Energy Community [B25]. The title of the project is "Nuclear Risk-Based Inspection Methodology for passive components (NURBIM)". We are also planning to participate in the proposed OECD benchmark study called "PROSIR - Probabilistic Structural Integrity of a PWR Reactor Pressure Vessel" [B26]. The first results from these studies will be published later this year (2004).

B8.3 Distribution and data to be used in a probabilistic analysis

The statistical distribution used for an input parameter has an important impact on the resulting failure probabilities. This is especially true when calculating small failure probabilities. Another important factor is the data used in the probabilistic analysis. Examples on distributions and data to be used are discussed below [B21-B22].

B8.3.1 Fracture toughness

The process of crack growth depends on the microstructural conditions in the crack tip vicinity. These are to some extent of random nature. Depending on the particular mechanism of crack growth, the random element is more or less apparent. Thus for instance we can be expecting that crack growth due to cleavage exhibit a prominently random character. This is also found in experimentation. Ductile crack growth on the other hand is of a more deterministic nature. The difference is due to the fact that cleavage fracture depends on the conditions in very small region around a single point while the ductile process will depend more on the average properties.

The normal, lognormal and Weibull distributions are most often used to describe the variations in fracture toughness [B3, B21-B22, B27-B28]. The fracture toughness data employed should, whenever possible, be for the actual material being considered. A disadvantage of the use of a normal distribution is that the algorithms used in MCS and FORM/SORM, may result in negative values of fracture toughness. Both the lognormal and Weibull distributions have the correct property that only non-negative values are permitted and are therefore more suitable distributions to be used for fracture toughness. The choice of distribution is then determined by whichever provides the better fit to experimental data. Where some uncertainty exists, a sensitivity analysis is recommended [B3, B21-B22, B27].

However, fairly little information is available for the random distribution of fracture toughness and related properties. In the lower shelf and transition region Wallin [B29, B30] and others have argued for the use of Weibull type distributions. In the wholly ductile temperature region a Weibull distribution is not appropriate. The results in [B31] instead suggest a lognormal distribution. Wallin [B30] indicates that a normal distribution provides a good fit to experimental J_R-data.

If no experimental data is available, the following data may be used [B27, B30, B32]:

- In the lower shelf and transition region: $\sigma_{K_{Ic}} \approx 0,2 \cdot \mu_{K_{Ic}} - 0,3 \cdot \mu_{K_{Ic}}$
- In the wholly ductile temperature region: $\sigma_{K_{Ic}} \approx 0,05 \cdot \mu_{K_{Ic}} - 0,1 \cdot \mu_{K_{Ic}}$
- In the wholly ductile temperature region (using correlated Charpy data): $\sigma_{K_{Ic}} < 0,1 \cdot \mu_{K_{Ic}}$

B8.3.2 Yield strength and ultimate tensile strength

The distributions for fracture toughness (i. e. the normal, lognormal and Weibull distributions), are also most often used to characterise the yield strength and ultimate tensile strength [B21-B22, B27].

The yield limit of a material can for instance be regarded as the sum of the yield limit of many grains and it is thus reasonable to assume the macroscopic limit to be normally distributed. Using an extensive data set from the English Health and Safety Executive materials database, to fit the yield strength to normal, lognormal and Weibull distributions, it was found that the lognormal distribution gave the best fit to most of the cases considered [B33]. With the data given, a typical standard deviation of 28 MPa could be evaluated [B22].

If only measured mean values for yield strength (μ_{σ_Y}) and ultimate tensile strength (μ_{σ_U}) are available, the following standard deviation values may be used [B30]:

- Yield strength: $\sigma_{\sigma_Y} = 0,03 \cdot \mu_{\sigma_Y}$
- Ultimate tensile strength: $\sigma_{\sigma_U} = 0,05 \cdot \mu_{\sigma_U}$

If only standardised minimum values for yield strength (R_e) and ultimate tensile strength (R_m) are available, the following data may be used [B30]:

- Yield strength: $\mu_{\sigma_Y} = R_e + 70$ MPa and $\sigma_{\sigma_Y} = 30$ MPa
- Ultimate tensile strength: $\mu_{\sigma_U} = R_m + 70$ MPa and $\sigma_{\sigma_U} = 30$ MPa

B8.3.3 Defect size given by NDT/NDE

NDE data generally results from the application of an inspection procedure based on several techniques, on the skill of the operator, on decision steps such as recording or not, geometric indication or not, false call or not. The size of a recorded defect is usually established by the operator, often not following rigorous reasoning that could be documented. The NDE data used by the structural integrity engineer will always be the result of a complex combination of various information and decisions taken during the process of generating that information [B23]. Most studies has then come to the conclusion that it is very common that small defects are overestimated in size and large defects are underestimated in size [B33-B34].

The distribution most often used is the normal distribution, which could be applied for analyses where a single defect is either known or postulated to exist in a weld [B3, B33].

It is impossible to give general recommendations on data to be used for a specific case. However, in table B2 below, some typical sizing error values from [B23] are summarised.

Table B2. Typical values of defect sizing error (UT = Ultrasonic testing) [B23].

Component	Material	NDE procedure	Sizing error (σ_a)
Plate $t > 75$ mm $\mu_a = 0.4 \cdot t$	Ferritic steel	Advanced UT	5 mm
		Good practice UT	12 mm
		Low effectiveness UT	15 mm
Piping ($D > 250$ mm) 30 mm $< t <$ 75 mm $\mu_a = 0.4 \cdot t$	Ferritic steel	Advanced UT	5 mm
		Good practice UT	15 mm
		Low effectiveness UT	15 mm
Piping ($D > 250$ mm) 10 mm $< t <$ 30 mm $\mu_a = 0.4 \cdot t$	Ferritic steel	Advanced UT	3 mm
		Good practice UT	5 mm
		Low effectiveness UT	10 mm
Piping ($D < 250$ mm) 5 mm $< t <$ 30 mm $\mu_a = 0.4 \cdot t$	Ferritic steel	Advanced UT	3 mm
		Good practice UT	5 mm
		Low effectiveness UT	10 mm
Piping ($D > 250$ mm) $t > 30$ mm $\mu_a = 0.4 \cdot t$	Wrought austenitic steel	Advanced UT	5 mm
		Good practice UT	5 mm
		Low effectiveness UT	7 mm
Piping ($D < 250$ mm) $t < 30$ mm $\mu_a = 0.4 \cdot t$	Wrought austenitic steel	Advanced UT	2 mm
		Good practice UT	3 mm
		Low effectiveness UT	5 mm

B8.3.4 Defect not detected by NDT/NDE

As no NDT device is able to detect all defects in the structural weld, there is always a possibility that a defect will remain in the component following inspection and repair. The probability of this occurring depends on many parameters, such as fabrication techniques, NDT methods and requirements, reliability of the methods and the operators etc [B21-B22, B33]. The probability of not detecting a defect will of course decrease as the defect size is increased and it will be near unity for very small defects, whereas it approaches zero with increase in crack size (using a sufficiently advanced procedure).

It is quite difficult to give general recommendations on data to be used for a specific case. However, in table B3 below, some typical detection probability values from the European SINTAP project [B23] are summarised.

Table B3. Typical values of detection probability (using different defect depths) [B23].

Component	Material	NDE procedure	Detection probability			
			$a = 0{,}05 \cdot t$	$a = 0{,}1 \cdot t$	$a = 0{,}4 \cdot t$	$a = 1{,}0 \cdot t$
Plate $t > 75$ mm	Ferritic steel	Advanced UT	0,5	0,95	1,0	1,0
		Good practice UT	0,5	0,7	0,8	0,95
		Low effectiveness UT	0,0	0,1	0,25	0,4
Piping ($D > 250$ mm) 30 mm $< t <$ 75 mm	Ferritic steel	Advanced UT	0,8	0,95	1,0	1,0
		Good practice UT	0,8	0,9	1,0	1,0
		Low effectiveness UT	0,0	0,2	0,4	0,6
Piping ($D > 250$ mm) 10 mm $< t <$ 30 mm	Ferritic steel	Advanced UT	0,7	0,95	1,0	1,0
		Good practice UT	0,6	0,9	1,0	1,0
		Low effectiveness UT	0,0	0,4	0,6	0,8
Piping ($D < 250$ mm) 5 mm $< t <$ 30 mm	Ferritic steel	Advanced UT	0,5	0,9	1,0	1,0
		Good practice UT	0,4	0,8	0,95	1,0
		Low effectiveness UT	0,0	0,3	0,5	0,8
Piping ($D > 250$ mm) $t > 30$ mm	Wrought austenitic steel	Advanced UT	0,5	0,9	1,0	1,0
		Good practice UT	0,6	0,8	0,9	0,95
		Low effectiveness UT	0,1	0,2	0,4	0,8
Piping ($D < 250$ mm) $t < 30$ mm	Wrought austenitic steel	Advanced UT	0,3	0,95	1,0	1,0
		Good practice UT	0,0	0,7	0,95	1,0
		Low effectiveness UT	0,0	0,5	0,7	0,8

As an example a POD-curve (distribution) for "Low effectiveness UT" corresponding to the lower bound performance among all teams that were evaluated in a program to assess inspection efficiency for piping [B35] is shown in Figure B10 (using Eq. (P14) with $c_1 = 0,240$ and

$c_2 = 1,485$). The POD-curve of "Good practice UT" corresponding to that of a team with over average performance ($c_1 = 1,526$ and $c_2 = 0,533$), and a POD-curve of the "Advanced UT" corresponding to the performance that could be achieved with improved procedures [B35] ($c_1 = 3,630$ and $c_2 = 1,106$) are also shown in Figure B10. For qualified inspection procedures used in Sweden, the POD-curve is assumed to correspond to the curve for a "Good practice UT".

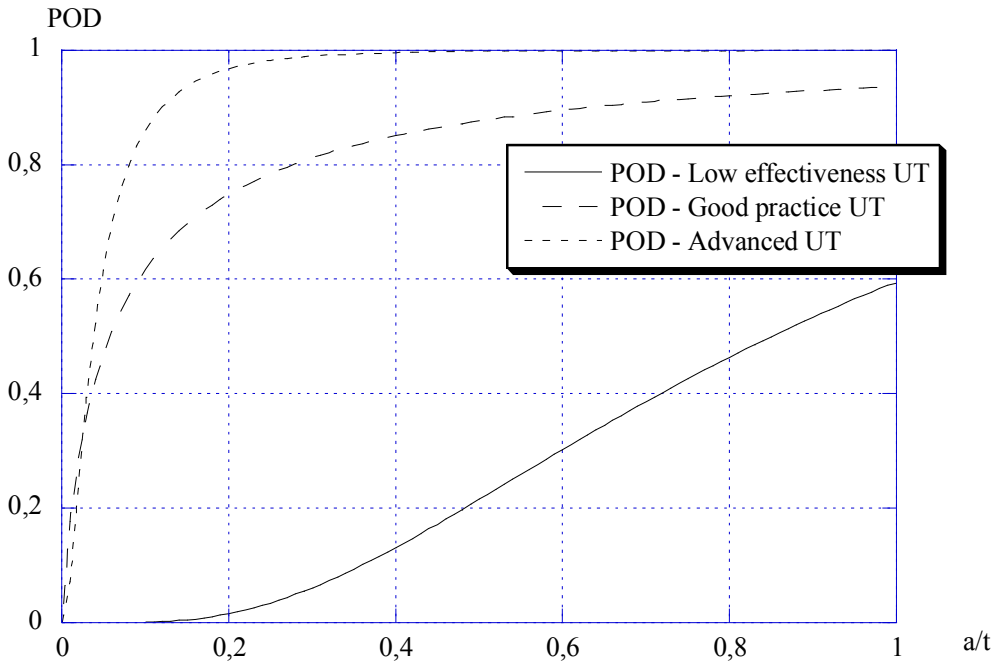

Figure B10. The probability of detection for different qualities of the inspection equipment and procedures, as a function of crack depth *a* relative to section thickness *t*.

The detection probability for thick plates (> 75 mm) of ferritic steel were assessed within the project SINTAP (table B3) [B23], and the curve for "Good practice UT" in Figure B10 is a good approximation of the POD for these thick ferritic plates.

B8.3.5 Defect distribution

Defect depth distributions are quite difficult to estimate reliably for any given application. This is because very few defects of significance have been observed by NDE of plain welds in pressure vessels or critical structural components. Therefore, whenever possible, sensitivity studies should be performed as part of an assessment to investigate the dependency on the assumed defect distribution [B3].

The defect depth distributions most often used are the lognormal, Weibull and exponential distributions [B3, B27, B33]. The so-called Marshall distribution, commonly used within the nuclear industry, is a particular case of the exponential distribution.

Ongoing research regarding a suitable defect distribution for thick-section butt welds is likely to eliminate some of the anomalies in using the Marshall distribution for these welds (this distribution is based on ultrasonic data acquired in the early 1970s). Using modern ultrasonic and destructive inspection techniques shows a significantly higher probability of defects of depths less than ~10 mm and lower probability of larger defects [B36] (see figure B11). Using an expert system [B37] to model different factors that influence the likelihood and size of defects mainly comes to the same conclusion (an example is shown in figure B12).

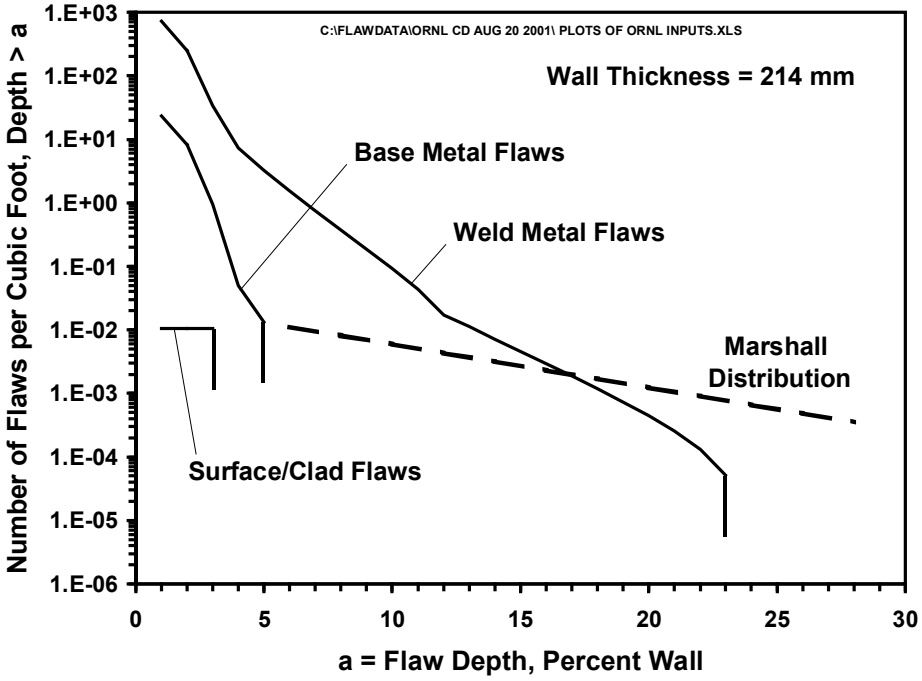

Figure B11. Example of new data on defects compared with the Marshall distribution [B36].

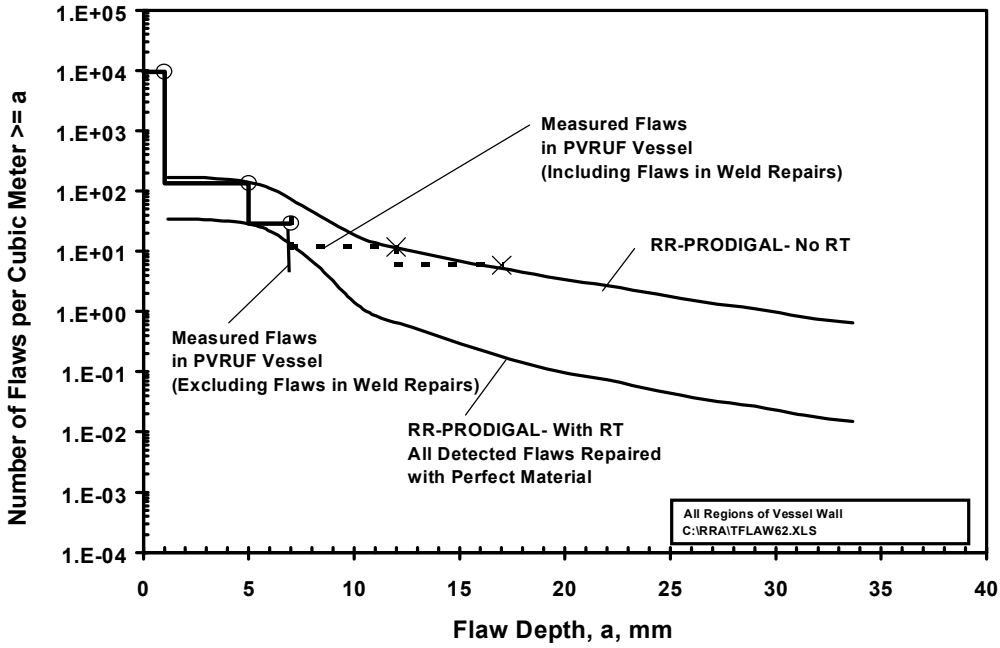

Figure B12. Comparison between measured defect data and resulting defect distribution using the expert system RR-PRODIGAL [B36-B37].

B9. ProSACC

The procedure described in this handbook including calculation of crack growth due to fatigue and stress corrosion has been implemented in a Windows based PC-program called ProSACC [B1]. ProSACC also has the option of running a probabilistic R6 analysis. Besides this, ProSACC contains options for assessment of cracks according to the 1995 edition of the ASME Boiler and Pressure Vessel Code, Section XI. Appendices A, C and H for assessment of cracks in ferritic pressure vessels, austenitic piping and ferritic piping, respectively.

ProSACC is written in Microsoft Visual Basic and Compaq Visual Fortran. ProSACC runs under most Microsoft Windows operating systems, *i.e.* Windows 98/Me/NT4/2000/XP. Get in contact with Det Norske Veritas for more information.

B10. References

[B1] DILLSTRÖM, P., and W. ZANG., (2004), "User manual ProSACC Version 1.0", DNV Research Report 2004/02, Det Norske Veritas AB, Stockholm, Sweden.

[B2] MILNE, I., AINSWORTH, R. A., DOWLING, A. R., and A. T. STEWART, (1988), "Assessment of the integrity of structures containing defects", *The International Journal of Pressure Vessels and Piping*, Vol. 32, pp. 3-104.

[B3] —, (2003), "Assessment of the Integrity of Structures Containing Defects", R6 – Revision 4, Up to amendment record No.2, British Energy Generation Ltd.

[B4] AINSWORTH, R. A., (1986), "The treatment of thermal and residual stresses in fracture assessments", *Engineering Fracture Mechanics*, Vol. 24, pp. 65-76.

[B5] BERGMAN, M., (1996), "Fracture mechanics analysis for secondary stresses - Part 1", SA/FoU-Report 94/03 (in Swedish), SAQ Kontroll AB, Stockholm, Sweden.

[B6] DELFIN, P., SATTARI-FAR, I., and B. BRICKSTAD, (1997), "Effect of thermal and weld-induced residual stresses on the *J*-integral and CTOD in elastic-plastic fracture analyses", SAQ/FoU-Report 97/02, SAQ Kontroll AB.

[B7] ANDERSSON, M., and P. DILLSTRÖM, (2004), "Background and implementation of a new deterministic safety evaluation system", DNV Research Report to be published, Det Norske Veritas AB, Stockholm, Sweden.

[B8] BUDDEN, P., (1989), "Fracture assessments of combined thermal and mechanical loads using uncracked body stress analysis", CEGB Report RD/B/6158/R89, Central Electricity Generating Board, Berkley, U.K.

[B9] SATTARI-FAR, I., (1986), "Constraint effects on behaviour of surface cracks in cladded reactor pressure vessels subjected to PTS transient", *The International Journal of Pressure Vessels and Piping*, Vol. 67, pp. 185-197.

[B10] HALLBÄCK, N., and F. NILSSON, (1992), "Fracture assessments for secondary loads", *Fatigue & Fracture of Engineering Materials and Structures*, Vol. 15, No. 2, pp. 173-186.

[B11] ANDERSON, T.L., (1995), *Fracture Mechanics – Fundamentals and Applications*, CRC Press, Second edition, Boca Raton, USA, 688p.

[B12] BRICKSTAD, B., and M. BERGMAN, (1996), "Development of safety factors to be used for evaluation of cracked nuclear components", SAQ/FoU-Report 96/07, SAQ Kontroll AB, Stockholm, Sweden.

[B13] DELFIN, P., and B. BRICKSTAD, (1998), "Residual stresses in multi-pass butt-welded bimetallic piping, Part I", SAQ/FoU-Report 98/12, SAQ Kontroll AB, Stockholm, Sweden.

[B14] DELFIN, P., and B. BRICKSTAD, (1999), "Residual stresses in multi-pass butt-welded bimetallic piping, Part II", SAQ/FoU-Report 99/06, SAQ Kontroll AB, Stockholm, Sweden.

[B15] CHAPULIOT, S., LACIRE,. M. H., and DELLIOU, P. Le., (1998), ”Stress intensity factors for internal circumferential cracks in tubes over a wide range of radius over thickness ratio”, *ASME PVP*, Vol. 365, pp 95-106.

[B16] DILLSTRÖM, P., and I. SATTARI-FAR., (2002), “Limit load solutions for surface cracks in plates and cylinders”, RSE R&D Report No. 2002/01, Det Norske Veritas AB.

[B17] ZANG, W., (1997), ”Stress intensity factor solutions for axial and circumferential trough-wall cracks in cylinders”, SINTAP/SAQ/02, SAQ Control AB, Stockholm, Sweden.

[B18] KLASÉN, B., DILLSTRÖM, P., and W. ZANG., (2003), “Stress Intensity Factor and Limit Load Solutions for Surface Cracks in Round Bars”, RSE R&D Report No. 2001/04, Rev. 1, Det Norske Veritas AB.

[B19] WILSON, R., (1995), “A User`s Guide to the Probabilistic Fracture Mechanics Computer Code: STAR6 - Version 2.2”, Memorandum TEM/MEM/0005/95, Nuclear Electric, Engineering Division, 75p.

[B20] BERGMAN, M., (1996), “User`s manual SACC version 4.0”, SAQ/FoU-Report 96/09, SAQ Kontroll AB, 9p.

[B21] DILLSTRÖM, P., (2000), ”Probabilistic Safety Evaluation - Development of Procedures with Applications on Components Used in Nuclear Power Plants”, SKi Report 00:58, Swedish Nuclear Power Inspectorate.

[B22] DILLSTRÖM, P., (2000), “ProSINTAP - A probabilistic program implementing the SINTAP assessment procedure”, *Engng Fract Mech*, V. 67, pp. 647-668.

[B23] CRUTZEN, S., FRANK, F., FABBRI, L., LEMAITRE, P., SCHNEIDER, Q., and W. VISSER, (1999), “Compilation of NDE effectiveness data”, SINTAP Task 3.4 Final Report, JRC - IAM, Petten, 77p.

[B24] GUNNARS, J., ANDERSSON, P., DILLSTRÖM, P. and G. SUND., (2002), “Risk based ranking of inspection sites for the reactor pressure vessels of Barsebäck 2, Oskarshamn 2 and Ringhals 1”, Technical Reports 10393500-3/4/7, Rev. 0/1, Det Norske Veritas AB.

[B25] BRICKSTAD, B., CHAPMAN, O.J.V., SCHIMPFKE, T., SCHULTZ, H., and A. MUHAMMED., (2003), “WP-4, Review and benchmarking of SRMs and associated softwares. Final Report”, Draft Report No. NURBIM D4, Det Norske Veritas AB and O.J.V. Consultancy.

[B26] FAIDY, C., (2003), “PROSIR - Probabilistic Structural Integrity of a PWR Reactor Pressure Vessel”, Round Robin Proposal, Rev. 4, EDF-SEPTEN.

[B27] BULLOUGH, R., GREEN, V. R., TOMKINS, B., WILSON, R., and J. B. WINTLE., (1999), ”A review of methods and applications of reliability analysis for structural integrity assessment of UK nuclear plant”, *International Journal of Pressure Vessel and Piping*, V 76, pp 909-919.

[B28] DILLSTRÖM, P., NILSSON, F., BRICKSTAD, B., and M. BERGMAN, (1993), ”Probabilistic Fracture Mechanics Analysis of a Nuclear Pressure Vessel for Allocation of In-Service Inspection”, *International Journal of Pressure Vessel & Piping*, V 54, pp 435-463.

[B29] WALLIN, K., (1984), “The scatter in K_{Ic}-results”, *Engineering Fracture Mechanics*, V 19, pp 1085-1093.

[B30] WALLIN, K., (1998), ”Probabilistisk säkerhetsvärdering PROPSE - Material-parametrar”, Rapport VALC444, VTT Tillverkningsteknik, 20p.

[B31] NILSSON, F., and B. ÖSTENSSON, (1978), ”J_{Ic}-testing of A-533 B – statistical evaluation of some different testing techniques”, *Engineering Fracture Mechanics*, V 10, pp 223-232.

[B32] WALLIN, K., (2001), “Low cost J-R-curve estimation based on CVN upper shelf energy”, *Fatigue and Fracture of Engineering Materials and Structures*, V. 24, pp 537-550.

[B33] BURDEKIN, F. M., and W. HAMOUR, (1998), ”SINTAP, Contribution to Task 3.5, Safety Factors and Risk”, UMIST, 25p.

[B34] SKÅNBERG, L., (1994), ”Kvalificering av OFP-system”, SKi Rapport 94:25, Statens kärnkraftinspektion, 45p.

[B35] BRICKSTAD, B., (2000), “The Use of Risk Based Methods for Establishing ISI-Priorities for Piping Components at Oskarshamn 1 Nuclear Power Station”, SAQ/FoU-Report 99/05, SAQ Kontroll AB / Det Norske Veritas.

[B36] JACKSON, D. A., ABRAMSON, L., DOCTOR, S. R., SIMONEN, F., and G. SCHUSTER, (2001), ”Development of Generalized Flaw Distribution as Input to the Re-Evaluation of the Technical Basis for US Pressurized Thermal Shock Regulation for PWRs”, *Presented at the NDE/Structural Integrity Conference – Seville, Spain – November 14-16, 2001*, United States Nuclear Regulatory Commission.

[B37] CHAPMAN, O.J.V., and F. A. SIMONEN, (1998), “RR-PRODIGAL – Model for Estimating the Probabilities of Defects in Reactor Pressure Vessel Welds”, NUREG/CR-5505, United States Nuclear Regulatory Commission.

APPENDIX X. EXAMPLE PROBLEM

A defect has been discovered in a plate, see Fig X1. The plate is assumed to be a component in a nuclear power plant and made of ferritic steel.

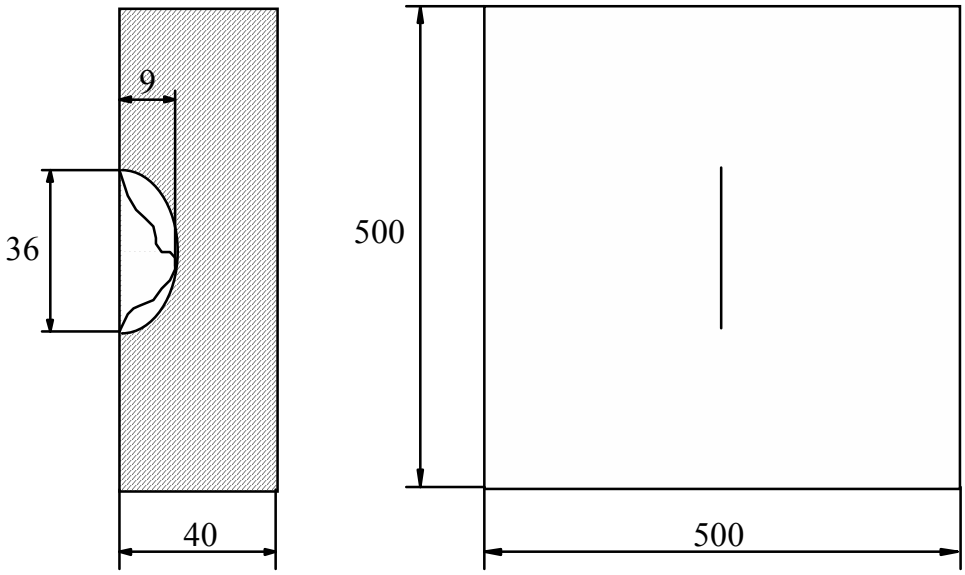

Figure X1. Plate with a defect (unit mm).

The material has the following measured properties at 20 and 150 °C.

$$K_{Ic}(150\ °C) = 160\ \text{MPa}\sqrt{\text{m}},$$

$R_{p0.2}(20\ °C) = 300$ MPa, $R_{p0.2}(150\ °C) = 280$ MPa,

$R_m(20\ °C) = 490$ MPa, $R_m(150\ °C) = 490$ MPa.

The plate is loaded by a tensile load due to dead weight and a thermal gradient. A stress analysis reveals that the nominal stress is 100 MPa due to dead weight and that the thermal gradient affects the plate with a bending stress of 180 MPa. The bending stress is tensile on the cracked side of the plate. The stresses act perpendicularly to the crack plane.

Perform a defect assessment to decide whether the crack can be accepted or not if the load event is categorised as normal. For reasons of simplicity, the temperature can be considered as constant and equal to 150 °C in the assessment.

X1. Solution

The defect assessment is performed according to the procedure described in Chapter 2 of this handbook.

X1.1 Characterization of defect

According to Appendix A, the defect is characterized as a semi-elliptical surface crack with depth a = 9 mm and length l = 36 mm.

X1.2 Choice of geometry

A plate with a finite surface crack is selected, see Fig. G1.1. The thickness of the plate is 40 mm.

X1.3 Determination of the stress state

The primary stress state consists of a membrane stress σ_m^p = 100 MPa due to dead weight, and the secondary stress state of a bending stress σ_b^s = 180 MPa due to the thermal gradient.

X1.4 Determination of material data

According to Chapter 2.5 the yield strength σ_Y, the ultimate tensile strength σ_U and the critical stress intensity factor K_{cr} must be determined. This is done by setting $\sigma_Y = R_{p0.2}$, $\sigma_U = R_m$ and $K_{cr} = K_{\mathrm{Ic}}$. Thus

$$K_{cr}(150\ ^\circ\mathrm{C}) = 160\ \mathrm{MPa}\sqrt{\mathrm{m}},$$

$$\sigma_Y(20\ ^\circ\mathrm{C}) = 300\ \mathrm{MPa}, \qquad \sigma_Y(150\ ^\circ\mathrm{C}) = 280\ \mathrm{MPa},$$

$$\sigma_U(20\ ^\circ\mathrm{C}) = 490\ \mathrm{MPa}, \qquad \sigma_U(150\ ^\circ\mathrm{C}) = 490\ \mathrm{MPa}.$$

X1.5 Calculation of possible slow crack growth

No crack growth mechanisms need to be considered in this case.

X1.6 Calculation of K_{I}^p and K_{I}^s

The stress intensity factors K_{I}^p and K_{I}^s are calculated according to Appendix K, Eqs. (K1) and (K2). The primary and secondary stress are expressed according to Eq. (K2).

$$\sigma^p = 100 = \sigma_0^p \quad ,$$

$$\sigma^s = 180\left(1-\frac{2u}{t}\right) = 180 - 360\frac{u}{t} = 180 - 360\frac{u}{a}\frac{a}{t} = 180 - 81\frac{u}{a} = \sigma_0^s + \sigma_1^s\frac{u}{a} \quad .$$

Hence σ_0^p = 100 MPa, σ_0^s = 180 MPa and σ_1^s = -81 MPa. All other stress components are zero. With $a/t = 9/40 = 0.225$ and $l/a = 36/9 = 4$, linear interpolation in Tables K1 and K2 gives the required geometry functions.

$$f_0^{\mathrm{A}} = 0.896\,, \qquad f_1^{\mathrm{A}} = 0.573\,,$$

$$f_0^{\mathrm{B}} = 0.738\,, \qquad f_1^{\mathrm{B}} = 0.123\,.$$

K_{I}^p and K_{I}^s at the deepest point of the crack (point A) become

$$\left(K_{\mathrm{I}}^p\right)^{\mathrm{A}} = \sqrt{\pi a}\,(\sigma_0^p f_0^{\mathrm{A}}) = $$
$$= \sqrt{\pi\cdot 0.009}\,\left(100\cdot 0.896\right) = 15.07\ \mathrm{MPa}\sqrt{\mathrm{m}} \quad ,$$

$$\left(K_{\mathrm{I}}^s\right)^{\mathrm{A}} = \sqrt{\pi a}\,(\sigma_0^s f_0^{\mathrm{A}} + \sigma_1^s f_1^{\mathrm{A}}) = $$
$$= \sqrt{\pi\cdot 0.009}\,(180\cdot 0.896 - 81\cdot 0.573) = 19.31\ \mathrm{MPa}\sqrt{\mathrm{m}} \quad .$$

K_{I}^{p} and K_{I}^{s} at the intersection of the crack with the free surface (point B) become

$$\left(K_{\mathrm{I}}^{p}\right)^{\mathrm{B}} = \sqrt{\pi a}(\sigma_0^{p} f_0^{\mathrm{B}}) = \\ = \sqrt{\pi \cdot 0.009}\left(100 \cdot 0.738\right) = 12.41\ \mathrm{MPa}\sqrt{\mathrm{m}} \quad ,$$

$$\left(K_{\mathrm{I}}^{s}\right)^{\mathrm{B}} = \sqrt{\pi a}(\sigma_0^{s} f_0^{\mathrm{B}} + \sigma_1^{s} f_1^{\mathrm{B}}) = \\ = \sqrt{\pi \cdot 0.009}(180 \cdot 0.738 - 81 \cdot 0.123) = 20.66\ \mathrm{MPa}\sqrt{\mathrm{m}} \quad .$$

X1.7 Calculation of L_r

L_r is calculated according to Appendix L, Eqs. (L1) - (L3). Eq. (L2) gives

$$\zeta = \frac{al}{t(l+2t)} = \frac{9 \cdot 36}{40 \cdot (36 + 2 \cdot 40)} = 0.0698 \quad .$$

Since the primary stress state in this case only consists of a membrane stress, L_r becomes

$$L_r = \frac{\sqrt{(1-\zeta)^{3.14}\left(\sigma_m^{p}\right)^2}}{(1-\zeta)^2 \sigma_Y} = \frac{\sqrt{(1-0.0698)^{3.14} \cdot 100^2}}{(1-0.0698)^2 \cdot 280} = 0.368 \quad .$$

X1.8 Calculation of K_r

K_r is calculated according to Chapter 2.9. In the deepest point of the crack (point A) we obtain

$$\chi^{\mathrm{A}} = \frac{\left(K_{\mathrm{I}}^{s}\right)^{\mathrm{A}} L_r}{\left(K_{\mathrm{I}}^{p}\right)^{\mathrm{A}}} = \frac{19.31 \cdot 0.368}{15.07} = 0.472 \quad ,$$

which according to Fig. 2.2 gives $\rho = 0.034$. Hence,

$$K_r^{\mathrm{A}} = \frac{\left(K_{\mathrm{I}}^{p}\right)^{\mathrm{A}} + \left(K_{\mathrm{I}}^{s}\right)^{\mathrm{A}}}{K_{cr}} + \rho^{\mathrm{A}} = \frac{15.07 + 19.31}{160} + 0.034 = 0.249 \quad .$$

Similarly we obtain at the intersection of the crack with the free surface (point B),

$$\chi^{\mathrm{B}} = \frac{\left(K_{\mathrm{I}}^{s}\right)^{\mathrm{B}} L_r}{\left(K_{\mathrm{I}}^{p}\right)^{\mathrm{B}}} = \frac{20.66 \cdot 0.368}{12.41} = 0.613 \quad ,$$

$$\rho = 0.039 \quad ,$$

$$K_r^{\mathrm{B}} = \frac{\left(K_{\mathrm{I}}^{p}\right)^{\mathrm{B}} + \left(K_{\mathrm{I}}^{s}\right)^{\mathrm{B}}}{K_{cr}} + \rho^{\mathrm{B}} = \frac{12.41 + 20.66}{160} + 0.039 = 0.246 \quad .$$

The maximum value of K_r is used in the assessment and is obtained at the deepest point of the crack (point A).

X1.9 Fracture assessment

The fracture assessment is described in Chapter 2.10. The non-critical region in the failure assessment diagram is defined by

$$K_r \le f_{R6} = (1 - 0.14L_r^2)[0.3 + 0.7\exp(-0.65L_r^6)] \quad ,$$

$$L_r \le L_r^{\max} \quad .$$

Since the component is nuclear and made of a ferritic material without a yield plateau ($R_{p0.2}$ has been measured instead of R_{eL}), $L_r^{\max}$ is given by

$$L_r^{\max} = \frac{\sigma_f}{\sigma_Y} = \frac{2.4S_m}{\sigma_Y} = \frac{2.4 \cdot 163}{280} = 1.4 \quad ,$$

where the allowable design stress S_m has been calculated according to Eq. (2.15). The point $\left(L_r, K_r\right) = \left(0.368, 0.249\right)$ is plotted in the failure assessment diagram. See Fig. X2.

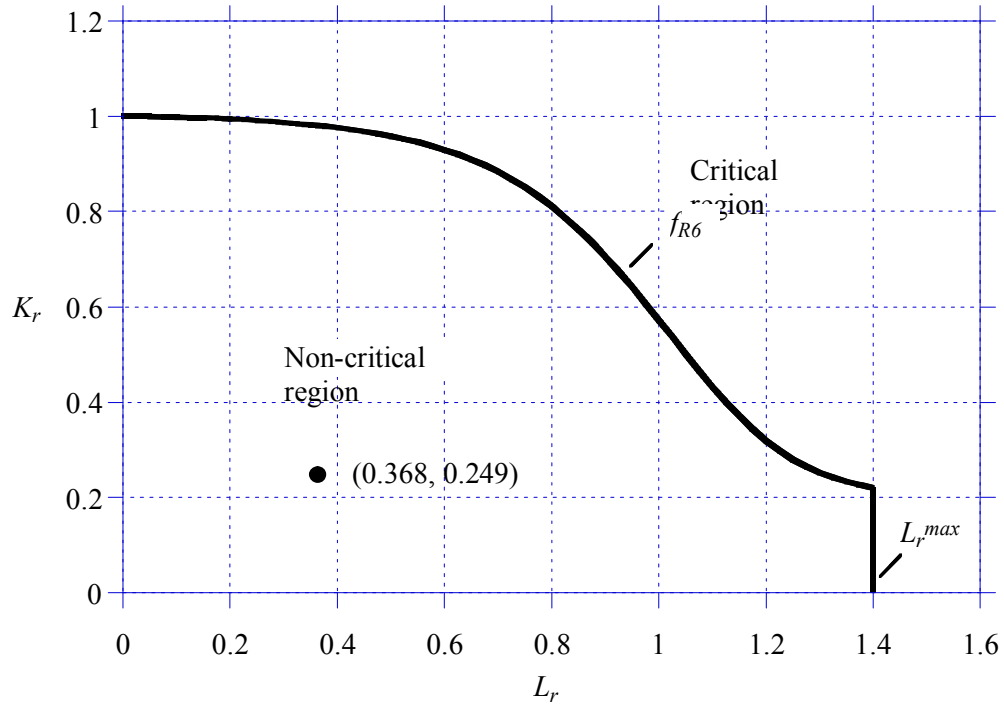

Figure X2. Fracture assessment.

The point is situated within the non-critical region in the failure assessment diagram. Thus fracture is not to be expected. However, the defect may still not be acceptable with respect to required safety demands to continue operation without repair or replacement of the component. This is investigated in the safety assessment.

X1.10 Safety assessment

The safety assessment is described in Chapter 2.11. The acceptable region in the failure assessment diagram is defined by

$$K_r^{acc} = \frac{K_I^p + K_I^s}{K_{cr}} + \frac{\rho}{\sqrt{SF_J}} \le \frac{f_{R6}(L_r)}{\sqrt{SF_J}} \quad ,$$

$$L_r \le \frac{L_r^{\max}}{SF_L} \quad .$$

Recommended values for the safety factors SF_J and SF_L are found in Appendix S. For a ferritic steel component under a normal load event, SF_J = 10 and SF_L = 2.4. Hence the maximum value of K_r^{acc} (i.e. at the deepest point of the crack) becomes

$$K_r^{acc} = \frac{15.07 + 19.31}{160} + \frac{0.034}{\sqrt{10}} = 0.226 \quad .$$

The point $\left(L_r, K_r^{acc}\right) = \left(0.368, 0.226\right)$ is plotted in the failure assessment diagram where also the acceptable region has been drawn. See Fig. X3.

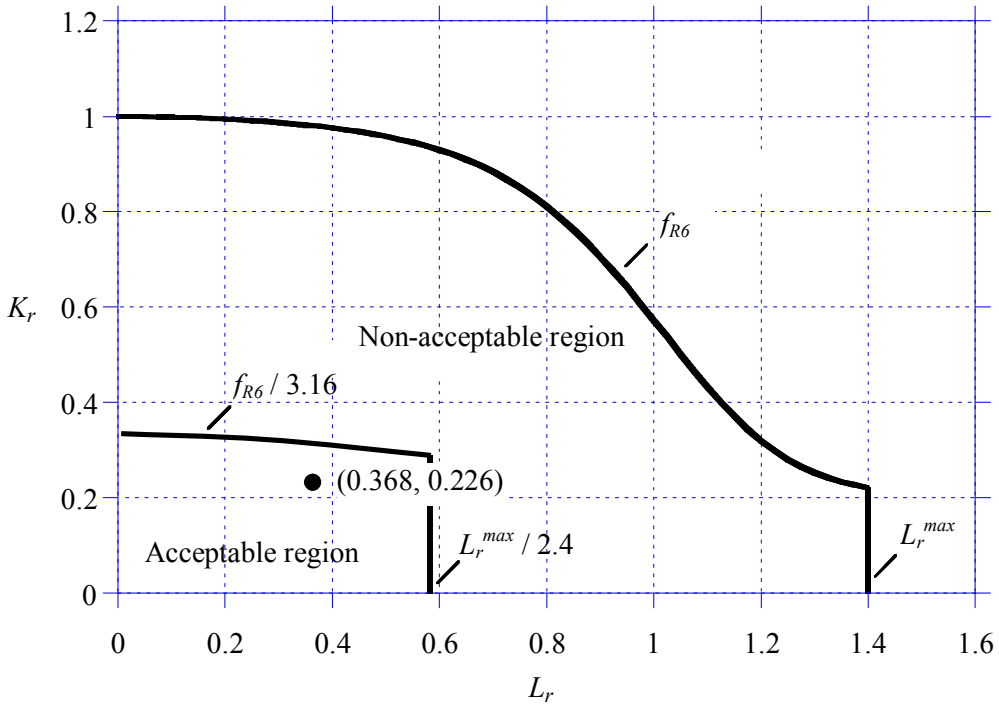

Figure X3. Safety assessment.

The point is situated within the acceptable region of the failure assessment diagram. Hence the defect is acceptable with respect to required safety demands and operation may continue without repair or replacement of the component.

By repeating the above calculations for gradually increasing crack sizes until the assessment point falls on the line that limits the acceptable region it can be shown that the maximum acceptable crack depth is 17.0 mm if the crack aspect ratio l/a remains constant and equal to 4.

Strålsäkerhetsmyndigheten
Swedish Radiation Safety Authority

SE-171 16 Stockholm
Solna strandväg 96

Tel: +46 8 799 40 00
Fax: +46 8 799 40 10

E-mail: registrator@ssm.se
Web: stralsakerhetsmyndigheten.se